



저작자표시-비영리-변경금지 2.0 대한민국

이용자는 아래의 조건을 따르는 경우에 한하여 자유롭게

- 이 저작물을 복제, 배포, 전송, 전시, 공연 및 방송할 수 있습니다.

다음과 같은 조건을 따라야 합니다:



저작자표시. 귀하는 원저작자를 표시하여야 합니다.



비영리. 귀하는 이 저작물을 영리 목적으로 이용할 수 없습니다.



변경금지. 귀하는 이 저작물을 개작, 변형 또는 가공할 수 없습니다.

- 귀하는, 이 저작물의 재이용이나 배포의 경우, 이 저작물에 적용된 이용허락조건을 명확하게 나타내어야 합니다.
- 저작권자로부터 별도의 허가를 받으면 이러한 조건들은 적용되지 않습니다.

저작권법에 따른 이용자의 권리는 위의 내용에 의하여 영향을 받지 않습니다.

이것은 [이용허락규약\(Legal Code\)](#)을 이해하기 쉽게 요약한 것입니다.

[Disclaimer](#)

**Scanning Tunneling Microscope Investigation on the Atomistic
and Electronic Structures of Two-Dimensional Materials**

by
Trinh Thi Ly

Dissertation
Submitted to
the Graduate School of the University of Ulsan
in partial Fulfillment of the Requirements
for the Degree of
Doctor of Philosophy

Department of Physics
Ulsan, Korea
August 2021

**Scanning Tunneling Microscope Investigation on the Atomistic
and Electronic Structures of Two-Dimensional Materials**

Supervisor: Professor Jungdae Kim

Dissertation
Submitted to
the Graduate School of the University of Ulsan
in partial Fulfillment of the Requirements
for the Degree of
Doctor of Philosophy
by
Trinh Thi Ly

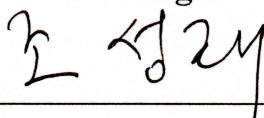
Department of Physics
Ulsan, Korea
August 2021

Scanning Tunneling Microscope Investigation on the Atomistic and Electronic Structures of Two-Dimensional Materials

This certifies that the dissertation of TRINH THI LY is approved by:

Committee Chair: **Professor Sunglae Cho**

Signature:



Committee Member: **Professor Jungdae Kim**

Signature:



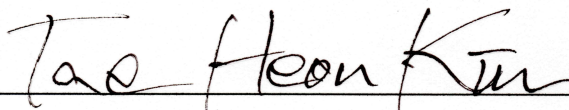
Committee Member: **Professor Jaekwang Lee**

Signature:



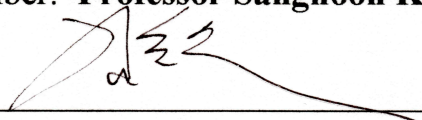
Committee Member: **Professor Tae Heon Kim**

Signature:



Committee Member: **Professor Sanghoon Kim**

Signature:



Department of Physics

University of Ulsan

August 2021

*I would like to dedicate this dissertation to my beloved parents, my
brother, sister-in-law, and my boyfriend:*

Trịnh Văn Bình

Lê Thị Đạt

Trịnh Văn Lương

Bùi Thị Phương

Phạm Minh Đức

Acknowledgements

First of all, I would like to respectfully thank to my supervisor, Professor Jungdae Kim for his valuable guidance, encouragement and support during my Ph.D. study at the University of Ulsan. It has been my great happiness to complete my Ph.D study under his guidance.

I would like to express my sincere thanks to my thesis committee members: Professor Jaekwang Lee (Pusan National University), Professor Sunglae Cho (University of Ulsan), Professor Tae Heon Kim (University of Ulsan), Professor Sanghoon Kim (University of Ulsan) for their valuable time, insightful comments and suggestions on my Ph.D thesis.

I would like to thank all Professors in University of Ulsan for their lectures and supports during my courses; all my collaborators because of their hard working and supporting.

I would like to share my heartfelt appreciation to my labmates in the Nanoscale Surface Science Laboratory (NSSL) who are Mr. Sangui Kim, Doctor Ganbat Duvjir, Mr. Taehoon Kim, Mr. Sanghwa Kim, Mr. Nguyen Huu Lam for the useful discussions, encouragement, help, and memorable moments during my study.

I also need to thank my advisors in undergraduate time, Doctor. Pham Van Vinh because he recommended me to be here for studying.

Finally, I would like to express my family gratitude to my parents, brother and sister-in-law, boyfriend, and all my relatives for their inspiration, care, and affection.

Ulsan, August 2021

Trinh Thi Ly

Abstract

Scanning Tunneling Microscope Investigation on the Atomistic and Electronic Structures of Two-Dimensional Materials

Trinh Thi Ly, Ph.D.

The University of Ulsan at Ulsan, 2021

Supervisor: Professor Jungdae Kim

Two dimensional (2D) materials have been taking much attention from researchers due to their promising characteristic for making devices. The 2D van der Waals (vdW) layered materials can be fabricated by a simple mechanical exfoliation from the bulk because of weak vdW coupling. In the 2D limit where electrons can only move freely in the plane perpendicular to the direction of confinement, the contribution on physical properties of the material surface becomes dominant, leading to demand for understanding the surface structure. For this reason, we use scanning tunneling microscopy (STM) to directly observe the surface structure at the atomic level of some materials such as layered vdW crystals (SnSe, $\text{SnSe}_{1-x}\text{S}_x$, $\text{Fe}_{5-x}\text{GeTe}_2$), monolayer transition-metal dichalcogenides (TMDs) (VSe_2 and ReSe_2) on bilayer graphene (BLG), and ultrathin Cu_2O films.

In this thesis, a brief introduction to 2D materials and scanning tunneling microscope are shown in chapter 1 and 2, respectively. In chapter 3, we figure out the origin of p-type electrical characteristic in SnSe and the alloying behavior of $\text{SnSe}_{1-x}\text{S}_x$ which are helpful for the optimization of thermoelectric properties of SnSe-based materials. Moreover,

we find that the non-centrosymmetry originated from $\sqrt{3}\times\sqrt{3}$ orderings of the Fe(1) - Ge pair resulting in helical magnetism in $\text{Fe}_{5-x}\text{GeTe}_2$, which is included in chapter 4. Following that, STM results regarding the charge density wave in monolayer VSe_2 on BLG and the trapped charge structure at ReSe_2 -graphene interface are discussed in chapter 5. Finally, chapter 6 is intended for the surface structure and the origin of hole source in ultrathin Cu_2O films.

Contents

Abstract	i
Contents	iii
List of Figures	v
List of Table	xii
Chapter 1	1
Overview of two-dimensional materials	1
Chapter 2	4
Scanning tunneling microscope	4
2.1 A back ground theory of scanning tunneling microscopy	4
2.1.1 Tunneling junction in STM	4
2.1.2 The Bardeen's approach to tunneling current	8
2.1.3 Tunneling matrix	10
2.2 Scanning tunneling microscope	16
2.2.1 STM mechanism and two scanning mode	16
2.2.2 Scanning tunneling spectroscopy	18
2.2.3 Measure dI/dV using lock-in amplifier	20
2.2.4 Overview of home built low temperature STM	23
2.2.5 STM head pan type	24
Chapter 3	25
Layered chalcogenide materials: SnSe, SnSe_{1-x}S_x	25
3.1 Structure of SnSe(S)	26
3.2 Surface treatment	28
3.3 Origin of p-type characteristic in SnSe	28
3.4 Alloying behaviors of SnSe _{1-x} S _x	32
3.5 Summary	40
Chapter 4	41
Magnetic vdW Materials: Fe_{5-x}GeTe₂	41
4.1 Surface treatment	44
4.2 Analysis surface structure of Fe _{5-x} GeTe ₂	45
4.2.1 Overview of Fe _{5-x} GeTe ₂ surface morphology	47
4.2.2 Origin of $\sqrt{3}\times\sqrt{3}$ superstructure in Fe _{5-x} GeTe ₂ surface	48
4.2.3 B area-Fe deficiency area	51

4.3	Magnetic properties of $\text{Fe}_{5-x}\text{GeTe}_2$	53
4.4	Conclusion.....	59
Chapter 5.....		60
Monolayer transition-metal dichalcogenides: VSe_2, ReSe_2		60
5.1	Monolayer VSe_2 on BLG: Lattice Distortion driving Charge Density Wave of $\sqrt{3} \times 2$ and $\sqrt{3} \times \sqrt{7}$	61
5.1.1	Sample preparation	63
5.1.2	Results and Discussion	64
5.1.3	Conclusion	70
5.2	Monolayer ReSe_2 on BLG.....	71
5.2.1	Atomistic and electronic structures of ML ReSe_2 on BLG	73
5.2.2	Trapped charge in vdW heterojunction of ML ReSe_2 on BLG.....	76
5.2.3	Conclusion	82
Chapter 6.....		83
Ultrathin Cu_2O Films		83
6.1	Introduction	83
6.2	Sample preparation.....	86
6.3	Surface structure.....	87
6.4	Intrinsic defect – An origin of p-type characteristic.....	91
6.5	Conclusion.....	97
Appendix A – Tip state effect to STM topography images of SnSe.....		98
Appendix B – Magnetic properties of $\text{Fe}_{5-x}\text{GeTe}_2$.....		101
Appendix C – Tip and sample preparation.....		108
Bibliography.....		110
Publications		128

List of Figures

Figure 1.1: Overview of two-dimensional materials world and the fabrication methods.	2
Figure 2.1: Metal-vacuum-metal problem in classical mechanics and quantum mechanics point of views.	4
Figure 2.2: A simple tunneling junction model (one-dimensional case) for STM with a negative bias (V) applied to the sample.	7
Figure 2.3: Bardeen’s approach to tunneling current. Tunneling current is originated by overlapping of two electron wave functions for sample (χ) and tip (ψ)......	9
Figure 2.4: An example of tip states effect to atomic corrugation in STM image. Simple picture of the corrugation increased by a ‘sharper’ dz ² -wave tip orbital as compared to s orbital.....	15
Figure 2.5: A schematic diagram of the scanning tunneling microscope.	16
Figure 2.6: Two operation modes for STM. (a) current constant and (b) height constant.	18
Figure 2.7: The STM tunneling process with positive bias voltage applied to sample.	19
Figure 2.8: dI/dV measurement using lock-in amplifier in STM. (a) A schematic of experimental set up. (b) I/V curve is obtained together with (c) dI/dV curve from output of lock-in amplifier.	20
Figure 2.9: A low temperature home built STM system. (a) A picture of low temperature home built STM system. (b) A schematic of the STM chamber.	23
Figure 2.10: Pan type STM head. (a-b) Schematic of Pan type STM head: 1. Macor body, 2. STM tip, 3. Shear piezo stacks glued on the macor body, 4. Piezo tube scanner, 5. Sapphire prism which holds the scanner and tip, 6. Stainless steel spring plate, 7. Sapphire (or ruby) ball, 8. Macor plate, 9. Sample, 10. Sample stage. (c) The pictures of a Pan type STM head with the main parts.	24

- Figure 3.1: Structure information of SnSe(S).** (a) A perspective view of one SnSe(S) layer. (b) Top view of SnSe(S), the red and blue balls represent Sn and Se(S) atoms, respectively. (c) The side view presents the buckling structure of the SnSe(S) layer structure. 27
- Figure 3.2: The cleaving in-situ process using Kapton tape for SnSe and SnSe_{1-x}S_x single crystals.** 28
- Figure 3.3: Surface structure of cleaving plane of SnSe.** (a) The clean cleavage surface is obtained in STM image (3 V, 30 pA). (b) The atomic structure of SnSe along *bc*-plane (2 V, 50 pA). 29
- Figure 3.4: Defect nature of SnSe.** (a) STM image of SnSe surface showing three kind of defect A, B, and A'. (b) STM and DFT simulation images prove that defect A is single Sn vacancy defect. Scanning condition for (a) and upper panel in (b) are (-2 V, 50 pA) and (-1.5 V and 30 pA), respectively. 30
- Figure 3.5: Single Sn vacancy is origin of p-type characteristic in SnSe.** *dI/dV* tunneling spectroscopy (the green and pink curves) measured at (the green and the pink) position surrounding V_{Sn} site. The STS of V_{Sn} is directly compared with that of defect-free areas (black curve). The inset shows an STM image of Sn vacancy with the marked position. 31
- Figure 3.6: All samples of SnSe_{1-x}S_x (x = 0.2, 0.4, 0.6) are single crystals.** (a) Atomic relaxation model of SnSe and SnS (red and blue balls correspond to Sn and Se (or S) atoms, respectively). (b) XRD data of SnSe_{1-x}S_x single crystals (x = 0.2, 0.4, 0.5) on the cleavage plane. (c) High resolution plot of the strongest diffraction peak (400). The inset shows the change in lattice constants of SnSe_{1-x}S_x along the a-axis. 33
- Figure 3.7: DFT simulation image confirms the substituted S atoms locating at the dark positions.** (a) STM topographic images of SnSe and (b) SnSe_{0.8}S_{0.2} single crystals. The inset in (a) shows the atomic model of a SnSe cleavage surface where red and blue balls correspond to Sn and Se atoms, respectively. Tunneling conditions: (a) V_s = - 2 V, I_t = 50 pA and (b) V_s = - 1.7 V, I_t = 80 pA. (c) Relaxed structural model of a SnSe surface with three substituted S atoms. Red, blue, and yellow spheres represent Sn, Se, and S atoms, respectively. (d) Simulated STM image for the SnSe supercell with three substituted S atoms. 35

Figure 3.8: STM topography images of SnSe_{1-x}S_x (x = 0.2, 0.4, 0.5). STM topographic images of (a) SnSe_{0.8}S_{0.2}, (b) SnSe_{0.6}S_{0.4}, and (c) SnSe_{0.5}S_{0.5}. All STM images are 20 × 20 nm in size with (a) V_s = - 0.9 V, I_t = 60 pA, (b) V_s = - 1.5 V, I_t = 40 pA, and (c) V_s = - 2.3 V, I_t = 20 pA. The dark areas in (a-c) were mapped with a red color in (d-f) by subtracting ideal lattices with uniform intensity. (g-i) are pie charts showing fractional percentage of areal sizes counted from the red areas in (d-f). 37

Figure 3.9: Alloy degree and mixing energy of SnSe_{1-x}S_x alloys. (a) Quantitative analysis of S atom distributions in SnSe_{1-x}S_x alloys. The alloying degree J for S atoms was estimated to be about 60%, which indicates that homo-atoms prefer to bond with one another rather than with hetero-atoms. (b) Mixing energies of SnSe_{1-x}S_x alloys as a function of S content. The positive mixing energies indicates that SnSe_{1-x}S_x has a tendency towards phase segregation into SnSe and SnS. 39

Figure 4.1: Fe_{5-x}GeTe₂ surface is cleaved by conducting epoxy to remove contaminations. 44

Figure 4.2: Structure model of Fe₅GeTe₂. a) Crystal structure of Fe₅GeTe₂ (space group R3m). Two possible Fe(1) – Ge split-sites of b) Fe(1)_{up} – Ge_{down} and c) Ge_{up} – Fe(1)_{down}. Vectors a, b, and c are along [100], [010], and [001] directions. The black, pink, blue, and red balls represent Te, Fe(1), Ge, and Fe(2)-(3) atoms, respectively; open circles indicate possible occupancy sites of Fe(1) and Ge. 45

Figure 4.3: Surface morphology of Fe₅GeTe₂. a) STM topographic image obtained from the cleavage surface of Fe_{5-x}GeTe₂ shows two different regions, marked by I and II (V_b = 100 mV, I_t = 50 pA at 79 K). b) Line profile taken along the arrow in (a). c) Zoomed-in STM image taken from the black box in (a). d) Zoomed-in STM image taken from the black box in (c). The dashed lines indicate the crystal axes. e) The fast Fourier transformation (FFT) image of (d). All STM images were taken at the same conditions of V_b = 10 mV, I_t = 50 pA. 47

Figure 4.4: Detailed atomic structures of Fe_{5-x}GeTe₂ surfaces. a-b) STM images are taken from region I and II in Fig. 4.3a, respectively. STM image obtained from region II in (b) shows two different areas, marked by A and B. c) The higher resolution STM image showing both A and B areas. (d) The fast Fourier transformation (FFT) images of (a-c) showing both

hexagonal lattice and $\sqrt{3}\times\sqrt{3}$ superstructures marked as white and yellow circles, respectively..... 48

Figure 4.5: Comparison between STM and DFT simulation images of $\sqrt{3}\times\sqrt{3}$ superstructures. a) and b) STM images of $\sqrt{3}\times\sqrt{3}$ superstructures with “udd” and “duu” orderings of Fe(1) layers, respectively. The Y-shaped feature connects three Te atoms to one Fe(1)_{up} atom at the center. c) and d) DFT simulation STM images of “udd” and “duu” orderings. e) and f) show the line profiles crossing Te (black) and Fe(1) (pink) lattices taken along the solid lines in (a) and (b), respectively. The suggested models are provided below the line profiles and the Fe(2)-(3) atoms are not illustrated for simplicity. The scanning conditions of (a-b) are $V_b = 10$ mV, $I_t = 50$ pA. 49

Figure 4.6: Lattice distortion of the top Te layer. a-b) Line profiles crossing Te atoms along the black arrows in (c) and (d). d_1 and d_2 indicate Te-Te atomic spacing with Fe(1)_{up} and Fe(1)_{down}, respectively. c-d) STM topography images showing “udd” and “duu” ordering of Fe(1). e) Table of d_1 and d_2 values.). All STM images were taken at the same conditions of $V_b = 10$ mV, $I_t = 50$ pA. 51

Figure 4.7: Comparison between STM and DFT simulation images. a) STM topography image of Fe-deficient area in Fe₅GeTe₂ ($V_b = 10$ mV and $I_t = 50$ pA). b) DFT simulation image of Fe₄GeTe₂. (c) FFT image of (a)..... 52

Figure 4.8. The magnetic properties of Fe_{5-x}GeTe₂. a) Fe_{5-x}GeTe₂ crystal (upper) and 2D helical ordering (lower) based on chiral soliton lattice phase of Fe_{5-x}GeTe₂ with crystallographic direction marked. The arrows represent the total magnetization (including both Fe and Ge magnetic moments), which exhibits a helical ordering along the *b*-axis. The three layers of the arrows show the magnetization profile along the *a*-axis. b) Temperature dependence of magnetization measured for in-plane (red, $H//ab$ -plane) and out of plane (black, $H//c$ -axis) field with 5 mT. The commensurate (blue-shaded area)-to-incommensurate (yellow-shaded area) transition appears around 273 K. The inset shows the magnetic anomaly of $H//ab$ -plane (upper) and $H//c$ -axis (bottom). c) and d) Comparison of temperature-dependent magnetization in various applied magnetic fields for (c) $H//ab$ -plane and (d) $H//c$ -axis, respectively. The forced ferromagnetic state was observed in both cases of $H//ab$ -plane and $H//c$ -axis under 1 T (saturation field). e) Temperature dependence of magnetization with the forced ferromagnetic state fitted by Bloch 3/2 law. The red solid line

is the fitted curve. The MFM images of $\text{Fe}_{5-x}\text{GeTe}_2$ in f) 140 K and g) 77 K. The stripe domain wall was observed. The red and blue indicate spin-up and down states of domain, respectively. The inset of (g) is the line profile taken along the white dotted line, which exhibits the fan-like fine structures in the magnetic domains (also schematically illustrated in the inset). 54

Figure 5.1: Sample cleaning process for VSe_2 on BLG..... 63

Figure 5.2: STM images of ML VSe_2 on BLG. (a) STM image of the morphology of ML VSe_2 grown on bilayer graphene (BLG) ($V_b = 3$ V, $I_t = 30$ pA). (b) Line profile taken along the arrow in (a). (c) High resolution STM image showing strong stripe modulation ($\sqrt{3} \times 2$ and $\sqrt{3} \times \sqrt{7}$ CDW) marked by dashed lines ($V_b = -1.6$ V, $I_t = 50$ pA). (d) Fourier-filtered image generated by selectively taking the stripe modulation peaks (red circles) and VSe_2 lattice peaks (white circles) in (e). (e) Fast Fourier transformation (FFT) image of (c). 64

Figure 5.3: STM topography and dI/dV mapping images of ML VSe_2 on BLG. (a) STM topography image and (b) corresponding FFT image of ML VSe_2 . (c) Simultaneously taken dI/dV mapping image and (d) corresponding FFT image. The white and red circles in (b) and (d) indicate the Bravais lattice of VSe_2 and CDW peaks, respectively. Scanning condition: $V_b = -1.5$ V, $I_t = 50$ pA. Scan size: 5 nm \times 5 nm. 67

Figure 5.4: Lattice distortion of the top Se atoms. (a) STM topography of ML VSe_2 shows the CDW phase with $\sqrt{3} \times 2$ (pink rectangles) and $\sqrt{3} \times \sqrt{7}$ (black parallelograms) periodicities ($V_b = -1.5$ V, $I_t = 30$ pA). (b) The line profile is taken along the blue line in (a) and shows the strong lattice distortion of the top Se atoms. (c) Schematic model of Se lattice distortions. 69

Figure 5.5: Introduce of ReSe_2 on BLG. (a) Model structure of ML ReSe_2 on graphene. Dark (light) green, white, and brown balls represent upper(bottom) Se, Re, and C atoms. Vector a , b , and c are three crystal axes. Vector a is along Re-chain direction. (b) The morphology of ReSe_2 on graphene ($V_b = 1.5$ V, $I_t = 30$ pA). (c) The STM image of ML ReSe_2 (left side) taken at bias voltage of 1 V is compared to the DFT simulated STM image (right side). The bright spots in STM images at 1 V are mostly attributed by upper Se and Re atoms. (d) The STS measurement displayed in logarithm scale ($\log(dI/dV)$) taken at ML ReSe_2 shows the valence band maximum (VBM) and conduction band minimum (CBM) at -1.2 eV and 0.5 eV, respectively. 74

Figure 5.6: STM image taken at bias voltage within ReSe₂ energy gap. Within one scan image, the bias voltage is switched from 0.1 V to 1.0 V at the certain position (black arrow) and changed back to 0.1 V (at the white arrow position). The scanning condition at $I_t = 50$ pA. 76

Figure 5.7: Origin of the “in-gap” pattern. (a) STM image taken from ML ReSe₂ area at 0.1 V ($I_t = 50$ pA) is compared to (b) DFT simulated STM image at 0.5 V. (c) The trapped charge distribution between vdW gap graphene and ReSe₂ monolayer along top view (upper) and side view (bottom). (d) Plane-averaged charge density different (CDD) along the c axis. The red and blue colors present accumulated and depleted electron regions, respectively. The size of (a) is 2.3 nm × 2.3 nm. 78

Figure 5.8: Effect of trapped charge on the edge of ML ReSe₂ on BLG. (a-b) STM images of ML ReSe₂ on BLG taken at bias voltages of 1.5 V (in conduction band of ReSe₂) and 0.3 V (“in-gap” bias voltage), respectively. The edge feature is significantly enhanced at “in-gap” bias voltage. The size of STM images in (a) and (b) are 35 nm × 15 nm. (c) The line profiles obtained from bias dependent STM images of the edge. The solid (dotted) black and orange line profiles are obtained from STM taken at positive (negative) bias voltages locating within the energy gap and conduction (valence) band of ReSe₂. (d) The STS measured along a line crossing the edge of ML ReSe₂ on BLG from position “I” to “IV” marked in (a-c). All STS in (d) are converted to logarithm scale; the blue dashed lines indicate the tendency of graphene electronic structure. 80

Figure 6.1: Two process of Cu₂O surface preparation. (a) Oxidation in ambient conditions. (b) Cleaning surface inside UHV chamber. 86

Figure 6.2: Surface structure of Cu₂O(111) films. (a) Large-scale STM topography of the Cu₂O(111) surface shows well-ordered terrace structures ($V_s = 4.5$ V, $I_t = 30$ pA). (b) The line profile taken along the blue arrow in (a) showing the single step about 2.1 Å. (c) The top and side view of structure model of stoichiometric Cu₂O(111) surface. The red, light blue, dark blue, yellow, and white circles represented for coordinatively unsaturated oxygen (O_{CUS}), coordinatively unsaturated copper (Cu_{CUS}), coordinatively saturated copper (Cu_{CSA}), coordinatively saturated oxygen (O_{CSA}), and underneath oxygen atoms. 88

Figure 6.3: Atomic structure of Cu₂O(111) surface. (a) High-resolution STM image exhibits hexagonal structures of stoichiometric Cu₂O(111) surface ($V_s = 1.4$ V, $I_t = 30$ pA).

(b) STM image of stoichiometric $\text{Cu}_2\text{O}(111)$ surface is simulated at +1 V with the revised Chen's approach using a sharp tip apex on $\text{W}(110)$. (c) High-resolution STM image exhibits triangular structures of stoichiometric $\text{Cu}_2\text{O}(111)$ surface ($V_s = 0.2$ V, $I_t = 30$ pA). (d) STM image of stoichiometric $\text{Cu}_2\text{O}(111)$ surface is simulated at +1 V with the Tesoff-Hammann method. Top-view structural model of the stoichiometric $\text{Cu}_2\text{O}(111)$ surface is overlaid on the STM and simulated STM images. The bright line features in experimental and simulated STM images are denoted as dashed lines in (a) and (b). Image size of (a) and (b) are $3 \text{ nm} \times 3 \text{ nm}$ 89

Figure 6.4: Intrinsic defects in the $\text{Cu}_2\text{O}(111)$ surface. (a) Two different defects labelled defects A and B are observed in STM topography (size: $30 \times 30 \text{ nm}^2$). (b) and (d) High-resolution STM images of the locations marked by yellow (defect A) and white (defect B) boxes in (a), respectively (size: $4 \times 4 \text{ nm}^2$). All STM images are produced at $V_s = 1.6$ V and $I_t = 30$ pA. Simulated STM images (using revised Chen's approach) are shown for defect A (at +1.5 V) in (c) and defect B (at +1.5 V) in (e) with surface atomic structures. (c) For defect A, one Cu_{CUS} vacancy defect exists on the $p(2 \times 2)$ Cu_2O surface supercell. (e) For defect B, the STM images are simulated with one Cu adatom (upper) and three-adatom (lower) models to confirm possible Cu clusters on the $p(3 \times 3)$ surface supercell. The atomic structures are overlapped to the simulated STM images. The Cu, O, and Cu_n atoms are depicted as white, red, and turquoise circles, respectively. 91

Figure 6.5: Bias polarity dependence of STM images at the same location. Cu vacancies (V_{Cu}) and Cu clusters (Cu_n) present different contrast behavior in (a) empty and (b) filled state images (size: $15 \times 15 \text{ nm}^2$). 94

Figure 6.6: Electronic structure of V_{Cu} . dI/dV spectroscopy taken at V_{Cu} (red curve) and a defect-free area (blue curve) (a) on linear scale and (b) on log scale. The I-V spectra are obtained with initial set-current 50 pA at 2.5 V (feedback off) and dI/dV signal is simultaneously measured by a typical lock-in technique (modulation amplitude of 10 mV and frequency of 1.2 kHz). 96

List of Table

Table 2.1: Tunneling matrixes of different tip states.	13
Table 2.2: Formulars of corrugation amplitude depending on different tip states.	14
Table 5.1. The intensity of CDW phase in topography and dI/dV mapping. R is the intensity ratio ($R = I_{CDW} / I_{lattice}$) of CDW peaks (I_{CDW} , red arrows) to VSe ₂ hexagonal lattice peaks ($I_{lattice}$, white arrows) in the FFT images of Figs. 5.3(b,d). R_T and R_M are the ratio values obtained from FFT images of topography and dI/dV mapping, respectively.	68
Table 6.1. Defect formation energy of single and paired surface defects of Cu₂O(111).	92

Chapter 1

Overview of two-dimensional materials

Two-dimensional (2D) materials are substances where the electron is confined in one direction (1D confinement) and exhibit unique physical properties. In the world of 2D materials shown in Fig. 1.1, we can categorize them into two types whose bulk materials are either non-layered materials or layered materials. The non-layered materials, in which the bonding between elements are all chemical, include metals (Sn, Au,...),^[1,2] a metal chalcogenides (PbS, CuS, Cr₂S₃)^[3-5], metal oxides (TiO₂, ZnO, ...),^[6] etc. ^[7]. On the other hand, the layered materials are substances in which the intralayer bonds are chemical while the interlayer bond between two adjacent slabs is van der Waals bond, so-called layered van der Waals (vdWs) materials. Some categories of the layered vdWs materials are shown in Fig. 1.1, e.g, one component (graphite, black phosphorous),^[8,9] two components (chalcogenides: SnSe, SnS, GaSe, InSe, etc.,^[10-14] transition metal chalcogenides: MoS₂, MoSe₂, VSe₂, ReSe₂, etc.,^[15-20] metal oxides: MoO₃, etc.,^[21] halides: CrX₃ (X = Cl, Br, I), RuCl₃, etc.),^[22-28] and three components (FeOCl,^[29] CrSiTe₃,^[30] Fe_nGeTe₂ (n=3,4,5),^[31] (Fe₂Ge)_nFeGeTe₂ (n=1, 2,3),^[32] etc.).

To fabricate a 2D material, there are two well-known strategies/approaches, namely bottom-up and top-down. The bottom-up approach assembles the atoms in a very thin layer by using both chemical vapor transport and physical vapor transport.^[33-37] This method can be used for both non-layered materials and layered van der Waals (vdWs) materials. The top-down approach which was commonly applied to the layered van der Waals (vdWs)

materials as mechanical exfoliation,^[38–47] ion exfoliation,^[48,49,57,58,50,50–56] and oxidation exfoliation,^[59–63] reducing the thickness of the bulk material to single or few atoms thick (typically less than 5nm). For example, graphene, MoS₂ and black phosphorene can be synthesized from their bulk materials by using a simple scotch tape technique.

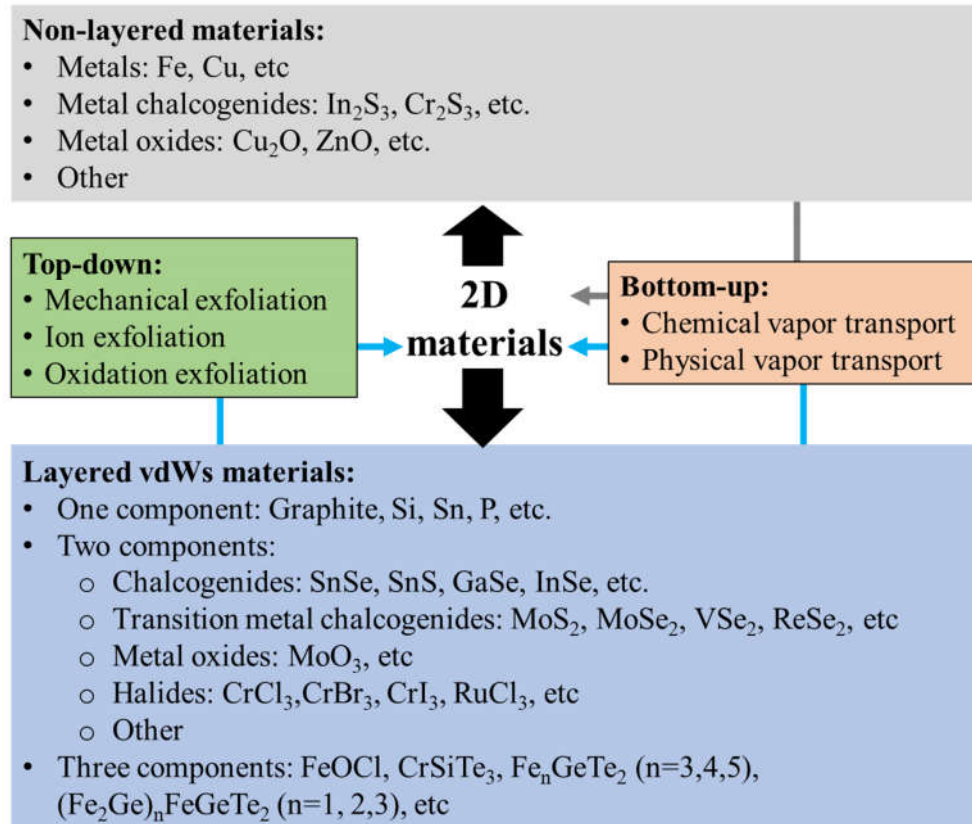


Figure 1.1: Overview of two-dimensional materials world and the fabrication methods.

After the discovery of graphene by simple mechanical exfoliation in 2004, the layered vdWs materials have been attracted many researchers. Graphene exhibits unique physical properties such as ultrahigh carrier mobility at room temperature, quantum hall effect, etc. Although graphene has shown great promise due to its ultrahigh electron mobility, its electronic application is still limited because of its absence of bandgap.^[64]

Instead, the emerging 2D semiconducting materials, such as layered chalcogenides, black phosphorous, transition metal dichalcogenides, are good candidates because of the tunable bandgap with high carrier mobility.^[65] Besides, some magnetic layered materials have been recently synthesized for the demands of making 2D magnets without killing ferromagnetism.^[66]

In the 2D limit, the surface structure plays a prominent role in physical properties. Scanning tunneling microscopy/spectroscopy (STM/S) is a powerful tool to investigate the surface properties of 2D materials at an atomic level. STM and STS provide the local electronic density of states and surface morphologies of the sample. From STM results, the quasi-particle band gap, defect, localized metallic, semiconducting behavior are revealed. This reason motivates us to investigate the atomistic and electronic structures from the surface of some vdWs layered materials via scanning tunneling microscopy.

Chapter 2

Scanning tunneling microscope

2.1 A back ground theory of scanning tunneling microscopy

2.1.1 Tunneling junction in STM

In this section, we present elementary theories of tunneling through a one-dimensional potential barrier, which will provide us an understanding of the basic physics in STM. We first consider a simple problem of a free electron in an infinite square well potential showing in Fig. 2.1.

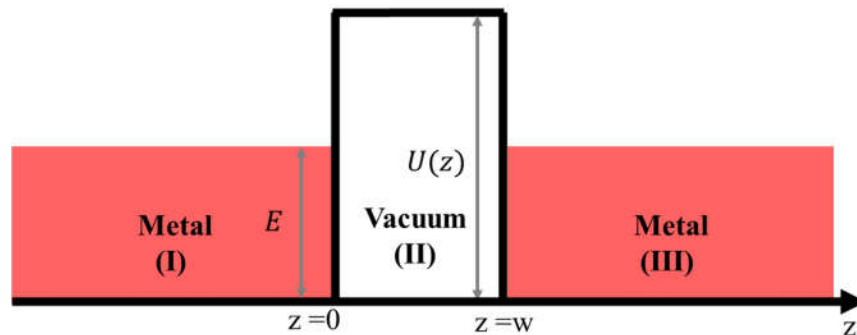


Figure 2.1: Metal-vacuum-metal problem in classical mechanics and quantum mechanics point of views.

In classical mechanics point of view, an electron in a potential $U(z)$ is described

$$\frac{p^2}{2m} + U(z) = E. \quad (2.1)$$

where p , m , E are momentum, mass, and energy of the electron, respectively.

In regions (I) or (III), if $E > U(z)$, the electron has a non-zero momentum $p = \sqrt{2m(E - U(z))}$. In other hand, if $E < U(z)$ the electron cannot penetrate into region (II). Thus, region (II) becomes forbidden region of electron.

However, the possibility of an electron moving from left to the right in Fig. 2.1 can be calculated in quantum mechanics perspective. The electron now can be treated as a wavefunction $\psi(z)$ satisfying the Schrödinger equation,

$$\frac{\hbar^2}{2m} \frac{\partial^2 \psi(z)}{\partial z^2} + U(z)\psi(z) = E\psi(z) \quad (2.2)$$

where \hbar , z , m are Planck's constant, the position, and the electron mass. And electron is under a potential barrier $U(z)$:

$$U(z) = \begin{cases} 0 & z < 0 \quad \text{in region (I)} \\ V_0 & 0 < z < w \quad \text{in region(II)} \\ 0 & z > w \quad \text{in region (III)} \end{cases} \quad (2.3)$$

By solving Eq. 2.2 using Wentzel-Kramers-Brillouin (WKB) approximation with the corresponding potential barrier of each region in Eq. 2.3, we obtain the electron wave function as a traveling wave equation,

$$\psi(z) = \begin{cases} \psi_I(z) = Ae^{ikz} + Be^{-ikz} & z < 0 \quad \text{in region (I)} \\ \psi_{II}(z) = D_1e^{-\kappa z} + D_2e^{\kappa z} & 0 < z < w \quad \text{in region(II)} \\ \psi_{III}(z) = Ce^{ikz} & z > w \quad \text{in region (III)} \end{cases} \quad (2.4)$$

where k and κ are wave vector and decay constant, respectively.

$$\text{Wave vector: } k = \frac{\sqrt{2mE}}{\hbar} \quad (2.5)$$

$$\text{Decay constant: } \kappa = \frac{\sqrt{2m(V_0 - E)}}{\hbar} \quad (2.6)$$

We also find the probability current density (j) of each region expressed in below:

$$j = \begin{cases} j_I = \frac{\hbar k}{m} (|A|^2 - |B|^2) & z < 0 \quad \text{in region (I)} \\ j_{III} = \frac{\hbar k}{m} |C|^2 & z > w \quad \text{in region (III)} \end{cases} \quad (2.7)$$

The transmission (T) and reflection (R) coefficients can be defined as

Transmission coefficient: $T = \left|\frac{C}{A}\right|^2$

Reflection coefficient: $R = \left|\frac{B}{A}\right|^2$

From the boundary conditions, we can find the ratios of A, B and C based on the continuity properties of wave function and its derivative.

$$\begin{aligned}\psi_I(0) &= \psi_{II}(0), \text{ and } \frac{\partial}{\partial Z}\psi_I(0) = \frac{\partial}{\partial Z}\psi_{II}(0) \text{ at } z = 0 \\ \psi_{II}(w) &= \psi_{III}(w), \frac{\partial}{\partial Z}\psi_{II}(w) = \frac{\partial}{\partial Z}\psi_{III}(w) \text{ at } z = w\end{aligned}\quad (2.8)$$

Therefore, the transmission and reflection coefficients can be calculated.

$$T = \left|\frac{C}{A}\right|^2 = \frac{4\kappa^2 k^2}{(\kappa^2 - k^2)\sinh^2 \kappa w + 4\kappa^2 k^2 \cosh^2 \kappa w} \quad (2.9)$$

$$R = \left|\frac{B}{A}\right|^2 = \frac{(\kappa^2 + k^2)\sinh^2 \kappa w}{(\kappa^2 - k^2)\sinh^2 \kappa w + 4\kappa^2 k^2 \cosh^2 \kappa w} \quad (2.10)$$

To apply this elementary model of tunneling problem to an STM configuration, two metal plates are now the sample and the tip. The work function (ϕ) is well known as the energy amount required for an electron exciting from Fermi level (E_F) to vacuum level. By assuming that the work function of tip is the same as work function of sample, tunneling current is not available with zero voltage applied between the junctions. Therefore, a bias voltage applied to one of electrodes is necessary to have tunneling current. An example of tunneling junction with a negative bias (V) applied to the sample is illustrated in Fig. 2.2. In this case, the tunneling current flows from sample to the tip with a given bias eV.

Likewise, the sample's local density of states (LDOS) in given interval near energy E can be defined as

$$\rho(z, E) = \frac{1}{\varepsilon} \sum_E |\psi_n(z)|^2, \quad \rho(0, E) = \frac{1}{\varepsilon} \sum_E |\psi_n(0)|^2 \quad (2.15)$$

Where $\rho(0, E_F)$ is the LDOS near E_F in the sample. The tunneling current is, thus, expressed below:

$$I \propto V \rho(0, E_F) e^{-2\kappa z} \quad (2.16)$$

Eq. 1.16 tells that LDOS of sample near E_F can be measured by changing applied bias voltage (V) to the junction and measuring the tunneling current (I). In general, the STM images include both surface morphology and LDOS of sample. For this reason, STM measurements can provide very insight information of sample surface.

2.1.2 The Bardeen's approach to tunneling current

The previous section is the simplification of tunneling problem which allows to use single electron wave function. However, such description does not consider the effects of multiple electrons to tunneling current. An approximation method provided by John Bardeen can approach to more realistic system. In this method, the tunneling process is treated due to transitions from single particle states locating on one side of the vacuum barrier into states on the other side. In STM configuration, two sides of vacuum barrier can be understood as tip and sample.

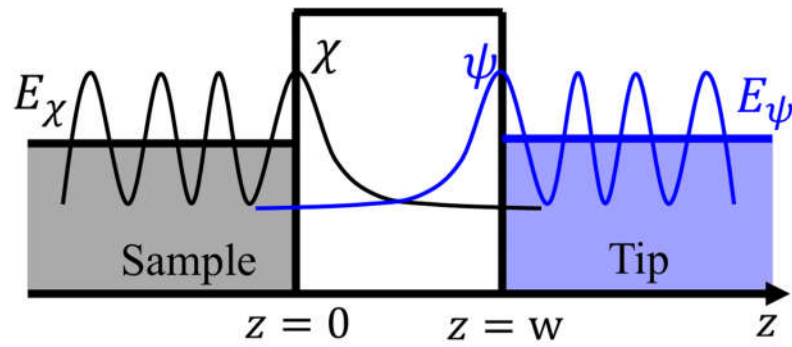


Figure 2.3: Bardeen's approach to tunneling current. Tunneling current is originated by overlapping of two electron wave functions for sample (χ) and tip (ψ).

As illustrated in Fig. 2.3, the tunneling current is originated by overlapping of two electron wave functions for sample (χ) and tip (ψ). In Bardeen's approach, Schrödinger equation is first solved using time dependent perturbation theory. Bardeen's approximation produces reliable results for systems which are well separated, i.e., systems where the overlap of the two wave-functions (χ) and (ψ) is small.^[67]

To evaluate tunneling matrix element, some additional approximation is introduced in Bardeen's approach. It is assumed that the potential U_S to be zero in the tip region and U_T should be zero in the sample region. Furthermore, in vacuum region, the potential U_S and U_T differ from zero. Because of this assumption, Bardeen's approximation becomes better for tunneling processes through a wider barrier, or a larger tip-sample distances.

Accordingly, the tunneling matrix element in one-dimensional form can be determined by integration over surface between the tip and sample,

$$M = \frac{2}{2m} \int_{\Sigma} (\chi \nabla \psi - \psi \nabla \chi) \cdot d\mathbf{S} \quad (2.17)$$

Furthermore, the rate of electron transfer across the barrier, or probability of the transition of an electron from sample state into a tip state is expressed by Fermi's Golden Rule,

$$p^{S \rightarrow T} = \frac{2\pi}{\hbar} |M|^2 \delta(E_\psi - E_\chi) \quad (2.18)$$

The presence of $\delta(E_\psi - E_\chi)$ implies that elastic tunneling from sample state (χ) into a tip state (ψ) is accounted with $E_\psi = E_\chi$ only.

In addition, the Fermi distribution function can be used to describe the probability of an electron occupied in an energy state (E),

$$f(E) = \frac{1}{1 + e^{(E - E_F)/k_B T}}. \quad (2.19)$$

As mentioned in previous section, a bias voltage (V) is applied to the sample in STM configuration. Summing over all relevant states including sample states (ψ) and tip states (χ) gives the tunneling current.

$$I = \frac{4\pi e}{\hbar} \int_{-\infty}^{+\infty} [f(E_F - eV + \epsilon) - f(E_F + \epsilon)] \rho_s(E_F - eV + \epsilon) \rho_T(E_F + \epsilon) |M|^2 d\epsilon \quad (2.20)$$

ρ_s are the densities of states (DOS) of sample and ρ_T is DOS of the tip.

It should be noted that the Fermi distribution can be used at any finite temperature because the states near the Fermi energy significantly contribute to the tunneling current. In the case of very low temperature; i.e, $k_B T$ can be smaller than resolution of energy required in the experiment, the step function can be used instead of Fermi distribution function.^[67] The tunneling current, therefore, becomes:

$$I = \frac{4\pi e}{\hbar} \int_0^{eV} \rho_s(E_F - eV + \epsilon) \rho_T(E_F + \epsilon) |M|^2 d\epsilon \quad (2.21)$$

From Eq. 2.21, to calculate tunneling current, the tunneling matrix elements (M) also need to be evaluated.

2.1.3 Tunneling matrix

Bardeen's tunneling theory have been presented in section 2.1.2 to understand the

essential physics of STM. Another application of this approach is the evaluation of the tunneling matrix elements, recalled:

$$M = \frac{2}{2m} \int_{\Sigma} (\chi \nabla \psi - \psi \nabla \chi) \cdot d\mathbf{S} \quad (2.17)$$

Bardeen's matrix element is the interaction energy due to the overlap of the two unperturbed states and has the dimension of energy. Furthermore, this tunneling matrix is dominantly affected by the force between the tip and the sample under normal STM operating conditions. Therefore, an explicit form of tunneling matrix elements is important in the quantitative understanding of STM.

Evaluating the tunneling matrix elements with respect to STM has been investigated by many authors.^[67] However, the commonly used methods are introduced by Tersoff-Hamann and Julian Chen which will be discussed below.

The previous sections lead two important points of tunneling current. First, from Eq. 2.16, the wave-function decays exponentially into the vacuum so that only the orbitals localized at this outermost tip atom will be dominantly contributed to tunneling process. Second, the tunneling current depends on the overlap of the wave-functions of the tip and the sample as described in Eq. 2.17. Accordingly, Tersoff-Hamann's model suggests that only the outermost atom at the apex tip, which has a s-wave form, affects to tunneling current. Based on this method, the Bardeen's tunneling matrix can be calculated:

$$M = \frac{2\pi C}{\kappa m} \psi(\mathbf{r}_0) \quad (2.22)$$

The tunneling current, therefore, becomes.

$$I \propto \int_{-\infty}^{+\infty} [f(\epsilon) - f(\epsilon + eV)] \rho_s(\epsilon, \mathbf{r}_0) \rho_T(\epsilon + eV) |M|^2 d\epsilon \quad (21.23)$$

$\rho_T(\epsilon + eV)$ is assumed to be constant while $\rho_s(\epsilon, \mathbf{r}_0)$ can be written as,

$$\rho_s(\epsilon, \mathbf{r}_0) = \sum |\psi(\mathbf{r}_0)|^2 \delta(\epsilon - \epsilon_s) \quad (2.24)$$

$\rho_s(\mathbf{r}, \mathbf{r}_0)$ is denoted for local density of state of the sample at tip apex (\mathbf{r}_0) which is the basic quantity for STM imaging.

Although this method is usually successful in explanation of STM images, but it fails in some cases. For examples, it cannot explain the atomic resolution observed in closed packed metal surface. Another problem is that the decay-constants for the wave-functions of the tip and the sample are different with the high voltage bias ranges. Furthermore, even Bardeen's approximation does not hold for larger voltages because the basic assumption of the separation of the potentials is in a way that the tip potential is zero in the sample region and vice versa. Thus, this model can only be trusted for low bias voltages below 1V.

Although Tersoff-Hamann model provides very simple way to calculate the tunneling matrix and elucidation of STM topography, the restriction of s-like tip orbitals makes this model fail in some cases. This is because the tip states can be changed by scanning conditions so that other tip states should be considered as well. For this purpose, Julian Chen proposed a method to extend the Tersoff-Hamann model for a few different tip states to obtain the different tunneling matrixes in the table 2.1.

Real tip wave functions and tunneling matrix elements

State	Wavefunction	Tunneling matrix
s	$C_{00}k_0(\kappa\rho)\sqrt{\frac{1}{4\pi}}$	$\frac{2\pi C\hbar^2}{\kappa m}\psi(\mathbf{r}_0)$
p_z	$C_{10}k_1(\kappa\rho)\sqrt{\frac{3}{4\pi}\frac{z-z_0}{\rho}}$	$\frac{2\pi C\hbar^2}{\kappa m}\frac{\partial\psi(\mathbf{r}_0)}{\partial z}$
p_x	$C_{11}^0k_1(\kappa\rho)\sqrt{\frac{3}{4\pi}\frac{x-x_0}{\rho}}$	$\frac{2\pi C\hbar^2}{\kappa m}\frac{\partial\psi(\mathbf{r}_0)}{\partial x}$
p_y	$C_{11}^e k_1(\kappa\rho)\sqrt{\frac{3}{4\pi}\frac{y-y_0}{\rho}}$	$\frac{2\pi C\hbar^2}{\kappa m}\frac{\partial\psi(\mathbf{r}_0)}{\partial y}$
d_{z^2}	$C_{20}k_2(\kappa\rho)\sqrt{\frac{5}{4\pi}\left(\frac{3}{2}\frac{(z-z_0)^2}{\rho^2}-\frac{1}{2}\right)}$	$\frac{2\pi C\hbar^2}{\kappa m}\left(\frac{\partial^2\psi}{\partial z^2}-\frac{1}{3}\kappa^2\psi\right)(\mathbf{r}_0)$
d_{xz}	$C_{21}^e k_2(\kappa\rho)\sqrt{\frac{15}{4\pi}\frac{(x-x_0)(z-z_0)}{\rho^2}}$	$\frac{2\pi C\hbar^2}{\kappa m}\frac{\partial^2\psi(\mathbf{r}_0)}{\partial z\partial x}$
d_{yz}	$C_{21}^0 k_2(\kappa\rho)\sqrt{\frac{15}{4\pi}\frac{(y-y_0)(z-z_0)}{\rho^2}}$	$\frac{2\pi C\hbar^2}{\kappa m}\frac{\partial^2\psi(\mathbf{r}_0)}{\partial z\partial y}$
d_{xy}	$C_{22}^e k_2(\kappa\rho)\sqrt{\frac{15}{4\pi}\frac{(x-x_0)(y-y_0)}{\rho^2}}$	$\frac{2\pi C\hbar^2}{\kappa m}\frac{\partial^2\psi(\mathbf{r}_0)}{\partial x\partial y}$
$d_{x^2-y^2}$	$C_{22}^0 k_2(\kappa\rho)\sqrt{\frac{15}{16\pi}\frac{(x-x_0)^2-(y-y_0)^2}{\rho^2}}$	$\frac{2\pi C\hbar^2}{\kappa m}\left(\frac{\partial^2\psi}{\partial x^2}-\frac{\partial^2\psi}{\partial y^2}\right)(\mathbf{r}_0)$

Table 2.1: Tunneling matrixes of different tip states.

Chen's method can solve some remained issues of Tersoff-Hamann's method because it can cover most of the cases related tip's effect to tunneling current. In addition, this method also strongly proves the role of tip state in appetence of STM images. Hence, this method can approach to more realistic STM measurements. The very important achievement of Chen's method is the atomic corrugation amplitude in STM images. With different orbital wavefunction of tip (tip states), the different formulars of corrugation amplitude are obtained, as shown in table 2.2.

The theoretical corrugation amplitudes for surfaces with a tetragonal symmetry

Tip	Sample	Corrugation amplitude	
s	s	$\frac{16\kappa}{\gamma^2} e^{-\beta z}$	(1)
s	p_z	$\left(\frac{\gamma}{2\kappa}\right)^2 \frac{16\kappa}{\gamma^2} e^{-\beta z}$	(2)
s	d_{z^2}	$\left(\frac{3}{2} \frac{\gamma^2}{4\kappa^2} - \frac{1}{2}\right)^2 \frac{16\kappa}{\gamma^2} e^{-\beta z}$	(3)
p_z	s	$\left(\frac{\gamma}{2\kappa}\right)^2 \frac{16\kappa}{\gamma^2} e^{-\beta z}$	(4)
p_z	p_z	$\left(\frac{\gamma}{2\kappa}\right)^4 \frac{16\kappa}{\gamma^2} e^{-\beta z}$	(5)
p_z	d_{z^2}	$\left(\frac{\gamma}{2\kappa}\right)^2 \left(\frac{3}{2} \frac{\gamma^2}{4\kappa^2} - \frac{1}{2}\right)^2 \frac{16\kappa}{\gamma^2} e^{-\beta z}$	(6)
d_{z^2}	s	$\left(\frac{3}{2} \frac{\gamma^2}{4\kappa^2} - \frac{1}{2}\right)^2 \frac{16\kappa}{\gamma^2} e^{-\beta z}$	(7)
d_{z^2}	p_z	$\left(\frac{\gamma}{2\kappa}\right)^2 \left(\frac{3}{2} \frac{\gamma^2}{4\kappa^2} - \frac{1}{2}\right)^2 \frac{16\kappa}{\gamma^2} e^{-\beta z}$	(8)
d_{z^2}	d_{z^2}	$\left(\frac{3}{2} \frac{\gamma^2}{4\kappa^2} - \frac{1}{2}\right)^4 \frac{16\kappa}{\gamma^2} e^{-\beta z}$	(9)

Table 2.2: Formulars of corrugation amplitude depending on different tip states.

From the table in table 2.2, the STM topography might look different with different tip states. For example, sample surface with the outermost atoms in p_z states are imaging by different tip states; i.e, $d_{x^2-y^2}$ -state and d_{z^2} -state. Using formular 2 and 8 in Table 2.2, we can simply tell the atomic corrugation is increased with d_{z^2} -tip state, as illustrated in Fig. 2.4.

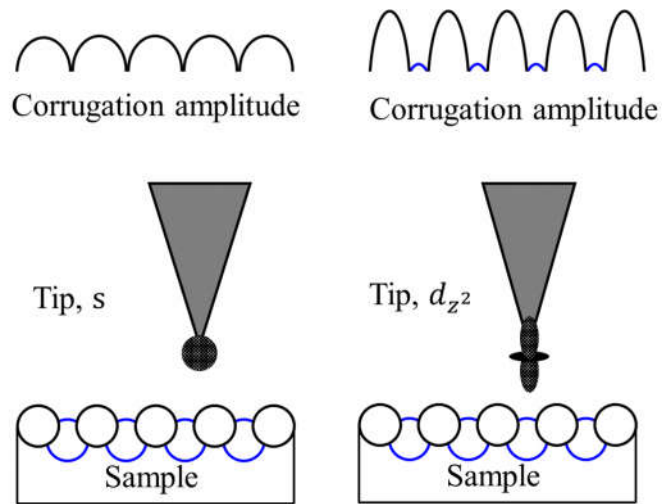


Figure 2.4: An example of tip states effect to atomic corrugation in STM image. Simple picture of the corrugation increased by a ‘sharper’ d_{z^2} -wave tip orbital as compared to s orbital.

We sometime obtained different feature of STM topography images for the same surface with the same scanning conditions (bias, setpoint). For example, the tip state effect on STM topography is presented in Appendix A.

2.2 Scanning tunneling microscope

Based on tunneling theory, the Scanning tunneling microscope (STM) was invented by Binnig and Rohrer and implemented by Binnig, Rohrer, Gerber, and Weibel.^[67] STM is a powerful technique that can directly resolve the atomic features of the sample surface. If the astronomical telescope is able to speculate on landscape of planet, the STM can image morphology of surface at atomistic level.

2.2.1 STM mechanism and two scanning mode

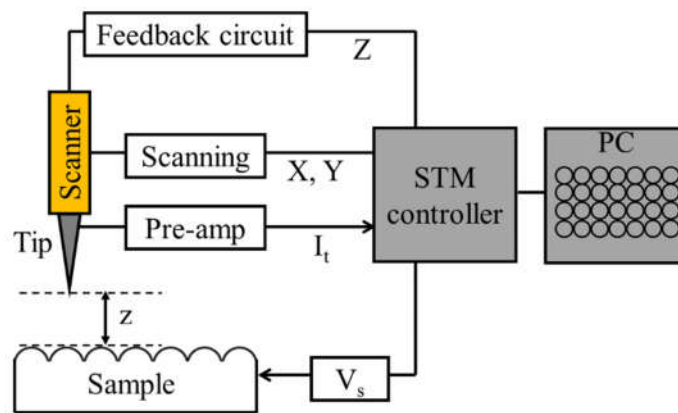


Figure 2.5: A schematic diagram of the scanning tunneling microscope.

To explain the operation of STM in a simplest way, a schematic including main parts of STM is shown in Fig. 2.5. To generate tunneling current between a metallic tip and sample, some conditions are needed: a bias voltage (V_s) is applied to sample, and the tip is close to the sample surface. The tip is brought close to the sample surface via “coarse approach” process. When the “coarse approach” is finished, the required tunneling current is reached and detected by feedback loop, the tip-sample distance (z) is within a few angstroms. The tip is now ready for “scanning” process. The tip motions are controlled by bias voltages applied to the scanner (X, Y, Z). It depends on either constant height or constant current mode,

the tip motions are maintaining either the tip-sample distance (z) or tunneling current, respectively. The tunneling signal is measured as the function of tip location (along lateral directions (X,Y)) and converted to voltage signal via pre-amplifier. After one scanning, a $(n \times n)$ matrix of tunneling signal is stored in personal computer (PC) and displayed as the contour plot which is so called “STM image”. The higher values of $n \times n$, the better resolution of STM topography.

To obtain STM image, the tip can be controlled by two modes: “constant height mode” and “constant current mode”, as shown in Fig. 2.6. In constant current mode, the tunneling current is maintained as a constant value by changing the tip-sample distance (z) with available feedback loop. The path of tip is then reflecting the sample surface information. On the other hand, in constant height mode, the tip-sample distance (z) is kept constantly by disabling feedback loop so that tunneling current is changed accordingly to corrugation of sample surface.

It is noted that the feedback loop is enable in constant current mode, a small-time delay is needed. For this reason, the slower and safer scanning is preferred in constant current mode than in constant height mode. To avoid crashing of tip, constant current mode is usually used in the unknown surfaces.

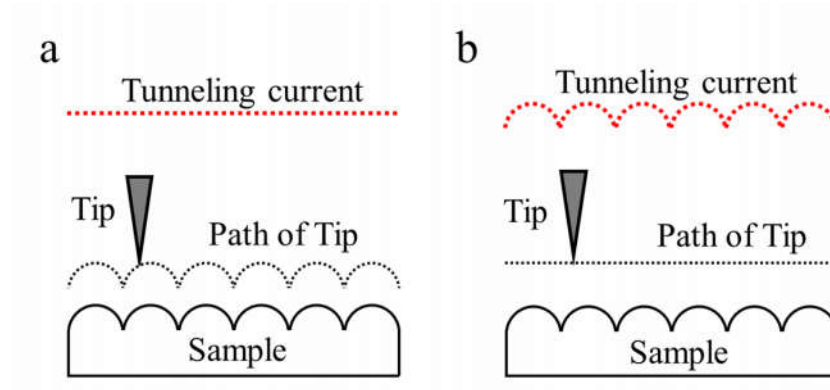


Figure 2.6: Two operation modes for STM. (a) current constant and (b) height constant.

2.2.2 Scanning tunneling spectroscopy

From Eq. 2.20, if the DOS of tip (ρ_T) and the tunneling matrix (M) are constants for the considered energy ranges, the tunneling current becomes

$$I \propto \frac{4\pi e}{\hbar} \int_0^{eV} \rho_s(E_F - eV + \epsilon) d\epsilon. \quad (2.25)$$

Furthermore, the differential tunneling conductance dI/dV provides the sample's DOS:

$$\frac{dI}{dV} \propto \rho_s(E_F - eV) \quad (2.26)$$

Eq. 2.26 tells that we can investigate electronic properties of sample surface using STM. This measurement is called scanning tunneling spectroscopy (STS), will explain right below.

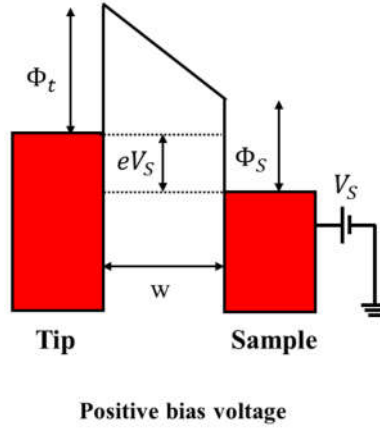


Figure 2.7: The STM tunneling process with positive bias voltage applied to sample.

One example of STM tunneling process is shown in Fig. 2.7. We first need to understand I-V spectroscopy measurement which is the most popular one. Before measuring the I - V spectrum, we must disable the feedback loop to fix the tip-sample distance (w) and then the tunneling current is recorded while sweeping sample bias. Using the Wentzel-Kramers-Brillouin (WKB) approximation method, the tunneling current can be expressed with independent position,

$$I(V, w) = \int_0^{eV} \rho_s(E_F + eV) \rho_T(E_F) \exp \left[-2w \sqrt{\frac{2m}{\hbar^2} \left(\frac{\phi_s + \phi_T}{2} - eV \right)} \right] d. \quad (2.27)$$

Assuming that tip's density of state is constant,

$$I(V, w) \propto \int_0^{eV} \rho_s(E_F + eV) \exp \left[-2w \sqrt{\frac{2m}{\hbar^2} \left(\frac{\phi_s + \phi_T}{2} - eV \right)} \right] d \quad (2.28)$$

If ρ_s is faster changing than the exponential function, then the dI/dV term will become:

$$\frac{dI}{dV} \propto \rho_s(E_F + eV) \exp \left[-2w \sqrt{\frac{2m}{\hbar^2} \left(\frac{\phi_s + \phi_T}{2} - eV \right)} \right]. \quad (2.29)$$

Thus, the local density of states (LDOS) of a sample can be extracted from the numerical derivative of an I - V spectrum (dI/dV).

2.2.3 Measure dI/dV using lock-in amplifier

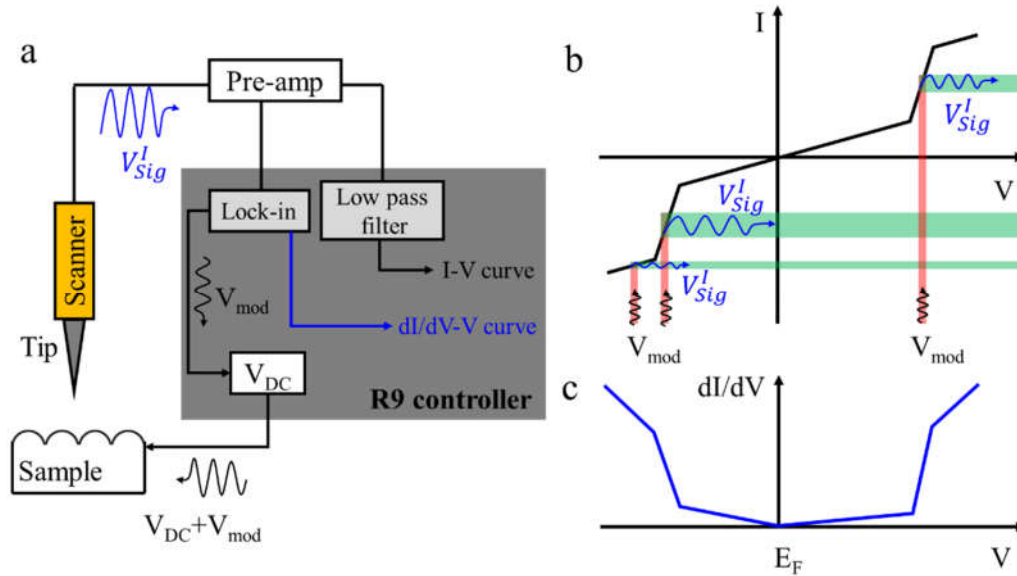


Figure 2.8: dI/dV measurement using lock-in amplifier in STM. (a) A schematic of experimental set up. (b) I/V curve is obtained together with (c) dI/dV curve from output of lock-in amplifier.

In technical, we can directly measure the LDOS of sample by lock-in amplifier. STM spectroscopy become more powerful with help of the lock-in amplifier, e.g, we can obtain both topography image together with mapping of LDOS in real space at a given bias at the same time.

To measure DOS, the lock-in amplifier adds a small sinusoidal voltage modulation ($V_{mod} = V_0 \sin(\omega_r t)$) with V_0 is set to about 1% to 10% with respect to the total bias voltage sweep range which is defined as the difference between the initial value and final value of measuring bias voltages. This modulation signal causes a sinusoidal form in tunneling signal. The slop of I/V curve corresponds to modulated current amplitude.

The measured tunneling signal (I_t) is combined of real and noise signals. For

convenience, this tunneling signal is converted to voltage signal (V_{input}^I) by preamplifier before inputting data into lock-in amplifier:

$$V_{input}^I = V_{sig}^I(t) + V_{DC}^I + V_{noise}^I(t) \quad (2.30)$$

With, $V_{sig}^I(t) = V_{sig}^I \sin(\omega_r t + \theta_{sig})$ is the voltage signal affected by small sinusoidal voltage modulation; V_{DC}^I is time independent and affected by setpoint of tunneling currents; and $V_{noise}^I(t) = V_n^I \sin(\omega_n t + \theta_n)$ is voltage signal of system noise background conditions. The output signal of lock-in amplifier is obtained after multiplying V_{input}^I signal with $V_{ref} = V_r \sin(\omega_r t + \theta_{ref})$:

$$\begin{aligned} V_{output} &= V_{ref}(t)V_{sig}^I(t) + V_{ref}(t)V_{DC} + V_{ref}(t)V_{noise}^I(t) \\ &= V_r V_{sig} \sin(\omega_r t + \theta_{sig}) \sin(\omega_r t + \theta_{ref}) + V_{ref}(t)V_{DC} + V_r V_n \sin(\omega_r t + \theta_{sig}) \sin(\omega_n t + \theta_n) \\ &= \frac{1}{2} V_r V_{sig} \cos(\theta_{sig} - \theta_{ref}) - \frac{1}{2} V_r V_{sig} \cos([\omega_r + \omega_r]t + \theta_{sig} + \theta_{ref}) + V_{ref}(t)V_{DC} + \\ &\quad \frac{1}{2} V_r V_n \cos([\omega_r - \omega_n]t + \theta_{sig} - \theta_n) - \frac{1}{2} V_r V_n \cos([\omega_r + \omega_n]t + \theta_{sig} + \theta_n) \end{aligned} \quad (2.31)$$

The V_{output} signal is filtered to remove terms depending on time, Eq. 2.31 remains only the first one:

$$V_{obtained} = \frac{1}{2} V_r V_{sig} \cos(\theta_{sig} - \theta_{ref}) \quad (2.32)$$

θ_{sig} and θ_{ref} are the phases of the measurement and reference signals. The θ_{sig} θ_{ref} value is adjusted for $\cos(\theta_{sig} - \theta_{ref}) = 1$, so-called ‘‘phase matching’’ process.

It should be noted that if the chosen modulation frequency is equal to noise frequency in the system ($\omega_r = \omega_n$), the signal V_{output} after removing time dependent term will include the noise term.

$$V_{obtained} = \frac{1}{2} V_r V_{sig} \cos(\theta_{sig} - \theta_{ref}) + \frac{1}{2} V_r V_n \cos(\theta_{sig} - \theta_n). \quad (2.33)$$

The second term in Eq. 2.32 is affected by noise signal. For this reason, we must properly choose the reference frequency frequencies should be satisfy two conditions, i.e, the reference frequency should be smaller than the current amplifier bandwidth and different from prominent noise frequency ($\omega_r \neq \omega_n$), which can be checked in the noise spectrum analyzer. If reference frequency ω_r is properly selected, we can significantly improve the

signal quality by lock-in amplifier. The measured signal in Eq. 2.32 is the expected signals of $\frac{dI}{dV}$. A schematic of experimental set up for dI/dV measurement using lock-in amplifier is shown in Fig. 2.8.

2.2.4 Overview of home built low temperature STM

In this section, an overview of home built low temperature STM based Professor Kim's design is presented in Fig. 2.9.^[68] Sample and tip are first transferred into load lock (1) and turbo (2) and rotary pumps (3) start running. After the load lock reaches a high vacuum of $\sim 10^{-9}$ Torr (usually after 2 hours depending on the volume space of load-lock), we can open the gate valve (4) and move the sample and tip into working space (5) where is always under ultra high vacuum (UHV) chamber. In UHV conditions, pressure of $10^{-10} \sim 10^{-11}$ Torr is maintained by ion pump (6) and cryostat system (7). Tip cleaning process is done at annealing stage (8). The sample surface treatment is decided based on sample characteristic. After cleaning processes, sample and tip are moved into STM head (9) for STM measurements. The STM head is kept at 79 K by liquid nitrogen in the cryostat system (7). All wires connect between STM head and R9 controller via feedthroughs (10).

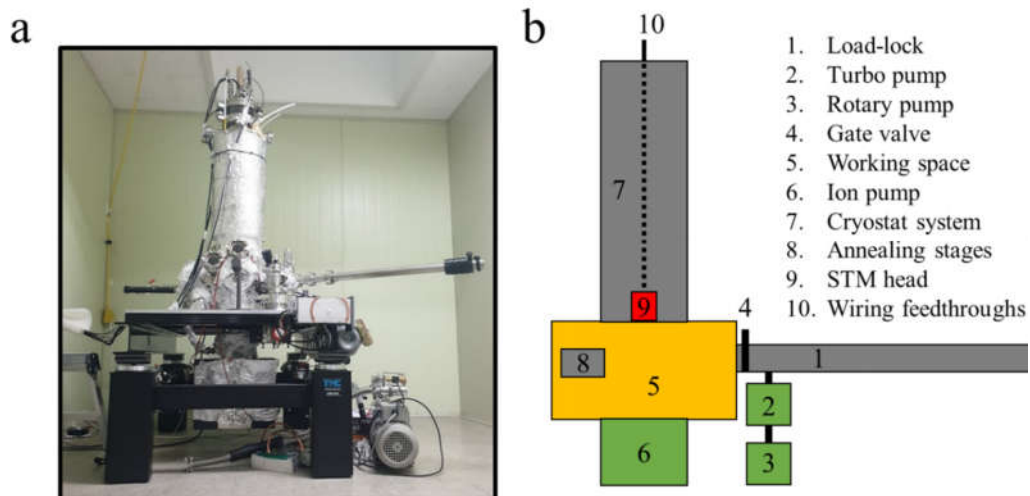


Figure 2.9: A low temperature home built STM system. (a) A picture of low temperature home built STM system. (b) A schematic of the STM chamber.

2.2.5 STM head pan type

The STM head is the most important part in STM system. In our STM system, we use STM head Pan type which is shown in Fig. 2.10. The Pan type head is one of the most widely used designs, especially in LT-STM, and the details of main parts were explained in Professor Kim's thesis.^[69]

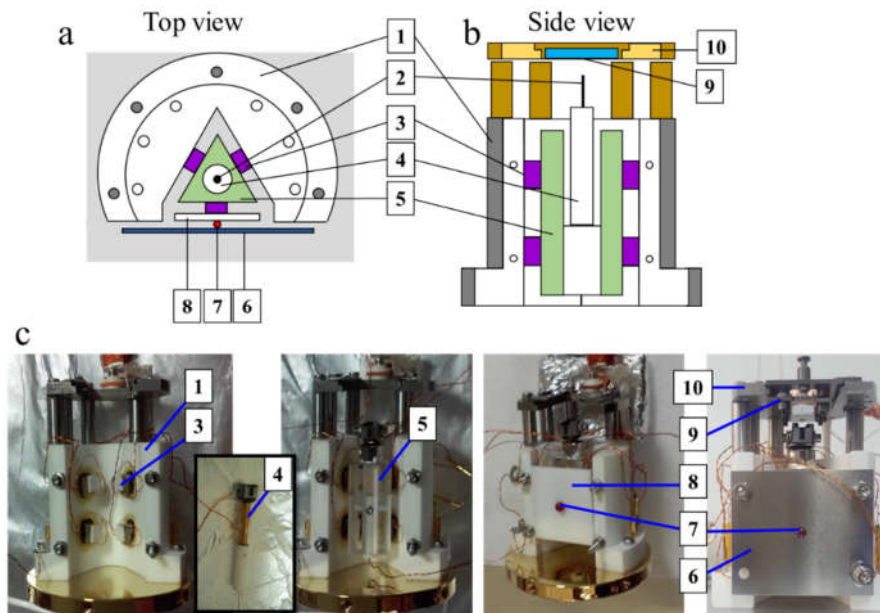


Figure 2.10: Pan type STM head. (a-b) Schematic of Pan type STM head: 1. Macor body, 2. STM tip, 3. Shear piezo stacks glued on the macor body, 4. Piezo tube scanner, 5. Sapphire prism which holds the scanner and tip, 6. Stainless steel spring plate, 7. Sapphire (or ruby) ball, 8. Macor plate, 9. Sample, 10. Sample stage. (c) The pictures of a Pan type STM head with the main parts.

Chapter 3

Layered chalcogenide materials: SnSe, SnSe_{1-x}S_x

Layered chalcogenide materials (LCMs) have been intensively studied due to their versatile physical properties when prepared in thicknesses of a few monolayers. Weak van der Waals coupling between layers allows simple mechanical exfoliation as a method to fabricate two-dimensional LCMs.^[70]

SnSe is a layered chalcogenide material (LCM) with ultra-high thermoelectric performance. Zhao *et al.* reported that SnSe single crystals showed a maximum ZT (thermoelectric figure of merit = $S^2\sigma T/\kappa$) value of 2.6 at 923 K, where S, σ , κ , T are Seebeck coefficient, electrical conductivity, thermal conductivity, and the absolute temperature, respectively.^[71,72] The ZT value is, therefore, very sensitive to carrier concentration and thermal conductivity. SnSe always exhibits p-type semiconducting behavior. To control the carrier concentration in SnSe by doping, the source of p-type characteristic in SnSe need to be understood. Besides, the higher ZT value is attributed to the lower κ of SnSe.^[73-75] Thus, SnSe_{1-x}S_x alloys are considered to be a plausible candidate to further enhance the thermoelectric properties of SnSe since the phonon scattering from foreign S atoms can further lower the thermal conductivity.^[76-82] SnSe_{1-x}S_x alloying, however, could also affect the electrical conductivity resulting in reduction of the ZT value. Therefore, it is very important to understand the alloying behavior in SnSe_{1-x}S_x at the atomic scale in order to design the optimal alloy composition without compromising other properties.

In this chapter, low temperature scanning tunneling microscope (LT-STM) measurements are used to directly probe the surface structures of SnSe and SnSe_{1-x}S_x alloys at atomic level. From STM results, origin of p-type characteristic in SnSe, and the alloying behavior of SnSe_{1-x}S_x are figured out in details. All STM results are confirmed by DFT calculation and the details are discussed in published works.^[83,84]

3.1 Structure of SnSe(S)

Both SnSe and SnS have a layered materials with orthorhombic structure (space group #62 at room temperature), as shown in Fig. 3.2a. Each layer is formed by strong covalent bonding between Se (S) and Sn atoms and consists of two-atom-thick structures on the *bc*- plane, and weak van der Waals forces hold these layers together along the *a*-axis. It should be noted that Se (S) and Sn atoms are connected in a zigzag fashion along the *bc*-plane, as shown in Fig. 3.2b. The structure of SnSe(S) is identical to that of black phosphorus with the exception that Sn atoms are slightly buckled upward in the *a*-direction.^[85] DFT calculations showed that the lattice parameters of SnSe were about $a = 11.90 \text{ \AA}$, $b = 4.24 \text{ \AA}$, $c = 4.46 \text{ \AA}$ and the SnS lattice constants were estimated to be about $a = 11.58 \text{ \AA}$, $b = 4.06 \text{ \AA}$, $c = 4.33 \text{ \AA}$. These values are similar to experimentally reported ones within about 2%.^[86]

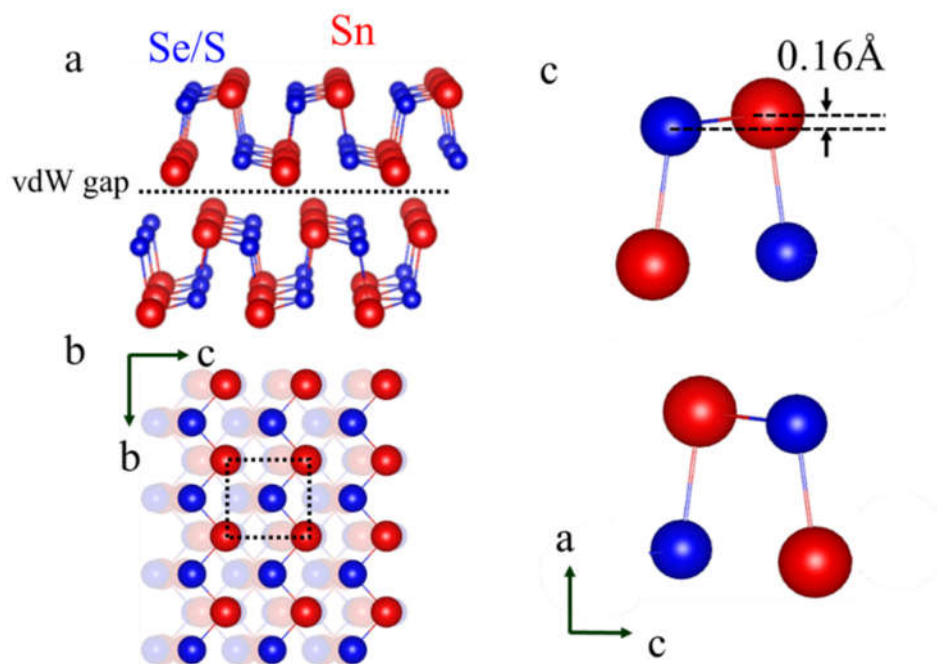


Figure 3.1: Structure information of SnSe(S). (a) A perspective view of one SnSe(S) layer. (b) Top view of SnSe(S), the red and blue balls represent Sn and Se(S) atoms, respectively. (c) The side view presents the buckling structure of the SnSe(S) layer structure.

3.2 Surface treatment

Due to the weak van der Waals forces hold layers of LCMs together, the single crystals of SnSe and $\text{SnSe}_{1-x}\text{S}_x$ ($x = 0.2, 0.4, 0.5$) samples can be easily cleaved *in-situ* by Kapton tape inside the STM chamber to obtain clean surfaces, as shown in Fig. 3.2. The Kapton tape was used because it has low outgassing under vacuum. This cleaning method can be applied for some other vdW single crystals, such as SnS, InSe, SnSe_2 , etc.

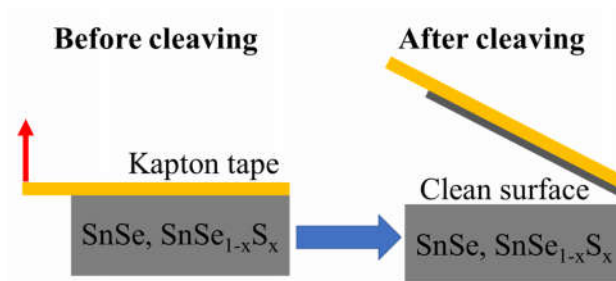


Figure 3.2: The cleaving *in-situ* process using Kapton tape for SnSe and $\text{SnSe}_{1-x}\text{S}_x$ single crystals.

3.3 Origin of p-type characteristic in SnSe

Form a large scale STM image in Fig. 3.3a, the clean SnSe surface is obtained after *in-situ* cleaving process. The clear atomic images along the cleavage plane of SnSe is shown in Fig.3.3b, instead of zigzag surface structures, the rectangular lattice is obtained in STM image.^[85] It is found that Sn atoms are only one which is resolved in STM images of SnSe because of its buckling compared to Se atoms. The atomic structure is overlaid in Fig. 3.3b, where red and blue spheres represent Sn and Se atoms. As the results, the rectangular lattice of Sn atoms is generally observed in STM image.^[85] However, in some special case of tip state, Se atoms can be resolved in STM images (Appendix A).

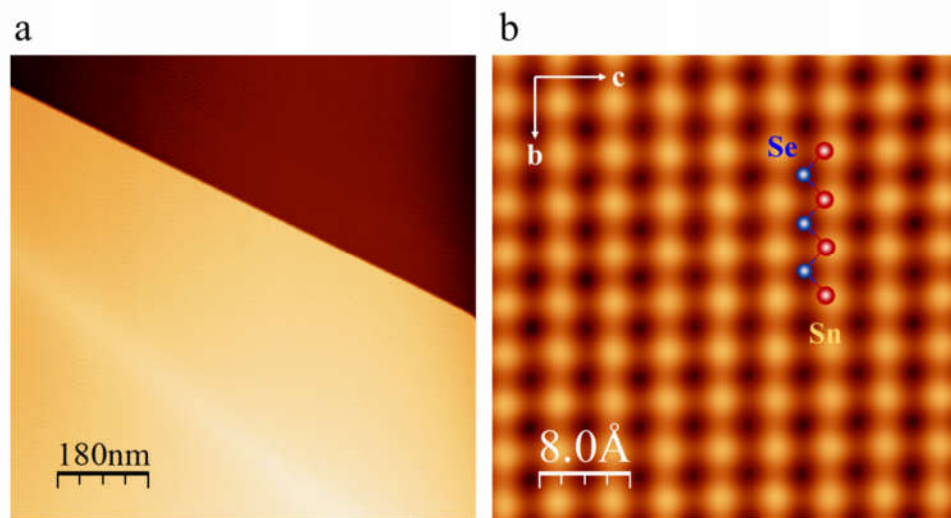


Figure 3.3: Surface structure of cleaving plane of SnSe. (a) The clean cleavage surface is obtained in STM image (3 V, 30 pA). (b) The atomic structure of SnSe along *bc*-plane (2 V, 50 pA).

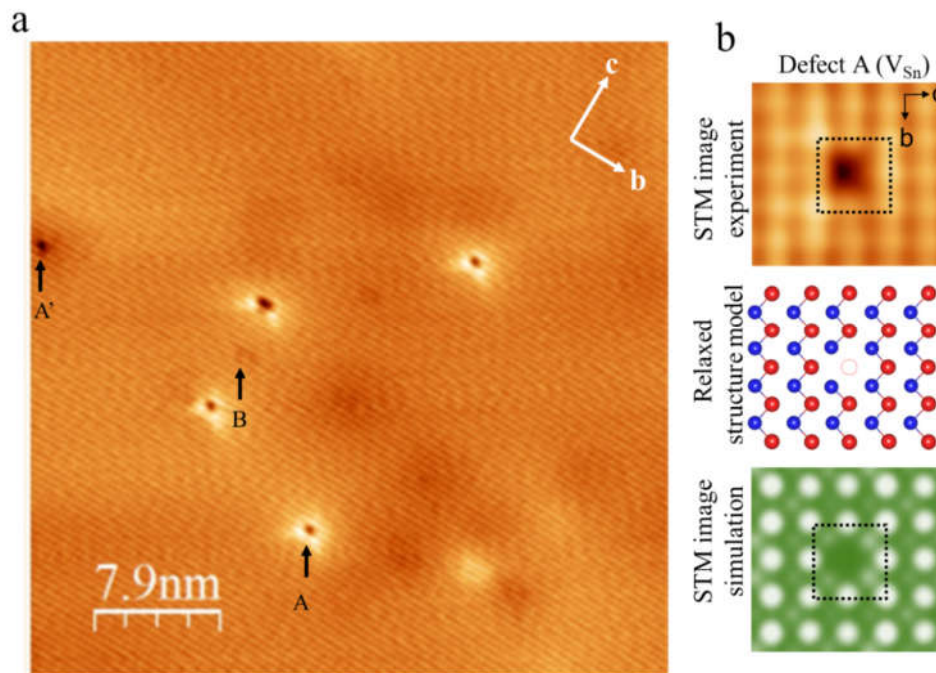


Figure 3.4: Defect nature of SnSe. (a) STM image of SnSe surface showing three kind of defect A, B, and A'. (b) STM and DFT simulation images prove that defect A is single Sn vacancy defect. Scanning condition for (a) and upper panel in (b) are (-2 V, 50 pA) and (-1.5 V and 30 pA), respectively.

After fully understand the surface structure, defect nature of SnSe is figured out via STM measurements. Three kind of intrinsic defects marked as A, B, and A' are found in Fig. 3.4a.^[83] From the STM images of defect A taken at filled-state probing in the top of Fig. 3.4b, there is an Sn atom missing in the dark position with bright contrast surrounding. This suggests that defect A is due to lacking an atom of Sn. Indeed, the relaxed structure model in Fig.3.4b (middle) and the STM image simulation (bottom) confirmed that defect A is assigned for single Sn vacancy (V_{Sn}). Besides, it is also found that defects of B and A' are single Se vacancy (V_{Se}) and multiple Se-Sn-Se vacancies ($V_{Se-Sn-Se}$) and confirmed by DFT

calculations.^[83] The fraction distribution of defect V_{Sn} is estimated as 81%, indicating that V_{Sn} is the most common defect in SnSe.^[83]

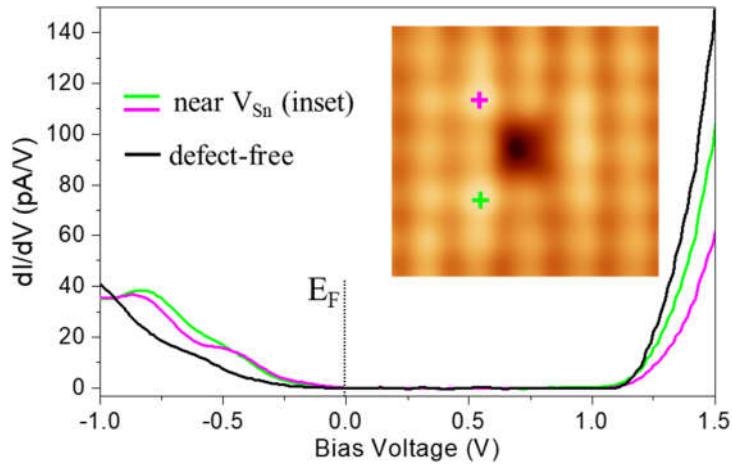


Figure 3.5: Single Sn vacancy is origin of p-type characteristic in SnSe. dI/dV tunneling spectroscopy (the green and pink curves) measured at (the green and the pink) position surrounding V_{Sn} site. The STS of V_{Sn} is directly compared with that of defect-free areas (black curve). The inset shows an STM image of Sn vacancy with the marked position.

The electronic structure of V_{Sn} is investigated by differential conductance (dI/dV) measurement. The p-type characteristics is revealed in the black spectrum, obtained at the far from defect area of the SnSe surface, in which the Fermi level (E_{F}) is closer to valence band edge than conduction band edge, as displayed in Fig. 3.5. At near V_{Sn} site marked as the green and pink plus in the STM image, the corresponded green and pink dI/dV spectra show an enhancement in DOS at filled state as compared to the black one. This indicates negatively charged behavior of V_{Sn} since they produce more holes to SnSe bulk sample. Accordingly, V_{Sn} is confirmed to be an acceptor attributing p-type properties of SnSe single

crystals. It is reported that Bi doping n-type SnSe is due to Bi dopant kills single Sn vacancy.^[74] This suggests that the most dominant defect (V_{Sn}) should be considered during synthesis SnSe materials to improve its properties for thermoelectric.^[83]

3.4 Alloying behaviors of $\text{SnSe}_{1-x}\text{S}_x$

From the structural similarity of SnSe and SnS, mentioned in section 3.1, $\text{SnSe}_{1-x}\text{S}_x$ alloys are considered. All our $\text{SnSe}_{1-x}\text{S}_x$ ($x = 0.2, 0.4, 0.6$) single crystals (i.e., substitutional solid solutions of SnSe and SnS) presented a single phase of orthorhombic crystalline structures, well oriented along the c -axis, as shown in Fig. 3.6b. The diffraction peaks were shifted to the right as the S content (x) increased, as shown in Fig. 3.6c. This result indicates that the lattice constant of $\text{SnSe}_{1-x}\text{S}_x$ decreased because lattice constants of SnS are smaller than those of SnSe. In the inset of Fig. 3.6c, the lattice constant of $\text{SnSe}_{1-x}\text{S}_x$ along the a -axis changed gradually as a function of S content (x), following Vegard's law.

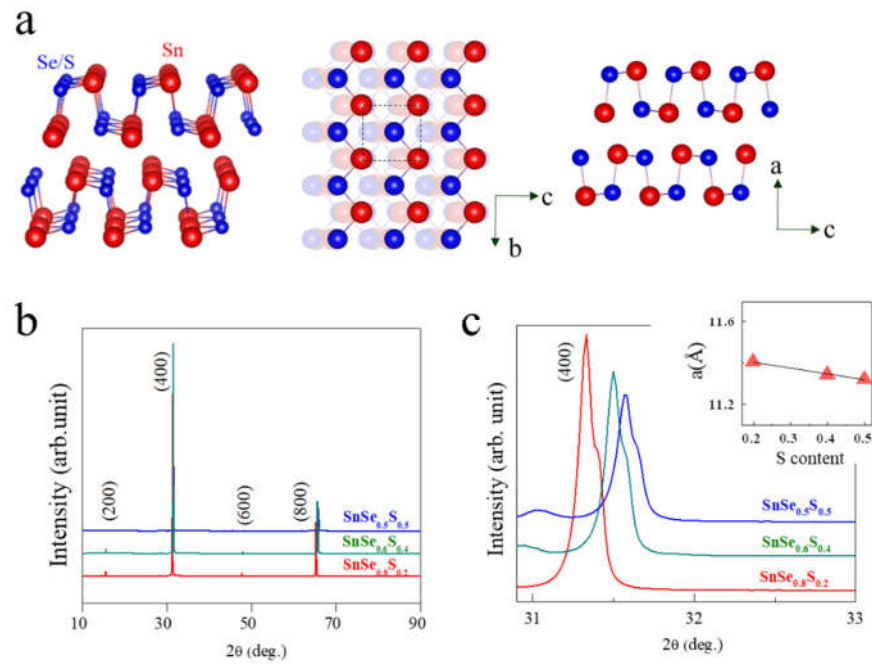


Figure 3.6: All samples of $\text{SnSe}_{1-x}\text{S}_x$ ($x = 0.2, 0.4, 0.6$) are single crystals. (a) Atomic relaxation model of SnSe and SnS (red and blue balls correspond to Sn and Se (or S) atoms, respectively). (b) XRD data of $\text{SnSe}_{1-x}\text{S}_x$ single crystals ($x = 0.2, 0.4, 0.5$) on the cleavage plane. (c) High resolution plot of the strongest diffraction peak (400). The inset shows the change in lattice constants of $\text{SnSe}_{1-x}\text{S}_x$ along the a-axis.

To directly probe how S atoms were distributed in $\text{SnSe}_{1-x}\text{S}_x$ alloys at the atomic scale, we conducted a systematic study of solid solutions of $\text{SnSe}_{1-x}\text{S}_x$ single crystals using a home-built LT-STM.^[68] A recent report showed that STM topographic images normally resolve only Sn atoms on the cleaved surfaces of SnSe due to the higher location of Sn atoms compared to Se atoms together with the dominant contribution of Sn 5p states in tunneling.^[83,85] Atomic resolved STM images of SnSe and $\text{SnSe}_{0.8}\text{S}_{0.2}$ are shown in Fig. 3.7a and b, respectively. In Fig. 3.7a, the bright extrusions correspond to Sn atoms, and Se atoms are located at the dark positions. Although only Sn atoms are visible in both images, the $\text{SnSe}_{0.8}\text{S}_{0.2}$ surface in Fig. 3.7b presents very distinctive features compared to the SnSe surface. Some areas of Sn atoms exhibited much darker contrast (or suppressed intensity) with slightly distorted lattices in $\text{SnSe}_{0.8}\text{S}_{0.2}$. This is expected due to substituted S atoms.

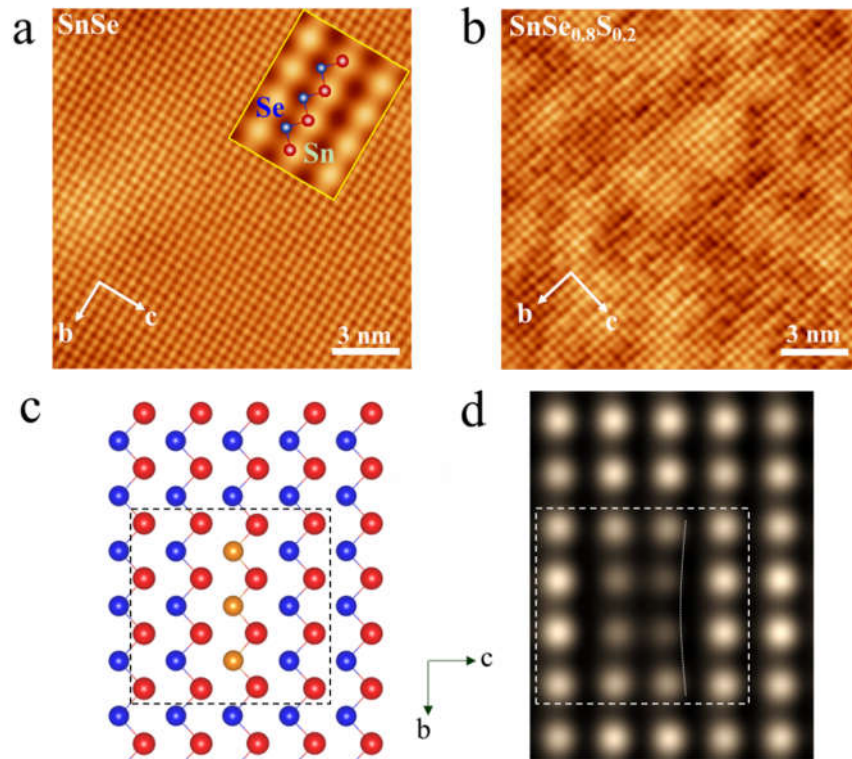


Figure 3.7: DFT simulation image confirms the substituted S atoms locating at the dark positions. (a) STM topographic images of SnSe and (b) SnSe_{0.8}S_{0.2} single crystals. The inset in (a) shows the atomic model of a SnSe cleavage surface where red and blue balls correspond to Sn and Se atoms, respectively. Tunneling conditions: (a) $V_s = -2$ V, $I_t = 50$ pA and (b) $V_s = -1.7$ V, $I_t = 80$ pA. (c) Relaxed structural model of a SnSe surface with three substituted S atoms. Red, blue, and yellow spheres represent Sn, Se, and S atoms, respectively. (d) Simulated STM image for the SnSe supercell with three substituted S atoms.

To reveal the origin of the dark contrast more clearly, we carried out DFT calculations for an atomic structure containing three S atoms. As shown in Fig. 3.7c, three Se atoms (blue spheres) were replaced by three S atoms (yellow spheres), and then the model structure was fully relaxed until the forces acting on each atom were less than 10 meV/Å. As shown in the DFT simulation image of Fig. 3.7d, nearest neighbor Sn atoms around S

atoms were slightly distorted. Such lattice distortions originate from the lattice parameter differences between SnSe and SnS. We also found that the downward arrangement of Sn atoms around S atoms resulted in much weaker intensity, which well reflects the dark areas in Fig. 3.7b. Based on the excellent agreement between the STM image and DFT simulation, we believe that dark localities of Sn atoms in the STM images are related to S substitution.

STM images were also obtained for $\text{SnSe}_{1-x}\text{S}_x$ with different S compositions. Fig. 3.8a-c present STM topographic images taken from $\text{SnSe}_{0.8}\text{S}_{0.2}$, $\text{SnSe}_{0.6}\text{S}_{0.4}$, and $\text{SnSe}_{0.5}\text{S}_{0.5}$, respectively. It should be noted that the dark areas increased with increasing content of S in $\text{SnSe}_{1-x}\text{S}_x$. This again confirms that these suppressed areas in STM images were caused by the presence of substituted S atoms. To map these dark areas, we processed the STM images in Fig. 3.8a-c as follows. Fig. 3.8a was filtered through a Fourier transformation to generate a perfect lattice image with uniform intensity. Thereafter, we subtracted the perfect lattice from Fig. 3.8a to produce Fig. 3.8d; as shown, the dark areas (mapped in red) became much more distinctive.^[87] Similarly, the dark areas in Fig. 3.8b-c are mapped in red in Fig. 3.8e-f.

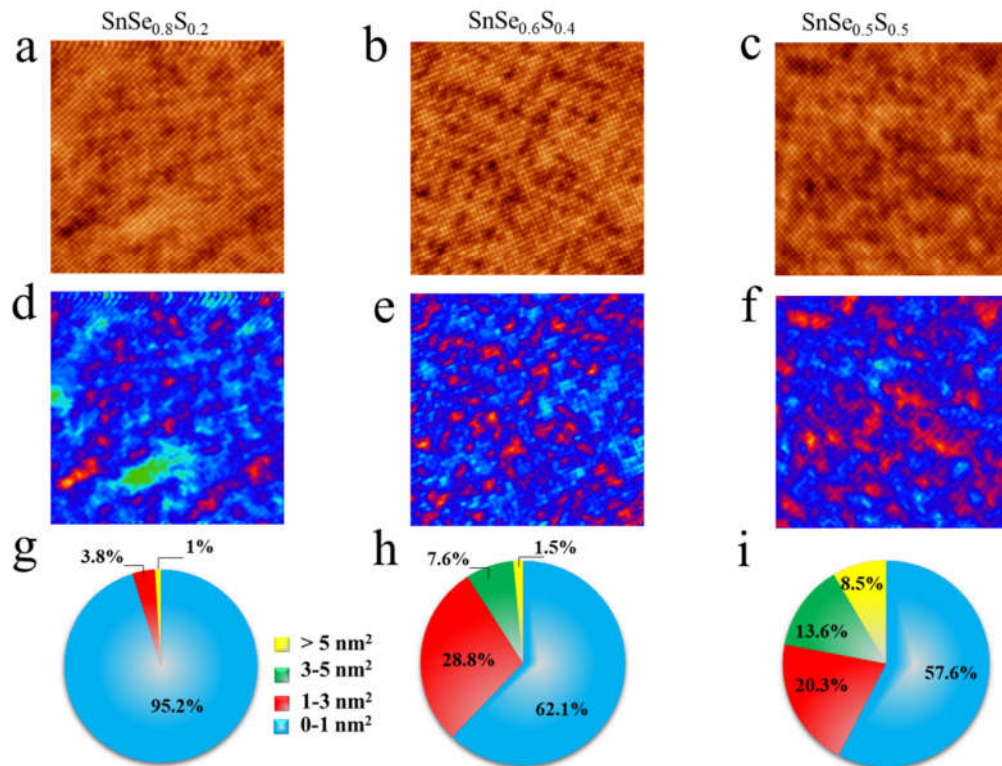


Figure 3.8: STM topography images of $\text{SnSe}_{1-x}\text{S}_x$ ($x = 0.2, 0.4, 0.5$). STM topographic images of (a) $\text{SnSe}_{0.8}\text{S}_{0.2}$, (b) $\text{SnSe}_{0.6}\text{S}_{0.4}$, and (c) $\text{SnSe}_{0.5}\text{S}_{0.5}$. All STM images are $20 \times 20 \text{ nm}$ in size with (a) $V_s = -0.9 \text{ V}$, $I_t = 60 \text{ pA}$, (b) $V_s = -1.5 \text{ V}$, $I_t = 40 \text{ pA}$, and (c) $V_s = -2.3 \text{ V}$, $I_t = 20 \text{ pA}$. The dark areas in (a-c) were mapped with a red color in (d-f) by subtracting ideal lattices with uniform intensity. (g-i) are pie charts showing fractional percentage of areal sizes counted from the red areas in (d-f).

The red areas in Fig. 3.8(d-f) indicate S substituted areas, and these are statistically counted in four different ranges of sizes in Fig. 3.8(g-i): $< 1 \text{ nm}^2$, $1-3 \text{ nm}^2$, $3-5 \text{ nm}^2$, and $> 5 \text{ nm}^2$. The numbers in the diagrams indicate the fractional percentage of real sizes counted from red areas in Fig. 3.8(d-f). As S content increased, the smallest range ($0-1 \text{ nm}^2$) of red areas decreased, while the large ranges ($3-5 \text{ nm}^2$ and $> 5 \text{ nm}^2$) increased. This result indicates

important information about the alloying behavior in $\text{SnSe}_{1-x}\text{S}_x$ single crystals, *i.e.*, S atoms are not just randomly distributed, but they tend to form local clusters of SnS.

In Fig. 3.9a, we also examined the alloying degree for S atoms and found it to be about 60% in $\text{SnSe}_{1-x}\text{S}_x$ single crystals ($x = 0.2, 0.4, 0.5$), implying that S atoms prefer to neighbor with another S atom over Se atoms.^[84] The calculated positive mixing energy for $\text{SnSe}_{1-x}\text{S}_x$ also in Fig. 3.9b suggests that $\text{SnSe}_{1-x}\text{S}_x$ has a tendency toward local phase segregation into SnSe and SnS.^[84]

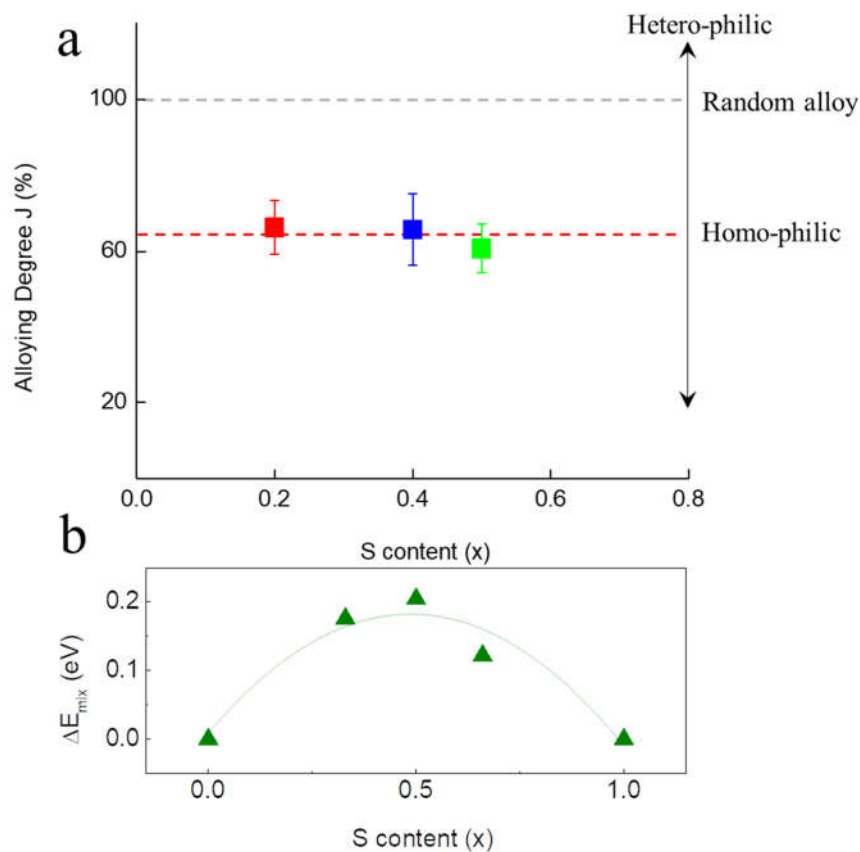


Figure 3.9: Alloy degree and mixing energy of $\text{SnSe}_{1-x}\text{S}_x$ alloys. (a) Quantitative analysis of S atom distributions in $\text{SnSe}_{1-x}\text{S}_x$ alloys. The alloying degree J for S atoms was estimated to be about 60%, which indicates that homo-atoms prefer to bond with one another rather than with hetero-atoms. (b) Mixing energies of $\text{SnSe}_{1-x}\text{S}_x$ alloys as a function of S content. The positive mixing energies indicates that $\text{SnSe}_{1-x}\text{S}_x$ has a tendency towards phase segregation into SnSe and SnS.

3.5 Summary

Based on understanding surface structure of SnSe, the defect nature in SnSe and alloying behavior of $\text{SnSe}_{1-x}\text{S}_x$ engineering in materials is studied at atomic level. Single Sn vacancy is an important factor need to consider during growth SnSe single crystal and it can be more critical for n-type doping SnSe. Besides, understanding the alloying behavior of crystalline $\text{SnSe}_{1-x}\text{S}_x$ at the atomic scale will eventually help in the design of optimized $\text{SnSe}_{1-x}\text{S}_x$ alloys with high thermoelectric properties.

Chapter 4

Magnetic vdW Materials: $\text{Fe}_{5-x}\text{GeTe}_2$

van der Waals (vdW) materials such as graphene, transition metal dichalcogenides, black phosphorous, etc., have made a great impact on various fields from fundamental science to engineering applications.^[29,88,89] Weak interlayer coupling of vdW materials allows easy mechanical exfoliation, which is ideal to control dimensionality and stacking configuration. Such degrees of freedom in sample manipulations introduce new possibilities for exploring novel materials with tailored physical properties.^[90,91] With these advantages, magnetic vdW materials have received extensive research attention in spintronics.^[92–96] Compared to conventional ferromagnets, the vdW ferromagnet provides a unique configuration of magnetic interactions due to its quasi two-dimensional (2D) nature. The pair-exchange interaction is mainly established within the 2D plane, while magnetic coupling between interlayers is weak. Therefore, the vdW ferromagnets are ideal for 2D spintronic devices that show various emergent spin-orbit coupled phenomena with time reversal and inversion symmetry breaking.^[97] In spite of a strong desire to develop such 2D spintronic devices, low critical temperatures (T_c) of these suggested vdW ferromagnets have been an obstacle in applications.^[92,93,96] Therefore, achieving a T_c above room temperature in the vdW ferromagnet is a critical issue for the development of novel spintronic devices.

As a promising vdW ferromagnet, the Fe_nGeTe_2 family ($n = 3, 4, 5$) was recently proposed based on its high T_c (260 ~ 310 K) and large saturation magnetization.^[98–105] In particular, Fe_5GeTe_2 with a rhombohedral space group ($R\bar{3}m$) is expected to show the highest T_c among Fe_nGeTe_2 family because the additional Fe layer in Fe_5GeTe_2 can boost

magnetic interaction.^[101,102] Also, the additional Fe layer gives rise to three magnetic transitions depending on temperature (around 70, 180, and 270 K) for in-plane (*ab*-plane) magnetization, which have not been reported in Fe₃GeTe₂ and Fe₄GeTe₂ crystals.^[98,101–103] Recently, these unconventional magnetic properties have been explained with magnetic anisotropy or/and spin reorientation by the Fe atoms in Fe₅GeTe₂.^[100,102,103] However, the exact mechanism of such non-trivial magnetic behaviors is still unclear because it is also involved with the structural complexity in Fe₅GeTe₂. For instance, May *et al.* reported that Fe₅GeTe₂ has ordering driven by Fe and Ge positions,^[100] while the ordering of Fe and Ge pair was not considered in other works.^[103,106] It is very important to clarify these structural details because they may have significant effects on the magnetic ordering in Fe₅GeTe₂. Therefore, systematic study for finding the correlation between such non-trivial magnetic behaviors and the atomistic structure of Fe₅GeTe₂ is needed to realize room temperature spintronic devices with this new vdW ferromagnet.

In this report, we explore atomistic structures of an Fe_{5-x}GeTe₂ single crystal by low temperature scanning tunneling microscopy (STM) and its temperature dependent magnetic behaviors. Subset Fe layers in Fe₅GeTe₂ are expected to play a major role in magnetic ordering. Among these Fe layers, Fe(1) located in the outermost Fe₅Ge sublayer can occupy one of two possible split-sites, situated either above or below the Ge atom. STM topography reveals $\sqrt{3}\times\sqrt{3}$ superstructures on the cleavage surface of Fe_{5-x}GeTe₂, which are attributed to the ordering of Fe(1) layer. The symmetry of Fe(1) ordering also allows two phases of $\sqrt{3}\times\sqrt{3}$ superstructures. Intriguingly, observed $\sqrt{3}\times\sqrt{3}$ ordering of Fe(1) - Ge pair breaks the inversion symmetry, which is an important microscopic origin of the antisymmetric exchange interaction, known as Dzyaloshinskii-Moriya interaction (DMI). The temperature dependent magnetization of Fe_{5-x}GeTe₂ clearly shows commensurate-incommensurate

transition, a typical helimagnetic behavior arising from the DMI, just below $T_c = 310$ K. We also confirm that spin reorientation behaviors are observed within the ranges of $120 \sim 260$ K and $20 \sim 100$ K due to competition between helimagnetism and other collinear properties. Our findings suggest that the Fe_5GeTe_2 crystal has helical magnetism with non-centrosymmetric ordering of Fe(1) - Ge pairs, which can be a source of topologically protected spin solitons to develop new types of topology-based spin devices.^[107-110]

4.1 Surface treatment

$\text{Fe}_{5-x}\text{GeTe}_2$ single crystals were cleaved *in-situ* by conducting epoxy as shown in Fig. 4.1. The aluminum rod is stuck on the sample surface by conducting epoxy before transfer inside the UHV chamber. Then, under UHV condition (pressure of 2×10^{-10} Torr), using the wobble stick to hit the rod along red arrow direction. By this way, the contaminated layers are removed from the surface obtaining clean surface. This method can be applied for some vdW materials besides using Kapton tape for cleaving.

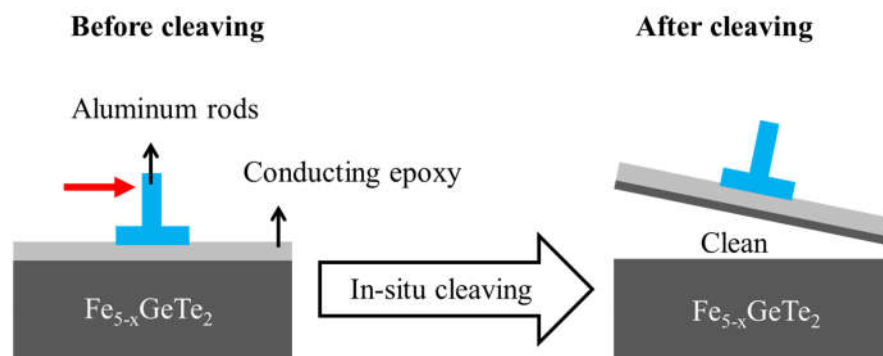


Figure 4.1: $\text{Fe}_{5-x}\text{GeTe}_2$ surface is cleaved by conducting epoxy to remove contaminations.

4.2 Analysis surface structure of $\text{Fe}_{5-x}\text{GeTe}_2$

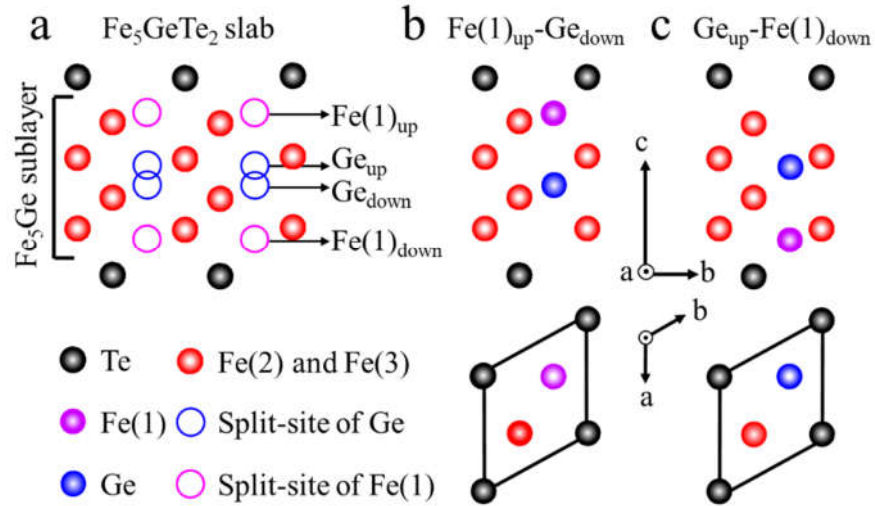


Figure 4.2: Structure model of Fe_5GeTe_2 . a) Crystal structure of Fe_5GeTe_2 (space group $\bar{R}3m$). Two possible Fe(1) – Ge split-sites of b) $\text{Fe(1)}_{\text{up}}\text{-Ge}_{\text{down}}$ and c) $\text{Ge}_{\text{up}}\text{-Fe(1)}_{\text{down}}$. Vectors a, b, and c are along [100], [010], and [001] directions. The black, pink, blue, and red balls represent Te, Fe(1), Ge, and Fe(2)-(3) atoms, respectively; open circles indicate possible occupancy sites of Fe(1) and Ge.

Fe_5GeTe_2 belongs to the Fe_nGeTe_2 family ($n = 3, 4, 5$) where each layer consists of a Fe_nGe slab sandwiched by Te layers. The sublayer of Fe_nGe plays an essential role in the magnetic properties of the Fe_nGeTe_2 system.^[102] There is one important structural characteristic of Fe_5GeTe_2 which makes it very different from other Fe_nGeTe_2 systems. In Fe_5GeTe_2 , Fe(1) positioned in the outermost Fe_5Ge sublayer and Ge has two possible split-sites, raising structural complexity. The X-ray diffraction experiment indicates that Fe(1) - Ge split-site pairs can form ordering,^[100] while such ordering was not considered in other recent works.^[103,106] Further atomistic microscopy study is still necessary to confirm these structural details of Fe_5GeTe_2 . Fig 4.2a shows the possible split-sites of Fe(1) (Fe(1)_{up} ,

Fe(1)_{down}) and Ge (Ge_{up}, Ge_{down}) marked by pink and blue open circles, respectively. Two possibilities of Fe(1) and Ge occupancies are presented in Fig. 4.2b as Fe(1)_{up} – Ge_{down} and Fig. 4.2c as Ge_{up} – Fe(1)_{down}; i.e. the split-site of Ge is determined by Fe(1) position because the Fe(1) atom pushes the Ge atom further away.^[100] Our density functional theory (DFT) calculation also indicates that having Fe(1) both above and below Ge is not allowed due to the required bonding length between them.

4.2.1 Overview of $\text{Fe}_{5-x}\text{GeTe}_2$ surface morphology

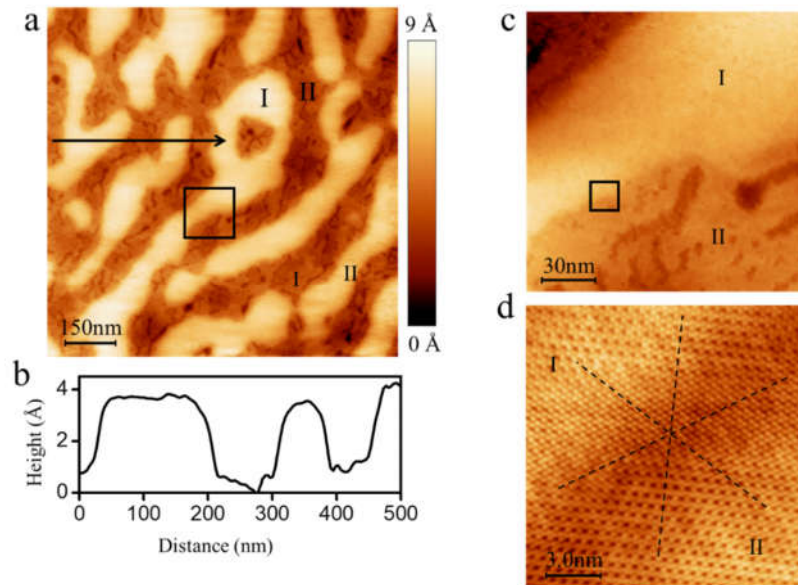


Figure 4.3: Surface morphology of Fe_5GeTe_2 . a) STM topographic image obtained from the cleavage surface of $\text{Fe}_{5-x}\text{GeTe}_2$ shows two different regions, marked by I and II ($V_b = 100$ mV, $I_t = 50$ pA at 79 K). b) Line profile taken along the arrow in (a). c) Zoomed-in STM image taken from the black box in (a). d) Zoomed-in STM image taken from the black box in (c). The dashed lines indicate the crystal axes. e) The fast Fourier transformation (FFT) image of (d). All STM images were taken at the same conditions of $V_b = 10$ mV, $I_t = 50$ pA.

The clean surface of $\text{Fe}_{5-x}\text{GeTe}_2$ single crystal is prepared by *in-situ* cleavage in UHV STM chamber. STM topography in Fig 4.3a shows stripe-like structures consisting of two areas marked by I and II. In Fig. 4.3b, the line profile taken along the arrow in Fig.4.3a shows that the height difference between the region I and II is around 4 Å. Fig.4.3d taken from the box in Fig.4.3c, which is zoomed in image from the box in Fig 4.3a, shows that all crystal axes of the region I and II are perfectly aligned as marked by dashed lines.

4.2.2 Origin of $\sqrt{3}\times\sqrt{3}$ superstructure in $\text{Fe}_{5-x}\text{GeTe}_2$ surface

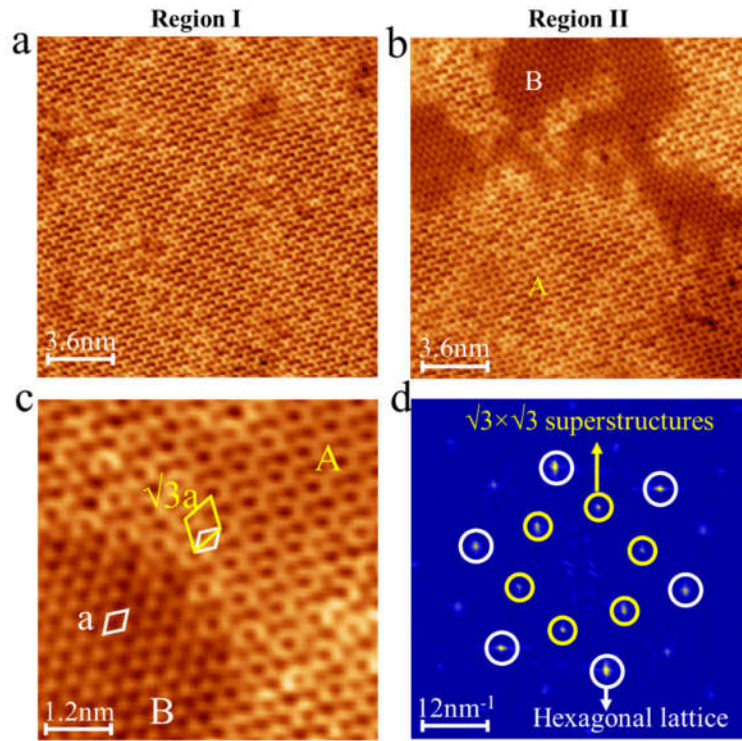


Figure 4.4: Detailed atomic structures of $\text{Fe}_{5-x}\text{GeTe}_2$ surfaces. a-b) STM images are taken from region I and II in Fig. 4.3a, respectively. STM image obtained from region II in (b) shows two different areas, marked by A and B. c) The higher resolution STM image showing both A and B areas. (d) The fast Fourier transformation (FFT) images of (a-c) showing both hexagonal lattice and $\sqrt{3}\times\sqrt{3}$ superstructures marked as white and yellow circles, respectively.

Atomistic images taken from regions I and II are provided in Fig. 4.4a-b, respectively. The ab -plane view in Fig. 4.2b-c shows that the topmost Te layer (black balls) has triangular lattice structure. In region I of Fig. 4.3a, interestingly, we observe additional superstructures on the hexagonal lattice of top Te layer (Fig. 4.4a). As shown in Fig. 4.4d, the fast Fourier transformation (FFT) image of Fig. 4.4a-c presents that $\sqrt{3}\times\sqrt{3}$ superstructure

(yellow circles) exists with respect to the hexagonal lattice (white circles). Detailed analysis of the $\sqrt{3}\times\sqrt{3}$ superstructure is given in Fig. 4.5.

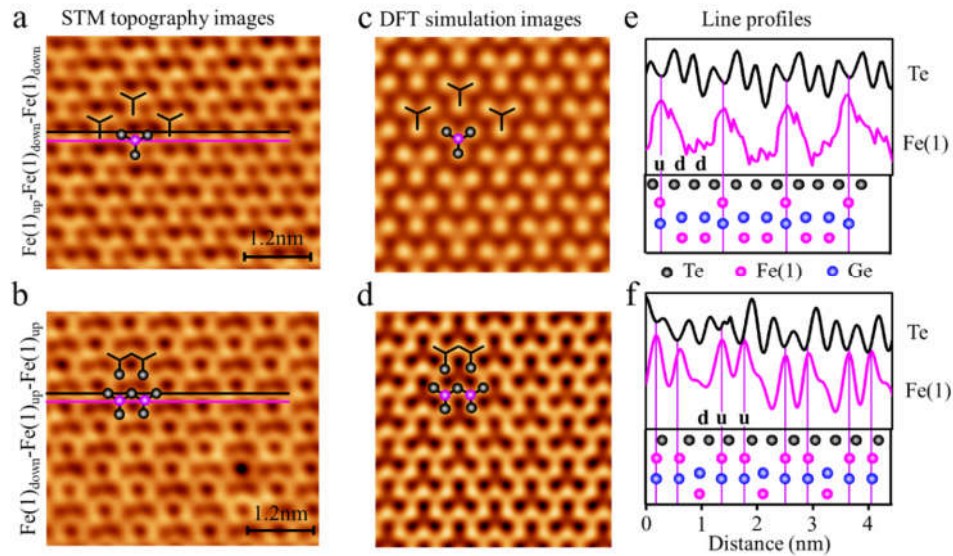


Figure 4.5: Comparison between STM and DFT simulation images of $\sqrt{3}\times\sqrt{3}$ superstructures. a) and b) STM images of $\sqrt{3}\times\sqrt{3}$ superstructures with “udd” and “duu” orderings of Fe(1) layers, respectively. The Y-shaped feature connects three Te atoms to one Fe(1)_{up} atom at the center. c) and d) DFT simulation STM images of “udd” and “duu” orderings. e) and f) show the line profiles crossing Te (black) and Fe(1) (pink) lattices taken along the solid lines in (a) and (b), respectively. The suggested models are provided below the line profiles and the Fe(2)-(3) atoms are not illustrated for simplicity. The scanning conditions of (a-b) are $V_b = 10$ mV, $I_t = 50$ pA.

Interestingly, we find two different phases of the $\sqrt{3}\times\sqrt{3}$ superstructures that are directly correlated with two symmetric orderings of Fe(1) layers such as Fe(1)_{up} - Fe(1)_{down} - Fe(1)_{down} (udd) and Fe(1)_{down} - Fe(1)_{up} - Fe(1)_{up} (duu). Both Figs 4.5a and 4.5b exhibit $\sqrt{3}\times\sqrt{3}$ superstructures with “udd” and “duu” orderings of Fe(1) layers, respectively. Since

$\text{Fe}(1)_{\text{up}}$ locates at the hollow site of Te hexagonal lattices (the ab -plane view of Fig. 4.2b,c), such orderings of $\text{Fe}(1)_{\text{up}}$ layers are directly confirmed from STM topography. Two profiles in Fig. 4.5e,f are taken from the Te lattice (black) and $\text{Fe}(1)$ lattice (pink) lines in Fig. 4.5a,b. Then, the pink lines evidently indicate “udd” (Fig. 4.5e) and “duu” (Fig. 4.5f) orderings of $\text{Fe}(1)$ layers. Accordingly, Ge layers are expected to order as well, shown in the bottom model of Fig. 4.5e,f. In addition, $\text{Fe}(1)$ orderings result in a Y-shaped feature which connects three Te atoms to one $\text{Fe}(1)_{\text{up}}$ atom at the center as marked in both topographs of Fig. 4.5a,b. These Y-shaped features eventually give rise to the $\sqrt{3}\times\sqrt{3}$ ordering in Fig. 4.5a,b. The Y-shaped feature and its periodic array are very well resolved in our DFT simulation images of Fig. 4.5c,d, supporting that our structural analysis is correct.

Fig. 4.6a and 4.6b show the line profiles along the arrows in Fig. 4.6c (“udd”) and 4.6d (“duu”), respectively. We find that the Te lattices are distorted due to the orderings of underneath $\text{Fe}(1)$ atoms. For the “udd” order (Fig. 4.6a), the Te-Te atomic spacing increases up to $\sim 4.3 \text{ \AA}$ (d_1) with $\text{Fe}(1)_{\text{up}}$, compared to $\sim 3.6 \text{ \AA}$ (d_2) with $\text{Fe}(1)_{\text{down}}$. Similar behavior of lattice distortions is also observed for the “duu” order as shown in Fig. 4.6b.

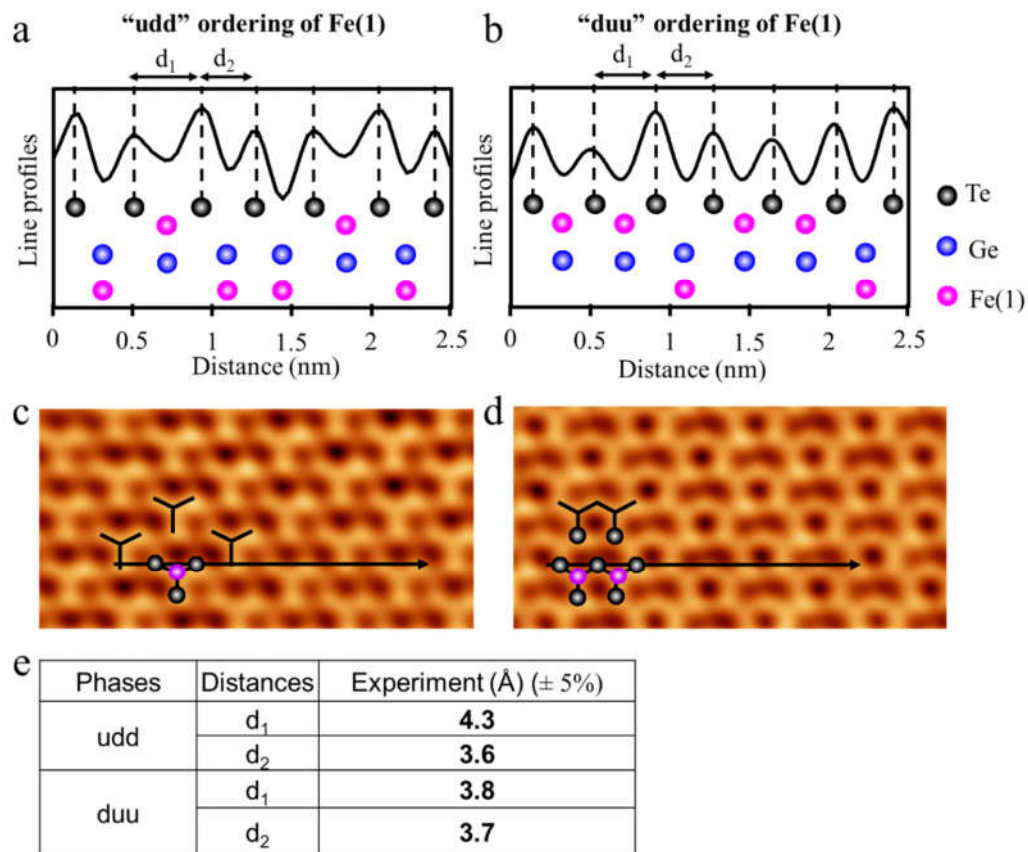


Figure 4.6: Lattice distortion of the top Te layer. a-b) Line profiles crossing Te atoms along the black arrows in (c) and (d). d_1 and d_2 indicate Te-Te atomic spacing with Fe(1)_{up} and Fe(1)_{down}, respectively. c-d) STM topography images showing “udd” and “duu” ordering of Fe(1). e) Table of d_1 and d_2 values. All STM images were taken at the same conditions of $V_b = 10$ mV, $I_t = 50$ pA.

4.2.3 B area-Fe deficiency area

Fig. 4.7a is a magnified topograph taken from the B area in region II of Fig. 4.4b showing simple hexagonal structure which is attributed to Fe(1)-deficiency commonly existing in Fe₅GeTe₂ single crystal. In fact, FFT image in Fig. 4.7c clearly shows an undistorted hexagonal structure of the top Te layer. In order to confirm this, DFT simulation

(Fig. 4.7b) is conducted for Fe_4GeTe_2 considering the absence of Fe(1) layer in Fe_5GeTe_2 , which indeed shows very good agreement with STM experiment (Fig. 4.7a).

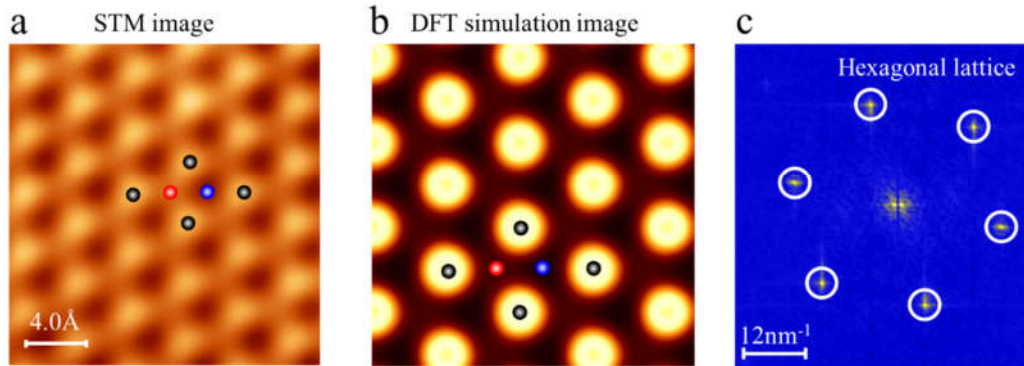


Figure 4.7: Comparison between STM and DFT simulation images. a) STM topography image of Fe-deficient area in Fe_5GeTe_2 ($V_b = 10 \text{ mV}$ and $I_t = 50 \text{ pA}$). b) DFT simulation image of Fe_4GeTe_2 . (c) FFT image of (a).

It is known that Fe-deficiency commonly exists in the Fe_nGeTe_2 system.^[99,101,111,112] We confirm that Fe-deficiency exists in our single crystal sample, and its composition is estimated to be $\text{Fe}_{4.8}\text{GeTe}_2$. Then, the B area in Fig. 4.7a having an undistorted hexagonal lattice of Te is attributed to local Fe(1) vacancies whose ordering is responsible for $\sqrt{3} \times \sqrt{3}$ superstructures. Our DFT simulation of the STM image on Fe_4GeTe_2 structure (Fig. 4.7b) also agrees with STM observation in Fig. 4.7a. Previous STM studies reported simple hexagonal structure without any superstructures in Fe_4GeTe_2 .^[102,111] Two phases of $\sqrt{3} \times \sqrt{3}$ Fe(1) orderings are observed in both region I and II, while the Fe(1)-deficient area is found mostly in region II in Fig. 4.3a.

It should be noted that the $\sqrt{3} \times \sqrt{3}$ ordering observed in STM image breaks the inversion symmetry in the $\text{Fe}_{5-x}\text{GeTe}_2$ crystal. This non-centrosymmetric structure is

essential for the chiral magnetic property of a matter because it induces the asymmetry in the electronic structures, resulting in Dzyaloshinskii-Moriya interaction.^[113–115] Detailed investigations on the magnetic property of $\text{Fe}_{5-x}\text{GeTe}_2$ are discussed in the following section.

4.3 Magnetic properties of $\text{Fe}_{5-x}\text{GeTe}_2$

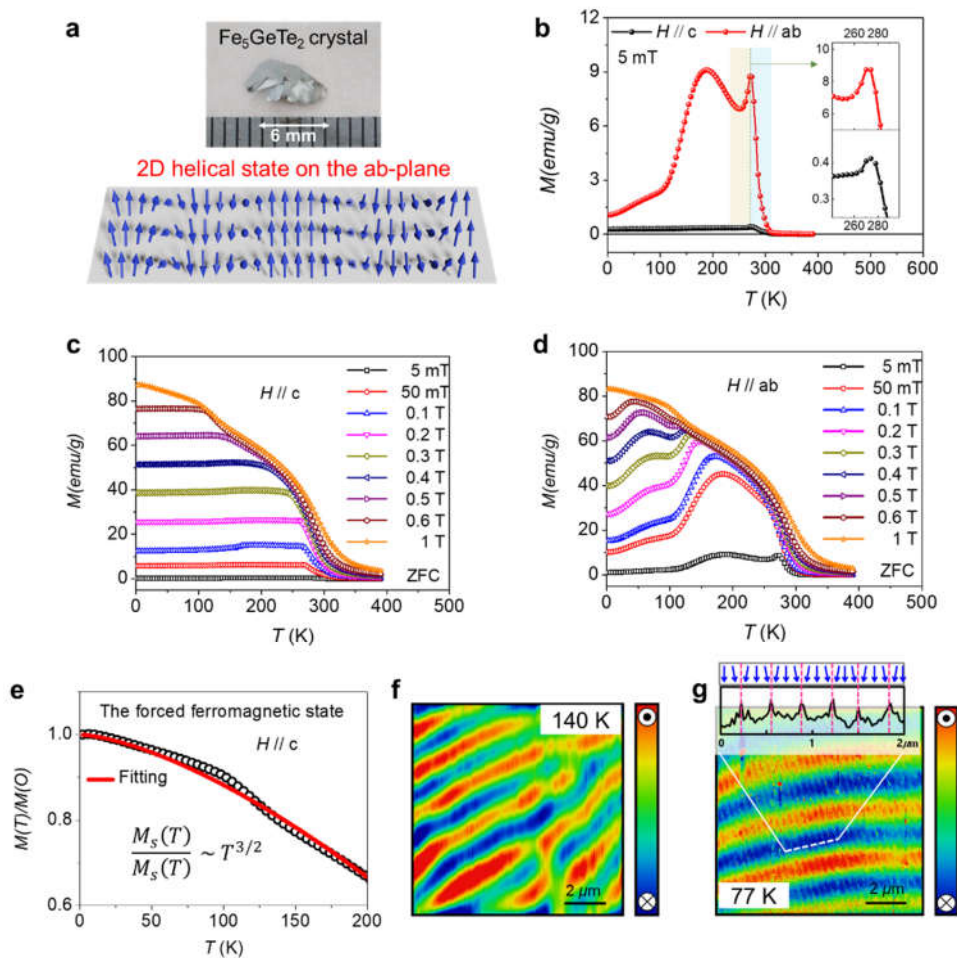


Figure 4.8. The magnetic properties of $\text{Fe}_{5-x}\text{GeTe}_2$. a) $\text{Fe}_{5-x}\text{GeTe}_2$ crystal (upper) and 2D helical ordering (lower) based on chiral soliton lattice phase of $\text{Fe}_{5-x}\text{GeTe}_2$ with crystallographic direction marked. The arrows represent the total magnetization (including both Fe and Ge magnetic moments), which exhibits a helical ordering along the b -axis. The three layers of the arrows show the magnetization profile along the a -axis. b) Temperature dependence of magnetization measured for in-plane (red, $H//ab$ -plane) and out of plane (black, $H//c$ -axis) field with 5 mT. The commensurate (blue-shaded area)-to-incommensurate (yellow-shaded area) transition appears around 273 K. The inset shows the magnetic anomaly of $H//ab$ -plane (upper) and $H//c$ -axis (bottom). c) and d) Comparison of temperature-dependent magnetization in various applied magnetic fields for (c) $H//ab$ -plane and (d) $H//c$ -axis, respectively. The forced ferromagnetic state was observed in both cases of $H//ab$ -plane and $H//c$ -axis under 1 T (saturation field). e) Temperature dependence of magnetization with the forced ferromagnetic state fitted by Bloch 3/2 law. The red solid line is the fitted curve. The MFM images of $\text{Fe}_{5-x}\text{GeTe}_2$ in f) 140 K and g) 77 K. The stripe domain wall was observed. The red and blue indicate spin-up and down states of domain, respectively. The inset of (g) is the line profile taken along the white dotted line, which exhibits the fan-like fine structures in the magnetic domains (also schematically illustrated in the inset).

Here, we perform the magnetic measurement in terms of T and H to investigate the effect of the $\sqrt{3}\times\sqrt{3}$ Fe(1) - Ge ordering on magnetic properties of $\text{Fe}_{5-x}\text{GeTe}_2$ crystal. The magnetic field of $H = 5$ mT is applied with in-plane ($H//ab$ -plane) and out-of-plane ($H//c$ -axis) orientations for the measurement of temperature-dependent magnetization (M - T) upon heating after zero field cooling (ZFC) from 390 K down to 2 K. We note two important observations; our $\text{Fe}_{5-x}\text{GeTe}_2$ sample has $T_c \approx 310$ K which is higher than that of Fe_4GeTe_2 (≈ 270 K) due to the enhancement of ferromagnetic spin-pair interaction as reported in Ref.^[102]. Additionally, a sharp peak, hereafter referred to as the *magnetic anomaly*, is

observed around 273 K in both cases of $H//ab$ (red) and $H//c$ (black) as shown in the inset of Fig. 4.8b. Although a similar anomaly was reported in $\text{Fe}_{5-x}\text{GeTe}_2$, its origin still remains unknown.^[103] We propose that the anomaly indicates the onset of helimagnetism accompanying the helical alignment of spins as suggested in Ref.^[116] (see also Fig. 4.8a). In the two phases of $\sqrt{3}\times\sqrt{3}$ Fe(1) - Ge orderings (referred to as the “udd” and “duu” phases), the inversion symmetry is broken within each layer. Therefore, from the symmetry grounds, the two-dimensional Dzyaloshinskii-Moriya interaction (DMI) in the Hamiltonian must exist. We find the ratio between DMI and exchange energy of the $\text{Fe}_{5-x}\text{GeTe}_2$ crystal at 140 K is about 0.1, implying the large contribution of DMI to the total energy in the system (see Appendix B2-B4). In general, a helimagnet ground state is known to arise from competition between this DMI and ferromagnetic exchange in the non-centrosymmetric system.^[116-118]

The aforementioned magnetic anomaly can be understood by considering the symmetry-inferred existence of the DMI as follows. For temperatures just below the Curie temperature, the magnetization is small and thus the Zeeman coupling (linear in the magnetization) dominates the exchange interaction and the DMI (quadratic in the magnetization). In this case, the system is in a uniform phase (also called the commensurate phase), where the magnetization is uniform in the direction of the applied field. As the temperature decreases, the magnetization increases, and this can be seen in Fig. 4.8b for temperatures between 273 K and 310 K. When we decrease the temperature further, eventually the exchange interaction and the DMI take over the Zeeman coupling. In this case, the system enters a chiral soliton lattice phase (also called the incommensurate phase), where the magnetization changes periodically along one direction with pitch determined by the competition among the exchange energy, the DMI, and the Zeeman coupling. In this chiral soliton lattice phase, the magnetization changes spatially and thus the average magnetization in one specific direction

is smaller than the saturation magnetization. This leads to a sudden drop of the average magnetization as shown in Fig. 4.8b around 273 K. This transition between the uniform phase and the chiral soliton lattice phase is called commensurate-to-incommensurate (C-IC) transition.^[116,119] The phase boundary between the uniform phase and the chiral soliton lattice phase has also been studied in the context of two-dimensional chiral magnets with the DMI in Refs.^[120–122] Analytical study regarding the C-IC transition and the magnetization profile on the chiral soliton lattice phase is provided in Appendix B1. This C-IC leads to the magnetic anomaly just below T_c , indicating formation of magnetic soliton lattice.^[116] A similar magnetic anomaly has been experimentally observed in helical magnetic systems, *i.e.*, $T_{1/3}\text{NbS}_2$ ($T = \text{Cr}$ and Mn)^[117,123,124] and CuB_2O_4 ^[119]. Therefore, we attribute the observed anomalous peak at 273 K to the helimagnetic behavior of the magnet induced by the structural inversion asymmetry of the $\text{Fe}(1) - \text{Ge} \sqrt{3} \times \sqrt{3}$ ordering. This striking chiral behavior has not been observed in other vdW magnets yet. Therefore, the Fe_5GeTe_2 is indeed promising to realize the skyrmion-based memory devices and future nano-inductors.^[107–110]

In the range 110 ~ 260 K, a broad cusp is observed in the case of $H//ab$. It was reported that Fe_4GeTe_2 shows a similar cusp explained by simple anisotropy changes.^[100,102] However, it is rather complicated for the Fe_5GeTe_2 because of the helical character. Spin reorientation should occur *via* competition between DMI and other energy terms such as Heisenberg exchange interaction, magneto-crystalline anisotropy, and magnetostatic energy.^[125–127] It is natural to see the transition from the helimagnetic spin alignment to the commensurate state due to the competitions. Since all those energies are T dependent, quantitative study for each energy parameter is required to manifest exact origin of the large-range cusp. In spite of such complexity of magnetism in the $\text{Fe}_{5-x}\text{GeTe}_2$ crystal, it is clear that an easy axis of magnetization is on the c -axis within the temperature range, which will

be further discussed in the magnetic force microscopy (MFM) results (Fig. 4.8f,g). Small magnetization with the c -axis is due to the formation of stripe domain structures. Details are discussed in the following paragraphs.

Fig. 4.8c-d exhibit the M - T curves at various magnetic fields under $H//ab$ and $H//c$, respectively. The observed magnetic anomaly in Fig. 4.8b disappears with an increase in applied magnetic field in Fig. 4.8c. This indicates a IC-C transition that helimagnetic state turns into other spin ordering as mentioned above.^[124] For $H//ab$ (Fig. 4.8d), the other cusp appeared for 0.2 T in the range 30 ~ 100 K, implying another magnetic phase transition in terms of T and H . Relatively large external magnetic field of ~ 0.3 T is required to observe the transition below 100 K. The forced ferromagnetic (FFM) states, which means the full saturated state, are formed under high magnetic field (> 1 T) in both cases of $H//ab$ and $H//c$. Here, the saturation magnetic moments of $H//ab$ and $H//c$ are about $9.0\mu_B/\text{Fe}_{5-x}\text{GeTe}_2$ and $9.4\mu_B/\text{Fe}_{5-x}\text{GeTe}_2$ at 10 K, respectively. In addition, the exchange stiffness energy (A_{stiff}) is 1.856 pJ/m at 0 K, estimated from the fitted M - T curve with the FFM state using the Bloch $T^{3/2}$ law (Appendix B2).

As shown in the magnetic force microscopy images (Fig. 4.8f,g), $\text{Fe}_{5-x}\text{GeTe}_2$ crystal has stripe domain structure at 140 K and 77 K, confirming that the crystal has a magnetic easy axis within the c -axis. This explains why the trend of the M - T curves for $H//c$ is different from those of $H//ab$ with a small external field; the $M//c$ becomes saturated below certain temperatures, while $M//ab$ shows *anomaly* and cusps. The wide range plateau for the $H//c$ case is due to that the total magnetization within the c -axis does not change, forming such stripe domain structures. In particular, fan-like fine structures in the magnetic domains are seen at $T = 77$ K (see the inset of Fig. 4.8g), which is below the temperature for phase

transition (~ 120 K).^[100] Such fine structures can result from strong DMI giving rise to chirality in magnetic properties of the $\text{Fe}_{5-x}\text{GeTe}_2$ crystal. From domain size in the MFM image scanned at 140 K, the estimated DMI energy density (D) is ~ 0.36 mJ/m². This value is comparable to the known DMI values of other materials. The DMI of various ferromagnetic systems has been reported to be an order of 0.1-3 mJ/m².^[125,128-132] Thus, the ratio of DMI and exchange energies when $T = 140$ K is ~ 0.1 , which is an important parameter to form such helical ordering as discussed in the Appendix B1 and B4. This ratio implies that DMI contribution to the total energy in the $\text{Fe}_{5-x}\text{GeTe}_2$ crystal is large enough to have such helical magnetic structure as confirmed with our analytical study. The details regarding the analytical model explaining the magnetic anomaly and the related energy parameters are given in Appendix B2-B4. Though further study is still required to understand the helimagnetic behavior in terms of T and H , our observations demonstrate the presence of helimagnetism in the $\text{Fe}_{5-x}\text{GeTe}_2$ crystal with the $\sqrt{3}\times\sqrt{3}$ ordering.

4.4 Conclusion

Although $\text{Fe}_{5-x}\text{GeTe}_2$ is considered a promising vdW ferromagnet due to its room temperature ferromagnetism, the microscopic structure and magnetic property of $\text{Fe}_{5-x}\text{GeTe}_2$ are not fully revealed due to the structural complexity. The $\sqrt{3}\times\sqrt{3}$ superstructure observed at the cleavage surface of $\text{Fe}_{5-x}\text{GeTe}_2$ is attributed to the ordering of underlying Fe(1) atoms. We find that two symmetric orderings of Fe(1) coexist in the $\text{Fe}_{5-x}\text{GeTe}_2$ system, and both orderings give rise to the $\sqrt{3}\times\sqrt{3}$ superstructure. Two symmetric Fe(1) orderings are directly identified by resolving $\text{Fe}(1)_{\text{up}}$ atoms in STM topography. The non-centrosymmetry originated from $\sqrt{3}\times\sqrt{3}$ orderings of the Fe(1) - Ge pair could cause helical magnetic ordering in $\text{Fe}_{5-x}\text{GeTe}_2$ due to competition between the antisymmetric exchange interaction and Heisenberg interaction. These results will provide an important role of Fe(1) orderings for understanding chiral or helical ordering in the $\text{Fe}_{5-x}\text{GeTe}_2$ crystal, which are promising characteristics to develop topology-based spin devices.

Chapter 5

Monolayer transition-metal dichalcogenides: VSe_2 , $ReSe_2$

The transition-metal dichalcogenides (TX_2) layer materials form a structurally and chemically well-defined family. Electrically, however, they cover a wide spectrum of properties, such as, insulator (HfS_2), semiconductors (MoS_2 , $ReSe_2$), semi-metals (WTe_2 , TeS_2), and metals (NbS_2 , VSe_2). Several of the materials such as $TaTe_2$, WTe_2 and $ReSe_2$ show structural distortions that throw their properties out of line as compared with their undistorted analogues.^[133]

Gaining an understanding of electronic reconstruction due to dimensionality and heterointerface coupling in layered van der Waals systems remains an open issue. Although the influence of the interface is often considered to be negligible for the transition metal dichalcogenides (TMDs) due to the weakness of the weak van der Waals interactions, the substrate may play an important role due to strain.^[134,135] To understand the effect of substrate to TMDs sample surface, the surface structure and electronic properties of TMD sample surface need to be clarified at atomistic level.

In this chapter, we will discuss about surface structure of ML VSe_2 on BLG and interface effect of graphene- $ReSe_2$ in ML $ReSe_2$ on BLG.

5.1 Monolayer VSe₂ on BLG: Lattice Distortion driving Charge Density

Wave of $\sqrt{3} \times 2$ and $\sqrt{3} \times \sqrt{7}$

A charge density wave (CDW) consists of static spatial modulations of electron distribution and lattice distortion observed in various metallic systems, including superconductors.^[136–140] Unique Fermi surface structure in which a single reciprocal lattice vector connects two large segments of the Fermi surfaces (Fermi surface nesting) is considered as one of the main origins for the CDW formation.^[141,142] CDW phenomena often accompany periodic lattice distortions called Peierls instabilities.^[142–144] There are also other origins of CDW such as Fermi patch,^[145] van Hove singularity,^[146] and periodic lattice distortion.^[147] In order to understand the fundamental properties of CDW phases, it is important to clarify whether CDW modulations are predominantly attributed to charge orderings or lattice distortions. For this purpose, scanning tunneling microscopy/spectroscopy (STM/S) is an ideal tool because it is sensitive to both charge distributions and lattice structures with atomic resolution. Although STM topographic images contain mixed information regarding spatial charge distributions and lattice structures, one can separate those two signals via differential conductance (dI/dV) spatial mapping, which represents only charge information.

When their thickness is reduced to the two-dimensional limit, TMDs exhibit intriguing properties which are very different from those of the bulk.^[148–154] For instance, vanadium diselenide (VSe₂) has been studied due to the emergence of room temperature ferromagnetism^[155–160] and new CDW phase at monolayer (ML) thickness.^[161,162] It is well known that bulk VSe₂ is a good example of three-dimensional CDW with $4 \times 4 \times 3$ periodicity driven by Fermi surface nesting.^[163–166] Considering quasi two-dimensional

characteristics of TMD materials, one might speculate that ML VSe₂ would show 4×4 CDW, which is simply projected 3D CDW of $4 \times 4 \times 3$ into a 2D plane.^[141] Surprisingly, recent STM studies reported that a new CDW phase with completely different periodicities of $\sqrt{3} \times 2$ and $\sqrt{3} \times \sqrt{7}$ emerges in ML VSe₂ grown on graphene substrates.^[161,167] The role of dimensionality on the emergence of new CDW phase is of great research interest in VSe₂ system. However, so far, no theoretical calculations have been successfully demonstrated the existence of $\sqrt{3} \times 2$ and $\sqrt{3} \times \sqrt{7}$ CDW phase observed in STM studies, and also the origin of this new CDW has not been clearly investigated.

Here, we provide a systematic investigation on the new CDW phase of $\sqrt{3} \times 2$ and $\sqrt{3} \times \sqrt{7}$ in ML VSe₂ using low temperature STM/S. STM topography shows that the new CDW phase in ML VSe₂ has a strong stripe modulation with $\sqrt{3} \times 2$ and $\sqrt{3} \times \sqrt{7}$ periodicities.^[161] Interestingly, the stripe modulation is significantly suppressed in simultaneously taken dI/dV mapping images. We directly compared the signal intensities of the stripe modulations for topographic and dI/dV mapping images taken at various bias voltages. Indeed, the $\sqrt{3} \times 2$ and $\sqrt{3} \times \sqrt{7}$ modulations are significantly weakened in the dI/dV mapping images at all bias ranges, indicating that charge ordering is not the driving factor of the observed modulations. In addition, detailed topographic analysis confirms the direct match between the modulations and the lattice distortions of Se atoms: i.e. the $\sqrt{3} \times 2$ and the $\sqrt{3} \times \sqrt{7}$ periodicities correspond to a gap feature and an isolated Se atom of the distorted lattice structures, respectively. Our work provides important information regarding the nature of the $\sqrt{3} \times 2$ and $\sqrt{3} \times \sqrt{7}$ CDW in ML VSe₂.

5.1.1 Sample preparation

ML VSe₂ samples were prepared on epitaxial bilayer graphene on SiC substrates using a molecular beam epitaxy (MBE) system under a base pressure of 2×10^{-10} Torr. A Se capping layer of 100nm was then deposited at room temperature to protect the sample from degradation during transfer to the STM chamber. The capping layer was removed by several circles of Ar⁺ sputtering and then annealing at 300 °C for several hours. The sample cleaning process is showing in Fig. 5.1

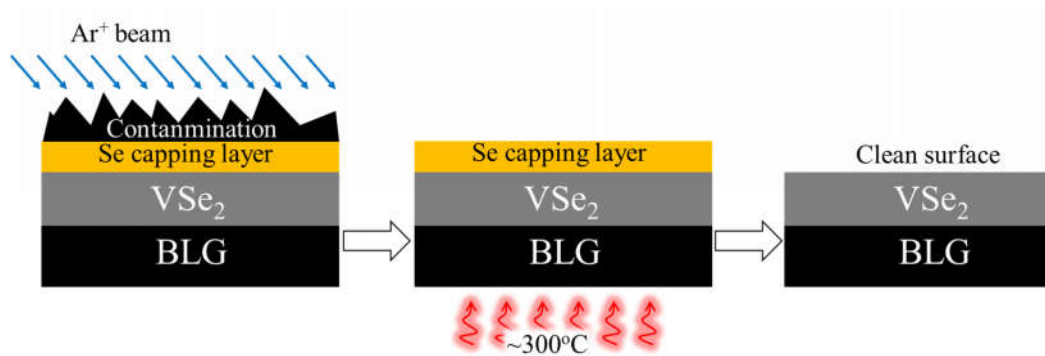


Figure 5.1: Sample cleaning process for VSe₂ on BLG

5.1.2 Results and Discussion

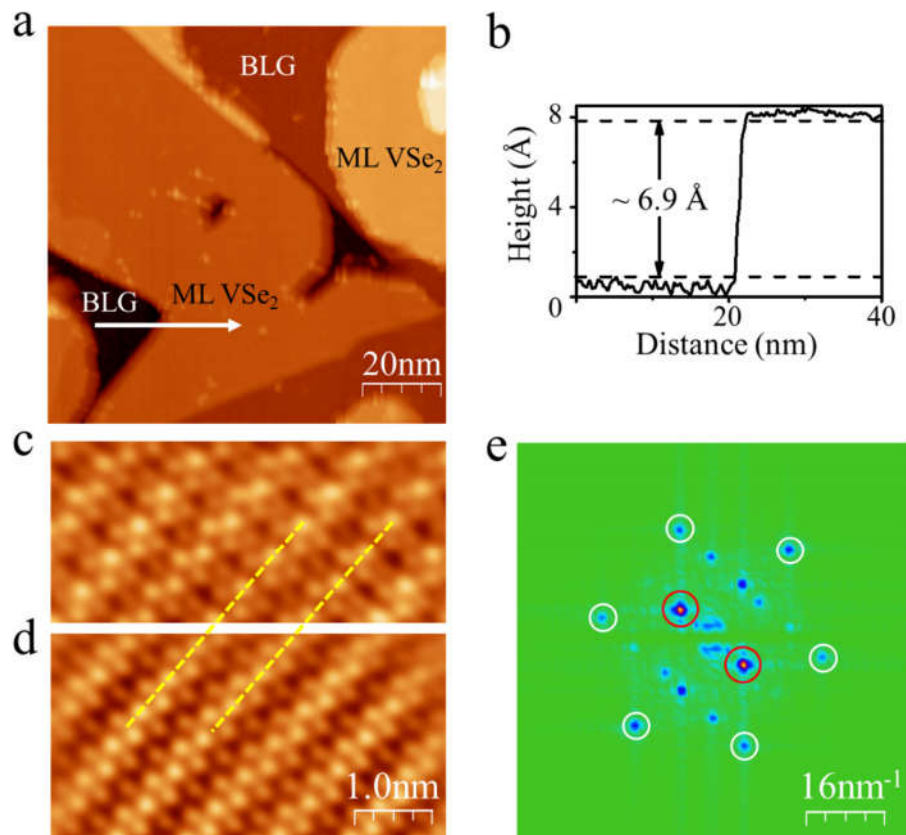


Figure 5.2: STM images of ML VSe₂ on BLG. (a) STM image of the morphology of ML VSe₂ grown on bilayer graphene (BLG) ($V_b = 3$ V, $I_t = 30$ pA). (b) Line profile taken along the arrow in (a). (c) High resolution STM image showing strong stripe modulation ($\sqrt{3} \times 2$ and $\sqrt{3} \times \sqrt{7}$ CDW) marked by dashed lines ($V_b = -1.6$ V, $I_t = 50$ pA). (d) Fourier-filtered image generated by selectively taking the stripe modulation peaks (red circles) and VSe₂ lattice peaks (white circles) in (e). (e) Fast Fourier transformation (FFT) image of (c).

ML VSe₂ films were grown on top of epitaxial bilayer graphene (BLG) on 6H-SiC(0001) substrate by using MBE method. All STM/S measurements were carried out at

79 K under the base pressure of $\sim 7 \times 10^{-11}$ Torr. Fig. 5.2a shows that the surfaces are mostly covered by ML thickness of VSe₂ film. The height of ML VSe₂ is measured to be around 6.9 Å in Fig. 5.2b. As shown in Fig. 5.2c, ML VSe₂ exhibits strong modulation along the diagonal direction (marked by dashed line) which is the $\sqrt{3} \times 2$ and $\sqrt{3} \times \sqrt{7}$ CDW reported previously.^[161] Detailed analysis regarding $\sqrt{3} \times 2$ and $\sqrt{3} \times \sqrt{7}$ periodicities will be discussed later. The fast Fourier transformation (FFT) image of Fig. 5.2c presents hexagonal lattice peaks (white circles) and superstructure peaks inside the hexagon of white circles in Fig. 5.2e. Fig. 5.2d presents Fourier-filtered image obtained by selectively taking the white and red circle peaks in Fig. 5.2e. Since Fig. 5.2d precisely preserves the diagonal modulation (dashed lines in Fig. 5.2c-d), those two strongest peaks (red circles in Fig. 5.2e) directly correspond to the CDW modulation in Fig. 5.2c. Therefore, the modulation peaks provide essential information for understanding the nature of the $\sqrt{3} \times 2$ and $\sqrt{3} \times \sqrt{7}$ CDW phase in ML VSe₂.

Although a few STM studies reported the emergence of $\sqrt{3} \times 2$ and $\sqrt{3} \times \sqrt{7}$ CDW phase in ML VSe₂ ^[161,162], the detailed structural analysis is still lacking. In order to understand the nature of the CDW modulation, it is important to find out whether the modulation comes mostly from charge orderings or lattice distortions. Both spatial charge distributions and lattice structures contribute to STM topography, while differential conductance (dI/dV) spectroscopy resolves only the local charge distribution. Figs. 5.3a and 5.3c are the topographic and simultaneously taken dI/dV mapping images of ML VSe₂ at -1.5 V, respectively. Corresponding FFT images are also given at Figs. 5.3b and 5.3d, respectively. As shown in Fig. 5.3b, the CDW peaks (red circles) usually appear strongest for topographs. On the other hand, the diagonal modulation in the dI/dV mapping image (Fig. 5.3c) is difficult to discern, and the associated FFT peaks (red circles) are significantly

weakened compared to those in the FFT image. In order to get more systematic data, we measured the intensity ratio ($R = I_{\text{CDW}} / I_{\text{lattice}}$) of the CDW peaks (I_{CDW}) to the lattice peaks (I_{lattice}) at various bias ranges for both topography (R_T) and dI/dV mapping (R_M) images. Table 5.1 shows that the CDW modulations are stronger than hexagonal crystal lattices in topography images for all bias voltages ($R_T \geq \sim 1$). However, the CDW peaks are significantly suppressed in the dI/dV mapping images for all bias voltages ($R_T < 1$), indicating that charge orderings are not the driving factor of the CDW modulation. This result, therefore, suggests that the CDW modulation observed in STM topography is mostly from lattice distortions rather than charge orderings.

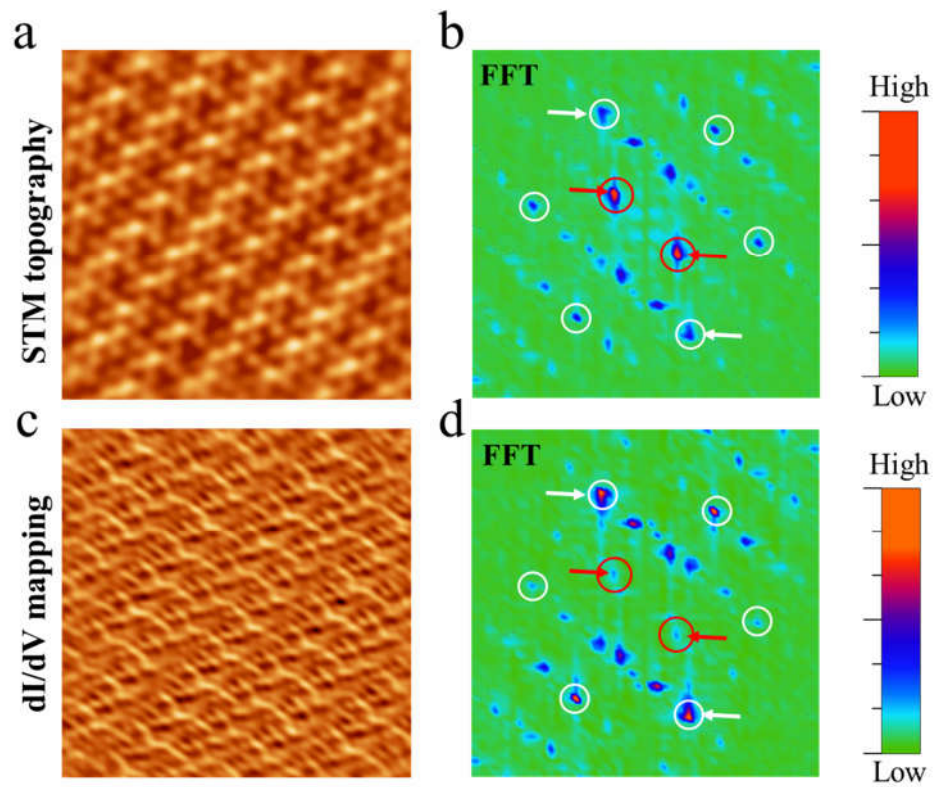


Figure 5.3: STM topography and dI/dV mapping images of ML VSe₂ on BLG. (a) STM topography image and (b) corresponding FFT image of ML VSe₂. (c) Simultaneously taken dI/dV mapping image and (d) corresponding FFT image. The white and red circles in (b) and (d) indicate the Bravais lattice of VSe₂ and CDW peaks, respectively. Scanning condition: $V_b = -1.5$ V, $I_t = 50$ pA. Scan size: $5 \text{ nm} \times 5 \text{ nm}$.

Bias (V)	Ratio of peak intensity ($R = I_{\text{CDW}} / I_{\text{lattice}}$)	
	R_T (topography)	R_M (dI/dV mapping)
1.8	0.91	0.37
1.6	1.09	0.53
1.4	1.05	0.64
-1.5	1.55	0.24
-2.2	2.16	0.32
-2.4	1.58	0.25

Table 5.1. The intensity of CDW phase in topography and dI/dV mapping. R is the intensity ratio ($R = I_{\text{CDW}} / I_{\text{lattice}}$) of CDW peaks (I_{CDW} , red arrows) to VSe₂ hexagonal lattice peaks (I_{lattice} , white arrows) in the FFT images of Figs. 5.3(b,d). R_T and R_M are the ratio values obtained from FFT images of topography and dI/dV mapping, respectively.

Detailed topographic analysis indeed verifies that the $\sqrt{3} \times 2$ and $\sqrt{3} \times \sqrt{7}$ modulations are directly linked with lattice distortions of the top Se atoms in ML VSe₂. Fig. 5.4 shows that the stripe CDW modulation consists of two alternate periodicities of $\sqrt{3} \times 2$ (pink rectangle) and $\sqrt{3} \times \sqrt{7}$ (black parallelogram). It is found that the stripe CDW modulation involves strong lattice distortions of Se atoms which appear as if they form pairs, i.e. the atomic spacing of Se-Se atoms is reduced to ~ 2.8 Å in Se pairs, compared to 3.2 Å for undistorted Se-Se atoms. As a result, two distinctive features of a spatial gap and an isolated Se atom exist as marked by pink and black circles, respectively, in Fig. 5.4a. Interestingly, the profile (Fig. 5.4b) taken from the blue line in Fig. 5.4a shows that the spatial gap and an isolated Se atom directly correspond to the $\sqrt{3} \times 2$ and $\sqrt{3} \times \sqrt{7}$ periodicities (marked by pink and black vertical arrows), respectively. Based on our observations, we propose a simple Se lattice distortion model (Fig. 5.4c). Further theoretical and experimental investigations are

required to elucidate the exact structural model of the $\sqrt{3} \times 2$ and $\sqrt{3} \times \sqrt{7}$ CDW phase in ML VSe₂.

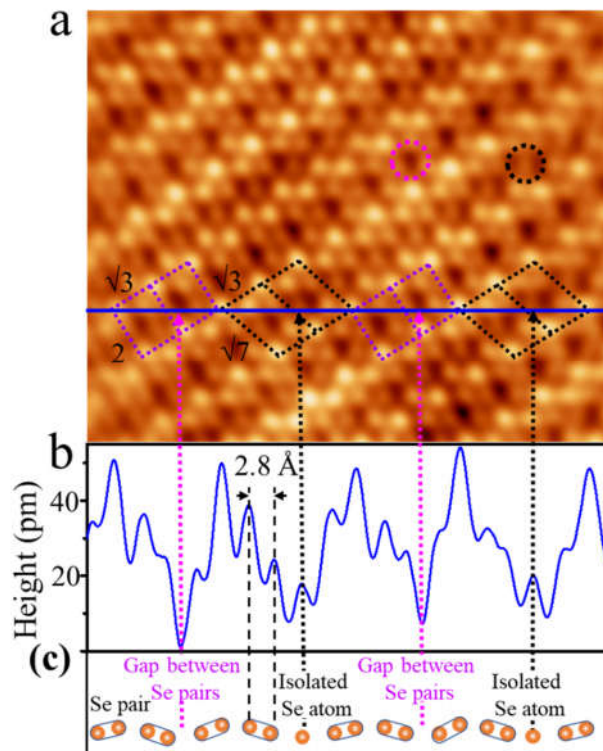


Figure 5.4: Lattice distortion of the top Se atoms. (a) STM topography of ML VSe₂ shows the CDW phase with $\sqrt{3} \times 2$ (pink rectangles) and $\sqrt{3} \times \sqrt{7}$ (black parallelograms) periodicities ($V_b = -1.5$ V, $I_t = 30$ pA). (b) The line profile is taken along the blue line in (a) and shows the strong lattice distortion of the top Se atoms. (c) Schematic model of Se lattice distortions.

5.1.3 Conclusion

Understanding the origin of the new CDW phase observed in ML VSe₂ is very important because it may provide insight into the role of dimensionality and heterointerfaces in TMD systems. It is therefore necessary to explore whether the main component of the CDW modulation is driven by charge orderings or lattice distortions. Interestingly, the CDW modulation is significantly suppressed in dI/dV mapping images while topographs always exhibit strong CDW phase regardless of applied bias voltages. This result indicates that the $\sqrt{3} \times 2$ and $\sqrt{3} \times \sqrt{7}$ CDW is mostly attributed to strong lattice distortions of Se atoms rather than charge orderings. Furthermore, we suggest that the lattice distortions of Se atoms appear as if they form pairs, giving rise to two topographic features of a spatial gap and an isolated Se atom. The spatial gaps and isolated Se atoms also directly correspond to the $\sqrt{3} \times 2$ and $\sqrt{3} \times \sqrt{7}$ periodicities of CDW phase, respectively.

5.2 Monolayer ReSe₂ on BLG

The vertical stacking van der Waals (vdWs) heterostructures constructed by graphene and thin atomic layered have been attracted many interests because of their potential in photodetector,^[168] field-effect transistors (FETs),^[169,170] Schottky diodes,^[171] etc. Besides transition metal dichalcogenides (TMDs)-based materials (MoS₂, MoSe₂, WSe₂),^[172,173] ReX₂ (X=Se, S) have been recently investigated for those purposes due to their in-plane anisotropy properties.^[174-176] In particular, ReSe₂/graphene heterostructure is reported as good candidate for conductive bridging random access memory (CBRAM),^[171] photodetection,^[177] FETs^[178]. Nevertheless, it was reported that FETs and infrared photodetector composed of ReSe₂ exhibit low charge carrier mobility and low responsivity of devices.^[179,180] To enhance the device performance, a clear understanding of ReSe₂/graphene interface is required. Unfortunately, the experimental and theoretical investigations on this issue are still very limited. For this reason, it is worth studying ReSe₂/graphene heterostructure using scanning tunneling microscopy.

Up to now, experimental studies on ReSe₂/graphene heterostructure have been focusing on the surface structure without discussing the interlayer coupling in detail. In previous work, the STM image of monolayer ReSe₂ showed a distorted 1T atomic structure.^[181] The moiré patterns were also resolved in the STM images of ReSe₂ overlaying graphene^[181] and graphene on ReSe₂^[182] due to a combination between triclinic lattice symmetry (monolayer ReSe₂) and a honeycomb lattice (graphene). That detailed information at the atomic level is very important to understand this ReSe₂/graphene system, however, to fully realize its application, further information is always required. For example, high mobility, which is attributed to low Schottky barrier height, are imperative for FETs.^[178] From angle-resolved photoelectron spectroscopy (ARPES) measurement, the minor

Schottky barrier ($<0.1\text{eV}$) is found in monolayer (ML) ReSe_2 on bilayer graphene (BLG), resulting in weak charge interaction at the interface.^[183] However, more experimental observations to deeper understand the graphene/ ReSe_2 interface are still needed. When metal and semiconductor approach each other, the charge at the interface might be redistributed due to semiconductor band edges aligning with metal Fermi level.^[184–188] To visualize the charge redistribution in other similar systems, the charge density difference (CDD) is theoretically calculated.^[184–188] In our best knowledge, there is no delicate experimental study resolving such charge distribution at the interface of vdW heterostructure.

In this work, we directly observe the trapped charge at ReSe_2 /graphene (R/G) interface in ML ReSe_2 grown on BLG materials via scanning tunneling microscope/spectroscopy (STM/S) measurements combined density functional theory (DFT) calculation. Scanning tunneling spectroscopy (STS) taken at ML ReSe_2 areas shows a band gap of 1.7 eV with conduction and valance band edges are 0.5 eV and -1.2 eV, respectively. When the scanning bias applied to the sample is either in the conduction band or valence band of ReSe_2 , the STM images of ML ReSe_2 on BLG shows a slight distorted hexagonal lattice of distorted 1T (1T') structure which is well agreed with DFT simulation results. Interestingly, STM image taken at bias range within the energy gap of ReSe_2 reveals an unexpected pattern following Re-chain of ReSe_2 layer, which is different from graphene atomic structure. The calculation of the charge density difference (CDD) at the R/G interface confirms that the unexpected feature taken at “in-gap” bias voltage is related to the top view of trapped charge distribution at the R/G interface. Furthermore, the trapped charge effect on ML ReSe_2 edge is significantly enhanced. We believe our work will provide a deeper understanding of interlayer coupling at R/G interface and open more opportunities to use this material in practical applications.

5.2.1 Atomistic and electronic structures of ML ReSe₂ on BLG

In Fig. 5.5a, the model structure of ML ReSe₂ is introduced. It was reported that the 1T' phase of ML ReSe₂ includes one Re atomic layer (white balls) in the between Se_{upper} (darker green balls) and Se_{lower} (light green balls) atomic layers. From the top view of 1T' phase in the bottom panel in Fig. 5.5a, every four adjacent Re atoms get closer forming Re₄ cluster (marked by the dashed diamond) and Re₄ clusters links along *a* direction.^[181,183]

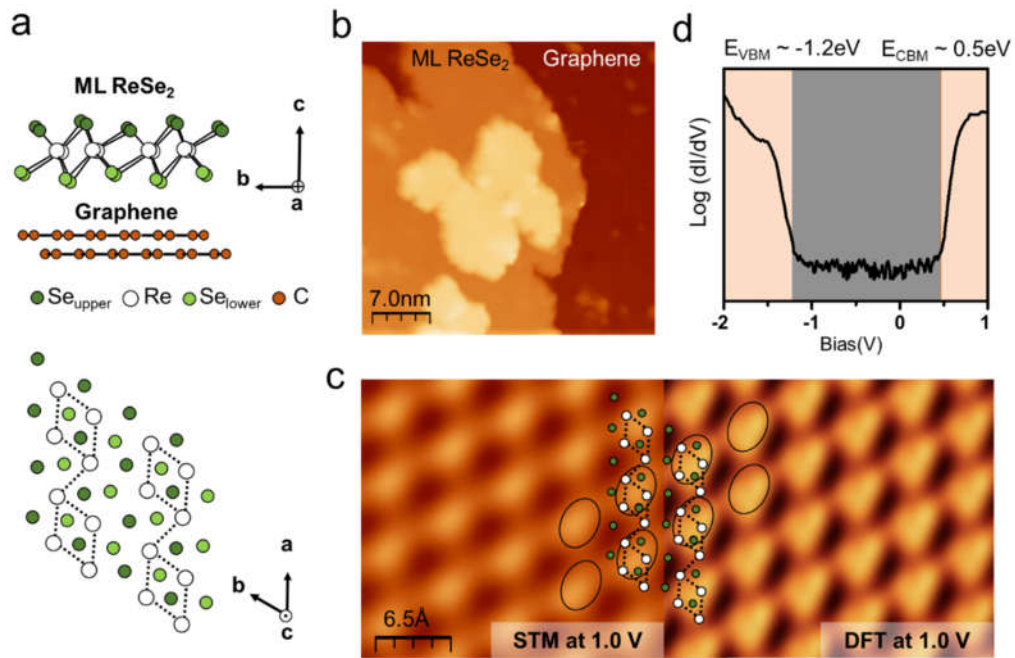


Figure 5.5: Introduce of ReSe₂ on BLG. (a) Model structure of ML ReSe₂ on graphene. Dark (light) green, white, and brown balls represent upper(bottom) Se, Re, and C atoms. Vector a , b , and c are three crystal axes. Vector a is along Re-chain direction. (b) The morphology of ReSe₂ on graphene ($V_b = 1.5$ V, $I_t = 30$ pA). (c) The STM image of ML ReSe₂ (left side) taken at bias voltage of 1 V is compared to the DFT simulated STM image (right side). The bright spots in STM images at 1 V are mostly attributed by upper Se and Re atoms. (d) The STS measurement displayed in logarithm scale ($\log(dI/dV)$) taken at ML ReSe₂ shows the valence band maximum (VBM) and conduction band minimum (CBM) at -1.2 eV and 0.5 eV, respectively.

The atomic structure of ML ReSe₂ on BLG/SiC is well resolved in STM images. The STM image in Fig. 5.5b shows that ML ReSe₂ has been successfully prepared on BLG. The STM image taken at 1V on ML ReSe₂ area shows the distorted hexagonal lattice, in Fig. 5.5c. To understand the origin of this structure, the scanning tunneling spectroscopy (STS) obtained at ML ReSe₂ and displayed in logarithm scale for convenience (Fig. 5.5d). By linear

fitting both sides of band edges, the valence band maximum and conduction band minimum energy levels (E_{CBM} ; E_{CBM}) are estimated at $(-1.2 \pm 0.05 \text{ eV}; 0.5 \pm 0.05 \text{ eV})$. From the electronic structure of ML ReSe₂, it is reasonable to claim that the structure observed at 1 V above E_{CBM} corresponds to ML ReSe₂ structure. Indeed, the measured lattice parameters, distance between two neighboring oval spots, along a and b directions are 6.6 Å and 6.5 Å, respectively, in line with previous works.^[182] Furthermore, previous STM studies on ML ReSe₂ reported similar structure, however, the origin of this structure was reported inconsistency. It was reported that Se_{upper} atoms attributed to STM image of ML ReSe₂ that is confirmed by the DFT calculation using Tersoff-Hamann approximation.^[189] While the other work believed that they observed Re atoms.^[181]

To give clear explanation of atomic feature in the STM image, we conducted DFT simulation using revised Chen's method. This method explicitly considers the contribution of the tip orbitals to the tunneling current, was proved beyond conventional Tersoff-Hamann method.^[190] The DFT simulation image at 1 V is displayed right panel of Fig. 5.5c showing reasonable agreement with the STM image. By overlying the model structure on both STM and DFT image, we found that the oval spot matches to both Se_{upper} atoms and Re₄ cluster position. Se_{upper} atoms are expected to be resolve because they are closest to the tip compared to Re and Se_{lower} atoms. For Re atoms, although they are much lower than Se_{upper}, the 5d state of Re are dominantly contributed to density of state. For this reason, both Se_{upper} atoms and Re₄ cluster are able to be resolved in STM image of ML ReSe₂. Above understanding on STM image of ML ReSe₂ will eventually help for further understanding R/G interface, going to discuss right below.

5.2.2 Trapped charge in vdW heterojunction of ML ReSe₂ on BLG

To further approach the R/G interface, we propose a measurement method by reducing tip-sample distance together with removing contribution of ReSe₂ states to tunneling current. In current constant mode of STM, to reduce tip-sample distance, we can either increase the setpoint or decrease the bias voltage applied to the sample (V_s). The second way is preferred because we can also eliminate the possibility of ReSe₂ states attributing to tunneling signal by reducing the V_s to the values within the energy gap of ReSe₂, namely “in-gap” bias voltage. The STM images taken in the ML ReSe₂ at “in-gap” bias voltage (from -1.2 eV to 0.5 eV) are carried out.

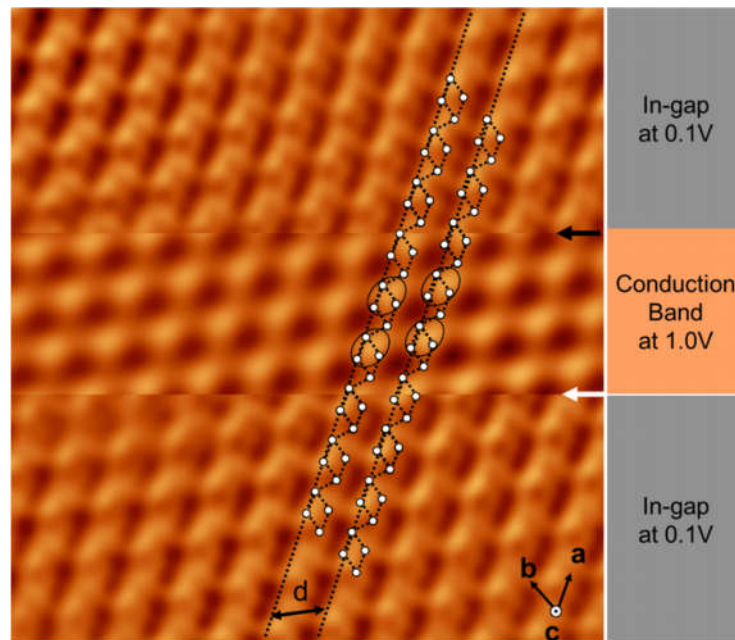


Figure 5.6: STM image taken at bias voltage within ReSe₂ energy gap. Within one scan image, the bias voltage is switched from 0.1 V to 1.0 V at the certain position (black arrow) and changed back to 0.1 V (at the white arrow position). The scanning condition at $I_t = 50$ pA.

To have a fair comparison, a switched-bias voltage STM image from the ML ReSe₂ area are shown in Fig. 5.6. While the tip is scanning from beginning to the black arrow position, the V_s is set at an “in-gap” bias voltage (0.1V). The tip is stopped at the position marked by black arrow, and then V_s is changed from 0.1 V to 1 V. The tip is continuously scanning until the white arrow position with the V_s is 1V. At the white arrow position, the tip is stopped again and then the V_s is changed back to 0.1V. Finally, we obtain the completed STM image including the upper, middle, and bottom parts which are corresponded to STM topography at 0.1V, 1V, and 0.1V, shown in Fig. 5.6.

The structure observed in middle part of Fig. 5.6 is consistent with Fig. 5.5c, whereas the STM topography parts taken at “in-gap” bias voltage reveal differently, namely “in-gap” pattern. This topography is not expected because the tip is now probing forbidden region of ReSe₂ band. However, it is reasonable to think this unexpected topography might relate to graphene substrate since the tip is approached closer to the sample surface and the graphene state is available at this bias range. Nevertheless, the features are totally different from that of graphene.^[161] Another possibility is the moiré patterns caused by lattice mismatch between graphene substrate and ML ReSe₂ but the moiré patterns in ReSe₂/graphene found in previous report have much longer periodicities.^[191] Besides, by overlaying the model structure of ML ReSe₂ in Fig. 5.6, we find that the “in-gap” pattern is following the Re-chain of ReSe₂ (dotted lines) with the periodicity (d) of 6.6 Å, implying that it is still somewhat related to ML ReSe₂. As the results, we believe that “in-gap” pattern is correlated to R/G interface.

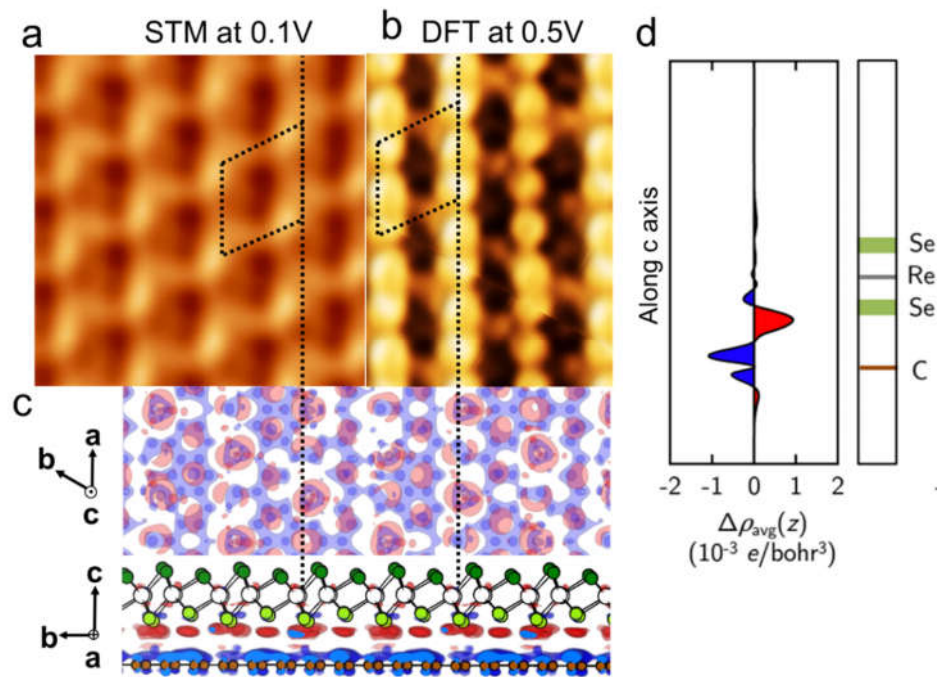


Figure 5.7: Origin of the “in-gap” pattern. (a) STM image taken from ML ReSe₂ area at 0.1 V ($I_t = 50$ pA) is compared to (b) DFT simulated STM image at 0.5 V. (c) The trapped charge distribution between vdW gap graphene and ReSe₂ monolayer along top view (upper) and side view (bottom). (d) Plane-averaged charge density different (CDD) along the c axis. The red and blue colors present accumulated and depleted electron regions, respectively. The size of (a) is 2.3 nm \times 2.3 nm.

The exact origin of “in-gap” pattern is clarified by the density functional theory (DFT) calculations. The “in-gap” STM topography (Fig. 5.7a) is directly compared to the DFT simulated STM image at the bias within the energy gap of ML ReSe₂ on graphene (Fig. 5.7b). Both STM and the DFT images show pattern with combination of linear (the dotted lines) and hexagonal features (the dotted parallelogram), indicating that they are agreed well each other. Interestingly, the features in Fig. 5.7a-b are matching with the top view of charge density difference (CDD) distribution in Fig. 5.7c. The charge density difference is

calculated as follows: $\Delta\rho = \rho_{R/G} - \rho_R - \rho_G$, where $\rho_{R/G}$, ρ_R , and ρ_G are charge density of the ReSe₂/graphene heterostructure, ML ReSe₂, and graphene, respectively. To have quantitative picture of charge distribution, the plane averaged CDD, $\Delta\rho_{\text{average}}(z)$, along *c* direction is plotted in Fig. 5.7d where the blue and red colors represent electron depletion and accumulation regions. Fig. 5.7d indicates that the electron density near the top surface of graphene is transferred to ML ReSe₂ and accumulated (trapped) right below Se_{lower} atoms. Thus, remarkable charge rearrangement occurs at the R/G interface, see the side view of this charge distribution in the bottom of Fig. 5.7c. Accordingly, the unexpected pattern observed at the bias within the energy gap of ReSe₂ is the trapped charge distribution in *ab*-plane.

As mentioned above, the trapped charge layer is formed right below the Se_{lower} atomic layer, suggesting that the small step of trapped charge layer with respect to graphene should be observed at the bias voltage within the energy gap of ML ReSe₂. STM images including both ML ReSe₂ terrace and graphene substrate taken at 1.5 V and 0.3 V are showing in Fig. 5.8a and b, respectively. The solid (dashed) orange line profiles at 1.5 V (-2 V), which locate in the conduction band (valance band) in Fig. 5.8c reveal the typical step edge of ML ReSe₂ on graphene around 8 Å. This value includes the vdW gap and the thickness of single ReSe₂ slab. While the solid (dashed) black line profiles at 0.3 V (-1V) reveal that the step between ML ReSe₂ terrace area and graphene show a smaller value of 3.6 Å, which is comparable to theoretical value of R/G vdW spacing (3.44 Å). This again confirms the existence of trapped charge layer in the R/G interface.

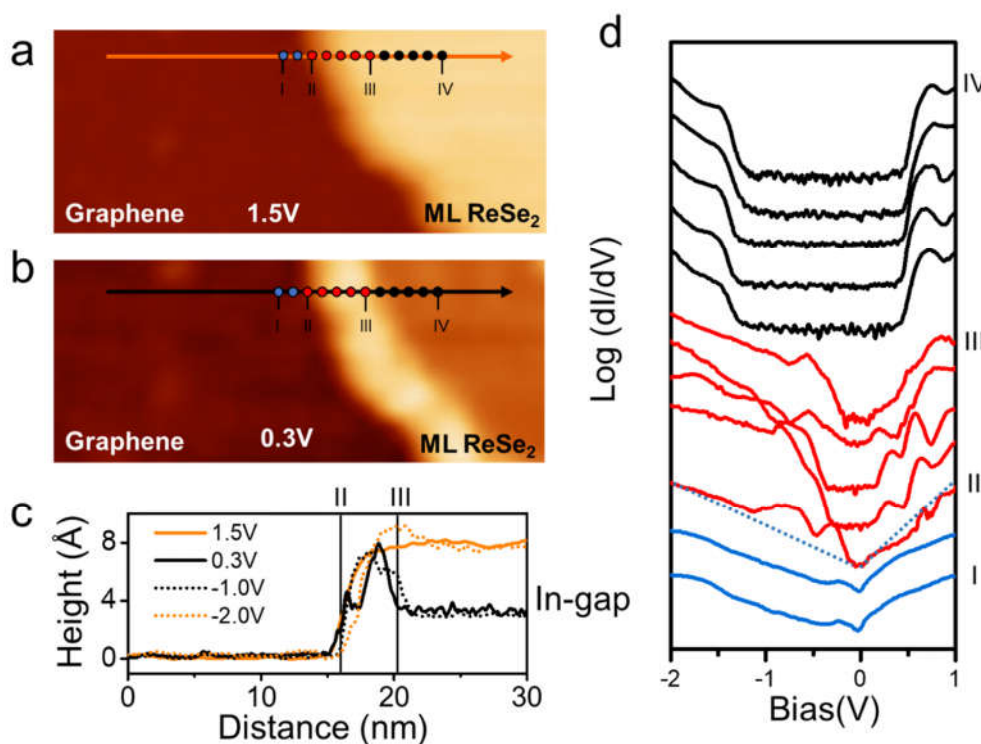


Figure 5.8: Effect of trapped charge on the edge of ML ReSe₂ on BLG. (a-b) STM images of ML ReSe₂ on BLG taken at bias voltages of 1.5 V (in conduction band of ReSe₂) and 0.3 V (“in-gap” bias voltage), respectively. The edge feature is significantly enhanced at “in-gap” bias voltage. The size of STM images in (a) and (b) are 35 nm × 15 nm. (c) The line profiles obtained from bias dependent STM images of the edge. The solid (dotted) black and orange line profiles are obtained from STM taken at positive (negative) bias voltages locating within the energy gap and conduction (valence) band of ReSe₂. (d) The STS measured along a line crossing the edge of ML ReSe₂ on BLG from position “I” to “IV” marked in (a-c). All STS in (d) are converted to logarithm scale; the blue dashed lines indicate the tendency of graphene electronic structure.

In addition, we also investigate the trapped charge effect on ML ReSe₂ edge via the STM/S measurements. From the bias dependent STM image in Fig. 5.8a-b, the edge feature become obvious at “in-gap” bias voltages, while it is not distinguishable from the ML ReSe₂ terrace at 1.5V. In fact, the height of the edge region at 0.3 V or -1V (as shown in Fig. 5.8c)

is greater than that of ML ReSe₂ terrace area. Besides, the electronic evolution from metallic (graphene) to semiconducting (ML ReSe₂) behavior is also conducted. The dI/dV line spectra are measured from position “I” to “IV” in Fig. 5.8a, crossing graphene, edge, and ML ReSe₂ areas, displayed in Fig. 5.8d. From the red curves taken at the transition region, general behavior such as band-bending^[192,193] or metal induced gap states^[194,195] is not observed. Instead, we found undefined electronic with small gaps which might be driven by graphene (indicated by the dashed V-shape in Fig. 5.8d). It was reported that charge redistribution at vdW heterostructure could form an interface dipole.^[188] We could expect the dipole field produced at R/G interface. Moreover, this dipole field could be affected by dangling bonds that disturbs electronic structure at the edge region. Therefore, the strong edge feature and undefined electronic behaviors again prove the presence of trapped charge layer at R/G interface.

5.2.3 Conclusion

As the results, we provide delicate experimental observation in the trapped charge layer at R/G interface. Although the interaction between ReSe₂ and graphene is weak vdW, the charge from graphene is still transferred to ReSe₂ and trapped underneath Se_{lower} atomic layer. More interestingly, this trapped charge layer forms a pattern following the Re- chain, which can be resolved in STM image by applying an “in-gap” bias voltage to the sample. Those understanding about trapped charge at R/G interface is very critical in the view of device application because the interlayer coupling is an effective way to improve the device performance.

Chapter 6

Ultrathin Cu₂O Films

Beside van der Waals materials, we are also interested in ultrathin films of Cu₂O sample surface. In this chapter, we will discuss about stoichiometric surface structure and intrinsic defect of Cu₂O.

6.1 Introduction

Copper (I) oxide, or cuprous oxide (Cu₂O), is a p-type semiconductor with a direct band gap of ~2.1 eV.^[196] Cu₂O has been widely investigated due to its various potential applications such as solar cells,^[197,198] photocatalytic splitting of water,^[199–203] and CO oxidation.^[204] Notably, it is rather uncommon for binary oxides to possess p-type characteristics due to the omnipresent defect of oxides (oxygen vacancy), which tends to provide electron donors and lead to n-type behavior. Here, what makes Cu₂O a unique choice of oxide material is its intrinsically stable p-type nature. Although there are some technical obstacles such as high off-state current,^[205,206] and low hole mobility,^[207] Cu₂O is considered a promising candidate for a p-type counterpart in oxide-based electronics. It is often stated that the p-type character originates from hole-producing Cu vacancies, which are easily generated due to low formation energy.^[208,209] The shallow acceptor level of a Cu vacancy can effectively supply holes in Cu₂O.^[209] Although this is the generally accepted mechanism of p-type conduction in Cu₂O, clear and direct observation of both the atomic and electronic characteristics of the Cu vacancy is lacking.

The O/Cu(111) system has been intensively studied to understand the complex nature of the oxidation process. At the early stage of oxidation, Cu₂O-like surfaces, the so-called

“44” and “29” structures, are formed and consist of Cu-O hexagonal rings, functioning as precursors to bulk Cu_2O .^[210–216] It has been reported that CO reduction can convert “44” and “29” structures to defective structures with pentagonal and heptagonal Cu-O rings as a metastable phase.^[204] Closely related to these studies, the actual surface structures and terminations of $\text{Cu}_2\text{O}(111)$ have been a subject of debate. A recent study involving scanning tunneling microscopy (STM) and hybrid density-functional theory (DFT) calculations suggest that the stoichiometric surface of $\text{Cu}_2\text{O}(111)$ is more stable under oxygen-lean conditions, contradicting previous semi-local DFT predictions where the formation of a Cu vacancy is deemed to be thermodynamically favorable.^[217,218] This vacancy formation on $\text{Cu}_2\text{O}(111)$, which corresponds to removal of the coordinately unsaturated Cu (Cu_{CUS}) atom, is supported by recent X-ray photoelectron spectroscopy measurements.^[219] Further high-resolution experiments and simulations are still needed to shed more light on the actual surface termination of $\text{Cu}_2\text{O}(111)$.

The manipulation and augmentation of $\text{Cu}_2\text{O}(111)$ surface for various applications have been thoroughly investigated. To pursue those objectives, the growth of the high crystalline phase of Cu_2O surface is of interest. In these aspects, several experimental groups have prepared ultrathin crystalline Cu_2O surfaces in UHV condition and investigated its fundamental properties such as the morphological changes,^[220,221] the structural properties of defects on $\text{Cu}_2\text{O}(111)$ surface under the controlled conditions,^[215,222] and the adsorption behavior of water molecules on prepared surfaces.^[223,224] In particular, Nilius *et al.* prepared high crystalline $\text{Cu}_2\text{O}(111)$ surface on $\text{Au}(111)$ (where their structural coherence is about 4.2%).^[217,223] However, the preparation of the high crystalline $\text{Cu}_2\text{O}(111)$ surface on $\text{Cu}(111)$ surface is rather challenging due to the anticipated high lattice mismatch.

In this work, we investigate the surface structures and intrinsic point defects of $\text{Cu}_2\text{O}(111)$ thin films grown on $\text{Cu}(111)$ surfaces via the combination of DFT calculations and home-built low-temperature STM. In particular, our DFT-derived simulated STM images are obtained beyond the simple Tersoff-Hamann approximation to consider explicitly the orbital contribution from the STM tip. Our combined STM/DFT studies indicate that $\text{Cu}_2\text{O}(111)$ is indeed stoichiometric where the Cu_{CUS} atoms appear as bright spots with a hexagonal structure in STM topography. Also, besides the possibility of kinetically-formed oxygen vacancies reported in previous work,³⁰ intrinsic defects identified as a Cu vacancy and Cu adatoms commonly exist on $\text{Cu}_2\text{O}(111)$ surfaces. The inverted contrast behavior of filled and empty state probes of V_{Cu} indicates that the surface V_{Cu} is negatively charged. Accordingly, the dI/dV spectrum taken at the single V_{Cu} reveals the strongly enhanced conductance at negative bias range, compared to that of the defect-free area. This charged behavior is attributed to the acceptor character of V_{Cu} . Our observation confirms that the surface V_{Cu} provides holes to Cu_2O system at the atomistic level.

6.2 Sample preparation

Fig. 6.1 describes the processes of the high-quality $\text{Cu}_2\text{O}(111)$ surfaces prepared on $\text{Cu}(111)$ films. Firstly, highly crystalline $\text{Cu}(111)$ films grown on sapphire (Al_2O_3) substrate are oxidized at ambient conditions (room temperature), and about 5-nm-thick surface oxide is formed on $\text{Cu}(111)$ film during this procedure. High-quality $\text{Cu}_2\text{O}(111)$ surfaces are prepared on $\text{Cu}(111)$ films by three cycles of Ar^+ sputtering at 0.5 kV for 10 min under Ar^+ pressure of 2.5×10^{-5} Torr, and annealing at 600°C for 30-45 min. The Ar^+ sputtering and annealing procedures are done in ultra-high vacuum (UHV) STM chamber.

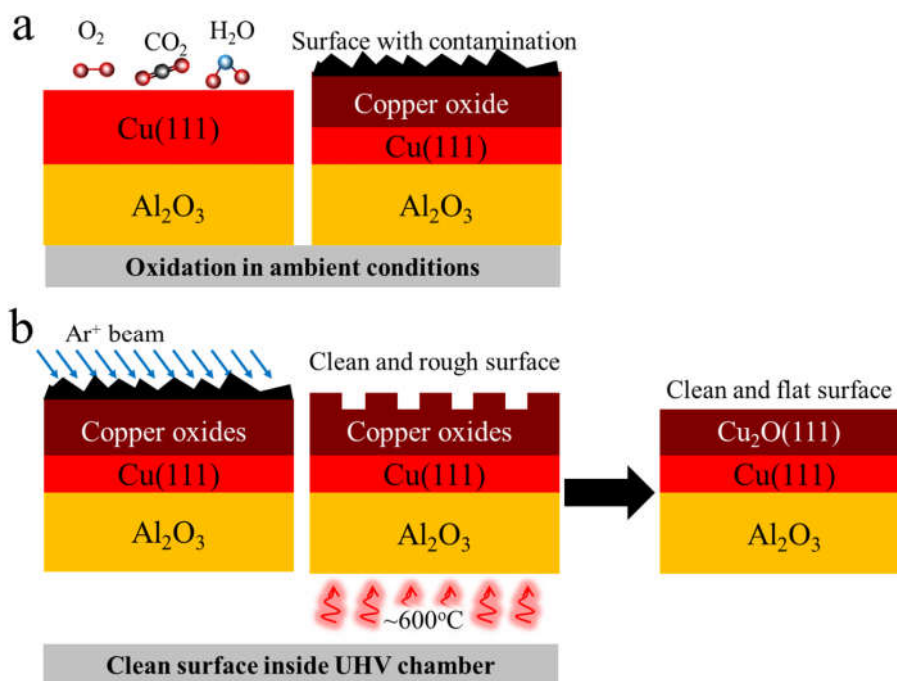


Figure 6.1: Two process of Cu_2O surface preparation. (a) Oxidation in ambient conditions.

(b) Cleaning surface inside UHV chamber.

6.3 Surface structure

The role of the metal host is essential in the preparation of high-quality oxide surfaces. Highly crystalline Cu(111) thin films are prepared on sapphire substrate, and a ~5-nm-thick surface oxide is formed on Cu(111) film under ambient conditions. The clean Cu₂O(111) surface is obtained by Ar⁺ sputtering and annealing at 600°C in an ultra-high vacuum (UHV). In Fig. 6.2a, STM topography exhibits a uniformly oxidized surface with well-ordered triangular terraces. The line profile taken along the blue arrow shows the single step height of Cu₂O film about 2.1 Å which is similar to that of Cu(111).

As shown in Fig. 6.2c, the stoichiometric Cu₂O(111) surface consists of coordinatively unsaturated copper (Cu_{CUS}), coordinatively saturated copper (Cu_{CSA}), coordinatively unsaturated oxygen (O_{CUS}), and coordinatively saturated oxygen (O_{CSA}). From the structure model, the O_{CUS} has only bonding with the underneath oxygen (O_{under}). Therefore, nonstoichiometric surface without Cu_{CUS} (Cu₂O(111)–Cu_{CUS} structure) could be possible. To date, it is still debatable whether the nonstoichiometric surface is thermodynamically more favorable than the stoichiometric surface. Complementing the STM imaging, the role of DFT simulation is critical to resolve this issue. All DFT-simulated STM images hereafter are based on the revised Chen's method that explicitly includes the tip orbitals.

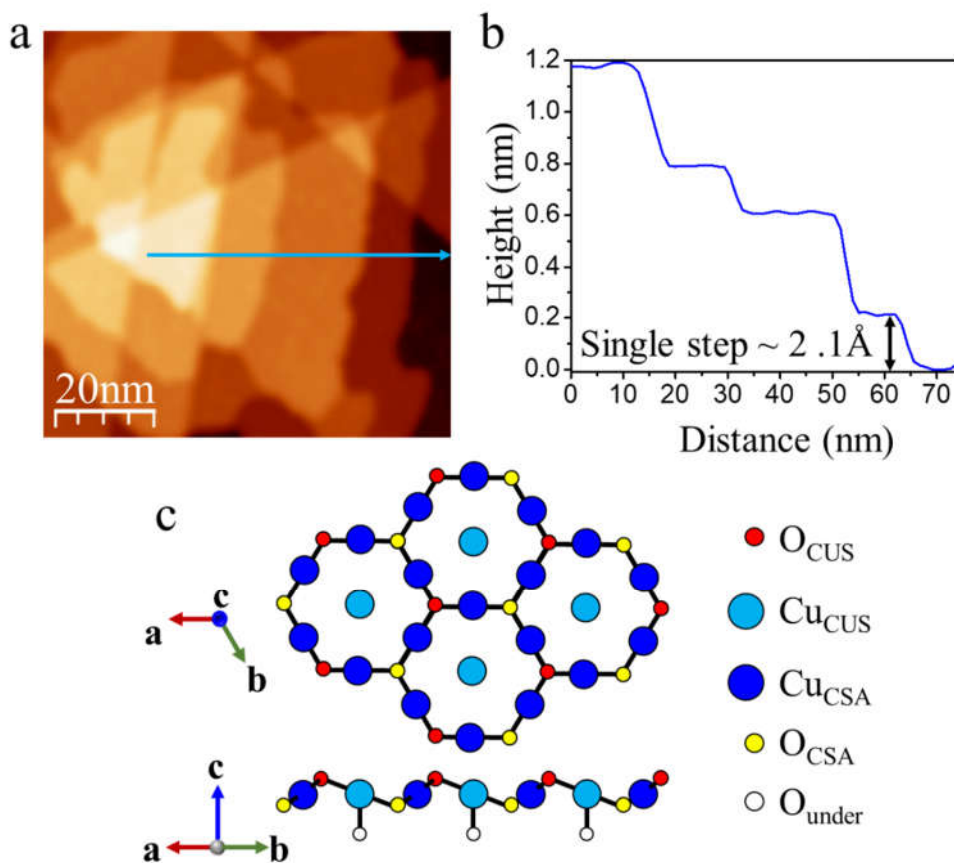


Figure 6.2: Surface structure of Cu₂O(111) films. (a) Large-scale STM topography of the Cu₂O(111) surface shows well-ordered terrace structures ($V_s = 4.5$ V, $I_t = 30$ pA). (b) The line profile taken along the blue arrow in (a) showing the single step about 2.1 Å. (c) The top and side view of structure model of stoichiometric Cu₂O(111) surface. The red, light blue, dark blue, yellow, and white circles represented for coordinatively unsaturated oxygen (O_{CUS}), coordinatively unsaturated copper (Cu_{CUS}), coordinatively saturated copper (Cu_{CSA}), coordinatively saturated oxygen (O_{CSA}), and underneath oxygen atoms.

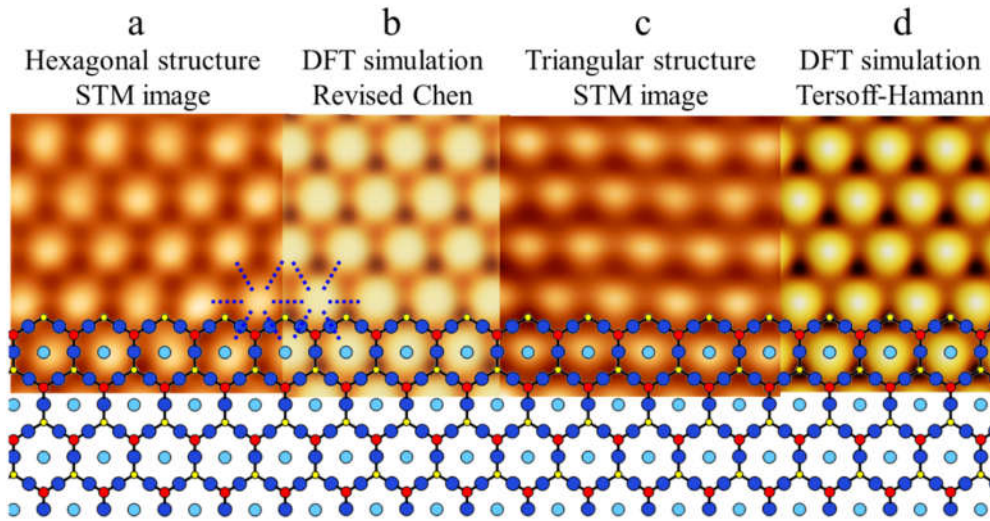


Figure 6.3: Atomic structure of $\text{Cu}_2\text{O}(111)$ surface. (a) High-resolution STM image exhibits hexagonal structures of stoichiometric $\text{Cu}_2\text{O}(111)$ surface ($V_s = 1.4$ V, $I_t = 30$ pA). (b) STM image of stoichiometric $\text{Cu}_2\text{O}(111)$ surface is simulated at +1 V with the revised Chen's approach using a sharp tip apex on W(110). (c) High-resolution STM image exhibits triangular structures of stoichiometric $\text{Cu}_2\text{O}(111)$ surface ($V_s = 0.2$ V, $I_t = 30$ pA). (d) STM image of stoichiometric $\text{Cu}_2\text{O}(111)$ surface is simulated at +1 V with the Tersoff-Hamann method. Top-view structural model of the stoichiometric $\text{Cu}_2\text{O}(111)$ surface is overlaid on the STM and simulated STM images. The bright line features in experimental and simulated STM images are denoted as dashed lines in (a) and (b). Image size of (a) and (b) are $3\text{ nm} \times 3\text{ nm}$.

A high-resolution image shows bright spots of a hexagonal lattice, as shown in Fig. 6.3a. Our DFT simulation of the stoichiometric $\text{Cu}_2\text{O}(111)$ surface using the revised Chen's method (Fig. 6.3b) shows good agreement with STM topography (Fig. 6.3a), confirming termination of the $\text{Cu}_2\text{O}(111)$ surface where the bright spots correspond to Cu_{CUS} atoms. Moreover, we are able to unveil some fine structures in the STM images of the stoichiometric $\text{Cu}_2\text{O}(111)$ surface. The bright linear features marked by dashed lines in Fig. 6.3a and 6.3b match very well and clearly coincide with the positions of the Cu_{CSA} atoms. On the other

hand, the 3-fold symmetry reflecting O_{CUS} atom and O_{CSA} atom around Cu_{CUS} atoms in the simulated image of Fig. 6.3b is not visible in the STM image of Fig. 6.3a, but appears in different bias image in Fig. 6.3c, suggesting that the 3-fold symmetry in Fig. 6.3b is also real. It is noted that the bright linear features are pronounced when we compare the STM images simulated with the revised Chen's method (Fig. 6.3b) with those of the Tersoff-Hamann approach (Fig. 6.3d). This result implies that including the contribution of the tip states to the STM simulation is important in capturing the correct electronic structure of the Cu_2O surface.

Our measured lattice constant (distance between Cu_{CUS} atoms) of prepared $Cu_2O(111)$ surface is $\sim 6.5 \text{ \AA}$ which is much larger than that of Cu_2O layer on $Au(111)$ (6.00 \AA) or that of bulk Cu_2O (6.04 \AA).^[220,223] The strained lattice constant (of about 8.33 %) as compared to the optimal lattice constant is attributed to the role of the $Cu(111)$ support where structural incoherence between the thin oxide and $Cu(111)$ can exist.

6.4 Intrinsic defect – An origin of p-type characteristic

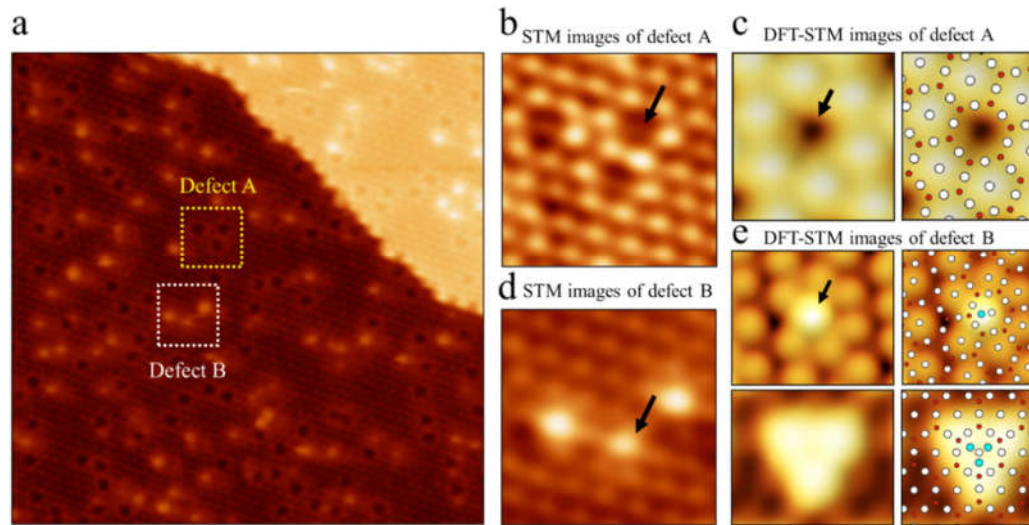


Figure 6.4: Intrinsic defects in the $\text{Cu}_2\text{O}(111)$ surface. (a) Two different defects labelled defects A and B are observed in STM topography (size: $30 \times 30 \text{ nm}^2$). (b) and (d) High-resolution STM images of the locations marked by yellow (defect A) and white (defect B) boxes in (a), respectively (size: $4 \times 4 \text{ nm}^2$). All STM images are produced at $V_s = 1.6 \text{ V}$ and $I_t = 30 \text{ pA}$. Simulated STM images (using revised Chen's approach) are shown for defect A (at $+1.5 \text{ V}$) in (c) and defect B (at $+1.5 \text{ V}$) in (e) with surface atomic structures. (c) For defect A, one Cu_{CUS} vacancy defect exists on the $p(2 \times 2)$ Cu_2O surface supercell. (e) For defect B, the STM images are simulated with one Cu adatom (upper) and three-adatom (lower) models to confirm possible Cu clusters on the $p(3 \times 3)$ surface supercell. The atomic structures are overlapped to the simulated STM images. The Cu, O, and Cu_n atoms are depicted as white, red, and turquoise circles, respectively.

We further investigate intrinsic defects existing on $\text{Cu}_2\text{O}(111)$ surfaces in STM topography. Two types of defects labelled defects A and B are observed in Fig. 6.4a. The high-resolution image in Fig. 6.4b indicates that defect A originates from removal of the

surface Cu_{CUS} atom, as marked by an arrow, suggesting that defect A is the Cu_{CUS} vacancy (hereafter, will be represented by surface V_{Cu}). This is supported by our DFT-STM simulations where the topographs of both experiment and theory agree very well (Figs. 6.4b and 6.4c).

As shown in Table 6.1, the calculated defect formation energy of surface V_{Cu} is thermodynamically favorable. Concurring with a recent work,^[225] the bright circular features are caused by the six Cu_{CUS} atoms surrounding the surface V_{Cu} (defect A), while the dark almost-triangular feature is strongly associated with the surface V_{Cu} .

Defect	E_{Defect}^f (eV/Defect)	E_{Pair}^f (eV/Pair)
V_{Cu}	-1.71	-
Cu_1	+0.31	-
Cu_3	+0.53	-
$1V_{\text{Cu}}+\text{Cu}_1$	-	-1.40
$3V_{\text{Cu}}+\text{Cu}_3$	-	-1.19

Table 6.1. Defect formation energy of single and paired surface defects of $\text{Cu}_2\text{O}(111)$.

In contrast, defect B shows bright protrusions on top of the surface, as shown in Fig. 6.4d. The bright protrusions show slight variance in brightness and topology, i.e., their sizes and brightness vary somewhat from defect to defect. Interestingly, similar features of our measure STM images of defect B was observed in a previous work where the possibility of Cu adatom formation on $\text{Cu}_2\text{O}(111)$ surface was proposed. In that work, the origin of the most common bright protrusion features of the STM images was assumed to be the isolated

Cu atom binding on top of the O_{CUS} atom with other various types of adatom defect configurations and sizes suggested.^[226]

Thus, to further verify the presence of Cu adatoms on $\text{Cu}_2\text{O}(111)$, we perform DFT calculations of possible Cu clusters (Cu_n) on $\text{Cu}_2\text{O}(111)$. Here, we choose to model the isolated Cu adatom (majority; denoted as Cu_1) and larger adatom clusters with three Cu atoms (denoted as Cu_3) as representative cases to test the possible adsorption sites on $\text{Cu}_2\text{O}(111)$.

From our calculations, the single Cu adatom binds to the “quasi” three-fold hollow site (i.e., located at two Cu_{CSA} and one Cu_{CUS} atoms), forming O-Cu chemical bonds to the nearest O_{CUS} atom with a bond distance of 2.04 Å. This is 10 % larger than the bond length between $\text{Cu}_{\text{CSA}}\text{-}O_{\text{CUS}}$ on the stoichiometric surface (at 1.84 Å). Our DFT-simulated STM image (Fig. 6.4e) for this surface defect captures the anisotropic bright feature of the experimental STM image (Fig. 6.4d). With brighter circular feature originated from Cu_1 atom, Cu_{CUS} atoms at outermost surface possess the bright protrusion feature which can be observed in the experimental measurement.

To investigate the thermodynamic stabilities of these defects, the $E_{\text{Defect}}^{\text{form}}$ of Cu_1 is calculated with respect to the stoichiometric $\text{Cu}_2\text{O}(111)$. Our results show that the Cu adatom defect is unfavorable with $E_{\text{Defect}}^{\text{form}} = +0.31$ eV (Table 6.1). However, interestingly, when we compute the formation energy of a defect pair (which is composed of one V_{Cu} and Cu_1) $E_{\text{Pair}}^{\text{f}}$, the formation of Cu_1 in the presence or co-existence of surface copper vacancies is indeed favorable ($E_{\text{Pair}}^{\text{f}} = -1.40$ eV). These results imply that the formation of defect B (cluster) is the natural consequence of the formation of defect A (Cu vacancy). The extracted Cu_{CUS} atoms from the center of Cu-O hexagonal rings may now bind to a “quasi” three-fold hollow site on $\text{Cu}_2\text{O}(111)$. We confirm our preliminary hypothesis via a statistical analysis

of the experimentally measured defect densities of A and B. The counted density of defect A and B is about 0.1 defects/nm² and 0.08 defects/nm², respectively, lending support that the relative ratio between defect A and B is fairly similar.

Indeed, with a closer inspection of the simulated STM image of Cu adatom clusters (for both Cu₁ and Cu₃; in the Fig. 6.4e), one will find similar topographs with the experimental image and thus suggesting the possible presence of small Cu adatom defects (defect B) on the stoichiometric Cu₂O(111) surface. The observed Cu adatom shows completely different topographic features from the triangular shape of oxygen vacancies reported in single crystals.³⁰ This implies that our strained Cu₂O thin films grown on the Cu substrate can have different surface defect characteristics (e.g. formation energies and electronic structures) as compared to those of Cu₂O single crystals. We note, however, as discussed in other work^[226], the observed bright protrusion features may also be signature of complex Cu-O defect (Cu_nO_m) formation on this oxide surface.

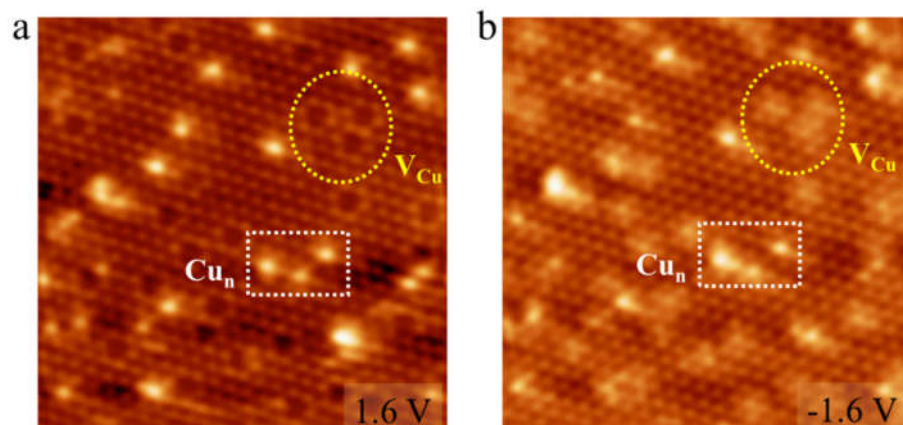


Figure 6.5: Bias polarity dependence of STM images at the same location. Cu vacancies (V_{Cu}) and Cu clusters (Cu_n) present different contrast behavior in (a) empty and (b) filled state images (size: $15 \times 15 \text{ nm}^2$).

These two defects, V_{Cu} and Cu_n , present very different electronic characteristics depending on the polarity of the sample bias. Figs. 6.5a and 6.5b exhibit topographic images for the same location at +1.6 V and -1.6 V, respectively. Interestingly, the hollow feature of V_{Cu} in the empty state becomes a bright spot in the filled state, while Cu_n remains unchanged as a bright protrusion in both states. Such inverted contrast behaviors of V_{Cu} imply that V_{Cu} is not neutral but negatively charged. Recalling theoretical predictions that the p-type nature of Cu_2O is attributed to V_{Cu} ,^[209] V_{Cu} easily ionizes to its -1 state by producing a hole carrier. Because Cu_n is just an adatom cluster sitting on top of the Cu_2O surface, it should always appear as a bright protrusion in topography regardless of the bias voltages and polarities.

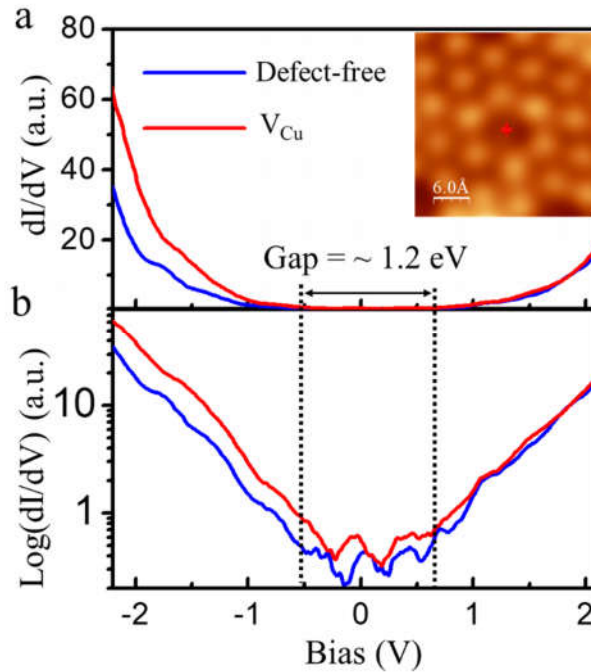


Figure 6.6: Electronic structure of V_{Cu} . dI/dV spectroscopy taken at V_{Cu} (red curve) and a defect-free area (blue curve) (a) on linear scale and (b) on log scale. The I-V spectra are obtained with initial set-current 50 pA at 2.5 V (feedback off) and dI/dV signal is simultaneously measured by a typical lock-in technique (modulation amplitude of 10 mV and frequency of 1.2 kHz).

The electronic nature of V_{Cu} is further investigated by performing dI/dV spectroscopy at the single-defect level. Fig. 6.6 shows dI/dV spectra obtained from the center of V_{Cu} (red, see inset) and a defect-free area (blue). The spectrum of V_{Cu} reveals strong enhancement in the negative bias range compared to the defect-free area. Again, this is a typical characteristic of a negatively charged defect.^[83] The charged behavior is attributed to the acceptor character of V_{Cu} . We observe a smaller gap size of ~ 1.2 eV (compared to the 2.1 eV in the bulk oxide) in our ultrathin Cu_2O film samples, and we attribute this to the influence of the underlying Cu metal support.

6.5 Conclusion

High-quality $\text{Cu}_2\text{O}(111)$ surfaces are prepared by ambient oxidation of $\text{Cu}(111)$ film and show very well-ordered, triangular terraces. STM studies combined with DFT calculations clarify that $\text{Cu}_2\text{O}(111)$ has a stoichiometric surface where Cu_{CUS} atoms are observed with a hexagonal structure. In this study, DFT-derived simulations of STM images are obtained by explicitly adding the orbital contributions from the STM tip to the simple Tersoff-Hamann approximation. Both high-resolution STM topography and DFT-STM simulations consistently reveal the fine structure of stoichiometric $\text{Cu}_2\text{O}(111)$ surfaces, showing the detailed features of the Cu_{CSA} atoms. Cu_2O is intrinsically copper deficient due to the low formation energy of V_{Cu} .^[208] However, the existence of surface V_{Cu} and its electronic properties have been rarely investigated at the atomistic level. Two surface defects commonly exist on $\text{Cu}_2\text{O}(111)$ and are identified as V_{Cu} and Cu_{n} . Unlike Cu_{n} , V_{Cu} exhibits a negatively charged behavior in both topography and spectroscopy measurements, unequivocally demonstrating the acceptor character of surface V_{Cu} . Here, we confirm that copper vacancies provide holes not only in bulk defects, but also at the surface, which could be important for device applications.

Appendix A – Tip state effect to STM topography images of SnSe

For example, Fig. A1 showing the different features obtained in STM topography images of SnSe surface. It well known that STM topography images of SnSe showing the rectangular periodicity of Sn atoms regardless of bias conditions. In this discussion of STM observations of SnSe surface, it is assumed that the W tip is in a four-lobe d orbital state such as d_{xy} and $d_{x^2-y^2}$, which are the dominant states at the Fermi level. However, the atomic features of SnSe that are observed can totally change when the tip state is altered. Occasionally, we obtain the topographic images shown in Fig. A1a which present two major differences compared to Fig. A1b. First, the apparent radius of the Sn atoms (the brightest spots) is significantly reduced. Second, new atomic features appear at the position of Se atoms, as marked by the green dashed circles in Fig. A1b

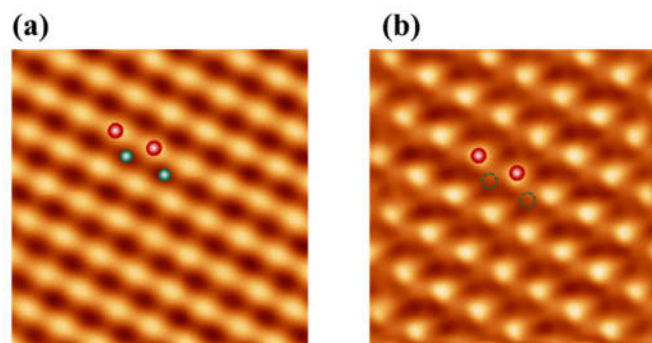


Figure A1: STM topography images of SnSe surface taken with different tip states. (a)

Typical four-lobe d state tips and (b) d_{z^2} state tips.

Fig. A2a presents typical topographic images of a SnSe surface obtained by a four-lobe d state tips. The profile of Fig. A2c, taken along the black dashed line (ABC), shows

that the corrugation amplitude and apparent atomic radius of Sn atoms are around 14 pm and 1.8 Å, respectively. On the other hand, Fig. A2b shows much sharper atomic features of the Sn atoms. Indeed, the corrugation amplitude remarkably increases to around 70 pm, and the apparent radius of the Sn atoms also noticeably decreases to around 1.3 Å in the line profile (ABCD) (Fig. A2d). All these observations agree very well with the characteristics of a d_{z^2} state W tip, so the improved topography of the SnSe surface seen in Fig. A2b can be attributed to the d_{z^2} state of the W tip. Interestingly, weak atomic features of Se atoms are also observable, as labelled with green dashed circles in Fig. A2b. This implies that the sharply focused shape of the d_{z^2} state helps to detect the hidden Se $4p_z$ states of SnSe surfaces. There are also bright connections between Sn and Se atoms in Fig. A2b which could be some features of Sn and Se atoms from the bottom layer of SnSe surfaces detected by the sharp d_{z^2} state. We were able to get the d_{z^2} state only when a negative bias is applied to the sample allowing the migration of W^+ ions. Although the d_{z^2} state is not controllable, it usually happens in the bias range of - 0.5 to - 2 V which would also depend on the shape and sharpness of W tip.

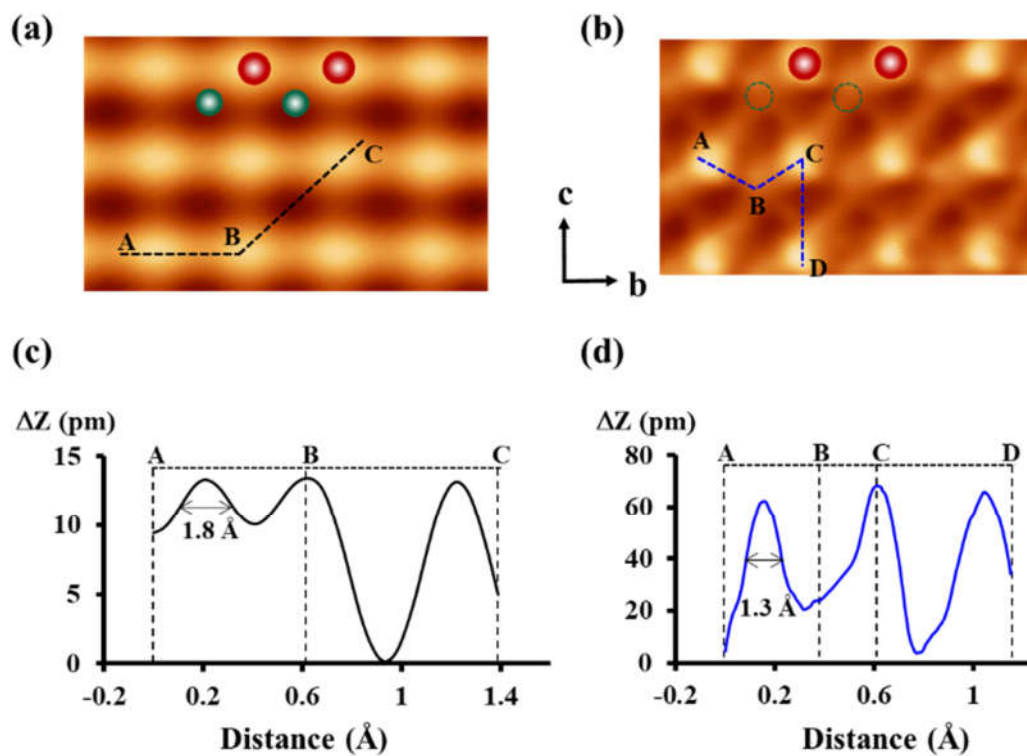


Figure A2. High-resolution images of SnSe surfaces with (a) Typical four-lobe d state tips and (b) d_{z^2} state tip. The line profiles along the dashed lines (ABC) and (ABCD) are shown in (c) and (d), respectively. The apparent radius of the Sn atoms is obtained from the FWHM (full width at half maximum) of the Gaussian fitting.

Appendix B – Magnetic properties of Fe_{5-x}GeTe₂

B1. Transition between a uniform state and a chiral soliton lattice state

In this section, we discuss a simple model that can qualitatively explain the anomalous cusp of the magnetization as a function of temperature just below 280 K shown in the insets of Fig. 4.8b. In two phases with $\sqrt{3} \times \sqrt{3}$ ordering referred to as “udd” and “duu” phases in the main text, the inversion symmetry is broken within each layer of Fe₅GeTe₂. Due to this inversion symmetry breaking, there should exist the two-dimensional Dzyaloshinskii-Moriya interaction (DMI) in the energy. By taking into account of the Heisenberg exchange energy, the DMI, and the Zeeman coupling, we model the system with the following energy:

$$U = \int dx dy \left[\frac{A(T)(\nabla \mathbf{m})^2}{2} + D(T)(m_z \nabla \mathbf{m} \cdot \mathbf{m} \nabla m_z) + M(T) \mathbf{H} \cdot \mathbf{m} \right] \quad (\text{Equation B1})$$

where $\mathbf{m}(x, y)$ is the unit vector in the direction of the local magnetization, $A(T)$ is the exchange coefficient varying with temperature T , $D(T)$ is the DMI coefficient, $M(T)$ is the magnetization, and \mathbf{H} is an external magnetic field. We consider the situation where the magnetization varies along only one direction (see, e.g., Fig. 4.8f-g for MFM images of the sample where the change of the magnetization occurs along one direction). Without loss of generality, we denote the direction of the magnetization change by the x axis. Then, it suffices to consider the following energy line density: $\mathcal{U} = \int dx \left[\frac{A(T)(\partial_x \mathbf{m})^2}{2} + D(T)(m_z \partial_x m_x - m_x \partial_x m_z) + M(T) \mathbf{H} \cdot \mathbf{m} \right]$. For the simplicity, the magnetic field is assumed in the z direction: $\mathbf{H} = H \mathbf{z}$. By factoring out the exchange coefficient, the expression can be rearranged as follows: $\mathcal{U} = A(T) \int dx \left[\frac{(\partial_x \mathbf{m})^2}{2} + \alpha(T)(m_z \partial_x m_x - m_x \partial_x m_z) + \beta(T) m_z \right]$, where $\alpha(T) = D(T)/A(T)$ and $\beta(T) = M(T)H/A(T)$ are the

rescaled DMI coefficient and the Zeeman coupling. For the analysis of the energy line density, we will closely follow the analysis done in ref.^[116,227] for chiral soliton lattices. It is known that, in the absence of the magnetic field $\beta(T) = 0$, a ground state of Equation B1 is given by a helical structure $\mathbf{m}(x) = (\cos(qx), 0, \sin(qx))$ with the wavevector $q = \alpha(T)$ (see, e.g.,^[228]). Note that $m_y = 0$ in this ground state. By following the aforementioned references, we assume that the magnetization stays in the xz -plane and represent the energy line density in terms of the angle θ with $\mathbf{m} = (\sin \theta, 0, \cos \theta)$:

$$\mathcal{U} = A(T) \int dx \left[\frac{(\partial_x \theta)^2}{2} - \alpha(T) \partial_x \theta - \beta(T) \cos \theta \right] \quad (\text{Equation B2})$$

Equation B2 is identical to Equation 2.6 of ref.^[116] There are two types of stationary solutions. The first one is a uniform state, $\theta(x) \equiv 0$, which is also called the ferromagnetic phase or the commensurate phase. The second is called the chiral soliton lattice (also known as the helical phase) or the incommensurate phase, and the solution is implicitly given by $\sin\left(\frac{\theta(x)-\pi}{2}\right) = \text{sn}\left(\frac{\sqrt{\beta}x}{k} \middle| k\right)$, where k is determined by $\frac{E(k)}{k} = \frac{\pi\alpha}{4\sqrt{\beta}}$, $E(k)$ is the complete integral of the second kind, and $\text{sn}(x|k)$ is the Jacobi elliptic function. The exemplary magnetization configuration of the chiral soliton state obtained by the aforementioned solution is shown in Fig. B1. The transition between the uniform state and the chiral soliton lattice state occurs at $\pi\alpha(T) = 4\sqrt{\beta(T)}$. To study the thermal transition between the commensurate and the incommensurate phases, let us take the following temperature dependence for the coefficients by following:^[116] $A(T) = A(0) \left(\frac{M(T)}{M(0)}\right)^2$, $D(T) = D(0) \left(\frac{M(T)}{M(0)}\right)^2$, and $M(T) = M(0)\sqrt{1 - T/T_c}$, where T_c is the Curie temperature. The temperature dependence of the coefficients can be much more complicated than the mentioned ones in real materials, but, in this supplemental material, we focus on qualitative

understanding of the observed cusp, which, we believe, can be obtained with this simple modeling. Then, the rescaled coefficients have the following temperature dependence: $\alpha(T) = \alpha$ and $\beta(T) = \beta(0)\sqrt{T_c/(T_c - T)}$. Note that $\alpha = D(T)/A(T)$ has no temperature dependence. Then, the transition between the commensurate (uniform) phase and the incommensurate (chiral soliton lattice) phase occurs at temperature given by $T = \left[1 - \left(\frac{16\beta(0)}{\pi^2\alpha^2}\right)^2\right] T_c$. For temperatures $T < T < T_c$, the system is in the commensurate (uniform) phase. The resultant magnetization is in the z direction and it is given by $M_z(T) = M(0)\sqrt{1 - T/T_c}$. For temperatures $T < T$, the system is in the incommensurate (chiral soliton lattice) phase. The average magnetization (in the z axis) in this phase is given by $M_z(T) = M(0)\sqrt{1 - T/T_c} \left(1 + \frac{2}{k^2} \frac{2E(k)}{k^2K(k)}\right)$ where k is determined by $\frac{E(k)}{k} = \sqrt{\frac{M(T)}{M(T)}}$, and $K(k)$ is the complete elliptic integral of the first kind.^[116] For an illustrative example, we calculated the magnetization $M_z(T)/M(0)$ for $\alpha = 0.05$ and $\beta(0) = 0.0004$ and it is shown in Fig. B1a. The transition temperature is given by $T = 0.93 T_c$. Above T and below T_c , the ground state is a uniform state, where the magnetization is in the z direction parallel to the external field. Below T , the ground state is a chiral soliton lattice state, where the magnetization changes in one direction. Fig. B1b shows the magnetization profile for $T = 0.92 T_c < T$. Note that the magnetization changes vertically forming the lattice of solitons.

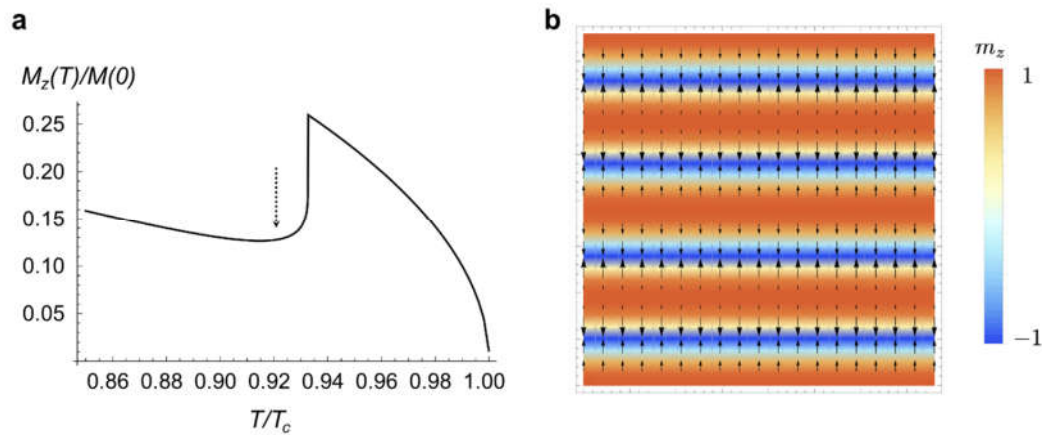


Figure B1. a) The spatial average of the z component of the magnetization $M_z(T)$ along the external magnetic field with the parameters $\alpha = 0.05$ and $\beta(0) = 0.0004$. The transition temperature is given by $T = 0.93 T_c$. The ground state is given by a commensurate (uniform) state and an incommensurate (chiral soliton lattice) state above and below T , respectively. b) The magnetization direction $\mathbf{m}(x, y)$ for temperature $T = 0.92 T_c$ (denoted by the dashed arrow in (a)) in the chiral soliton lattice phase. The color encodes the z-component of the magnetization m_z and the vector represents the xy-components of the magnetization (m_x, m_y) .

B2. Determination of the exchange stiffness constant A_{stiff}

The exchange stiffness constant A_{stiff} can be obtained from M - T curve of the forced ferromagnetic state. In low temperature region, the spin-wave stiffness constant D_{spin} is estimated from the Bloch $T^{2/3}$ law;^[115,229]

$$\frac{M_s(T)}{M_s(0)} = 1 - BT^{3/2} \quad (\text{Equation B3})$$

Here,

$$B = 2.612 \frac{g\mu_B}{M_s(0)} \left(\frac{k_B}{4\pi D_{\text{spin}}} \right)^{3/2} \quad (\text{Equation B4})$$

where, $M_s(0)$ is saturation magnetization at 0 K. g is the g -factor. μ_B represents the Bohr magneton. k_B is the Boltzmann constant. According to Equation B1, we fitted our data (Fig. 4.8e) in main text), and the obtained D_{spin} is $1.87 \times 10^{-22} \text{ Jnm}^2$. Then, the constant A_{stiff} at 0 K, $A_{\text{stiff}}(0)$ can be calculated using relation $A_{\text{stiff}}(0) = D_{\text{spin}} \times M_s(0) / g\mu_B$.^[115] The value of $A_{\text{stiff}}(0)$ is 1.856 pJ/m. Finally, the temperature-dependent $A_{\text{stiff}}(T)$ is calculated using simplified relation^[115] as

$$\frac{A_{\text{stiff}}(T)}{A_{\text{stiff}}(0)} = \left[\frac{M_s(T)}{M_s(0)} \right]^2 \quad (\text{Equation B5})$$

At 140 K and 77 K, the estimated values of $A_{\text{stiff}}(T)$ with saturation magnetization M_s in Fig. 4.8e are 1.201 pJ/m and 1.572 pJ/m respectively.

B3. Determination of the DMI based on MFM image

The DMI strength $|D|$ can be estimated by the domain wall energy δ_w as follows: ^[109,230]

$$\delta_w = 4\sqrt{A_{stiff}K_{eff}} \quad \pi|D| \quad (\text{Equation B6})$$

$$K_{eff} = \frac{1}{2}\mu_0 M_s H_{sat} \quad (\text{Equation B7})$$

where, A_{stiff} is the exchange stiffness constant. K_{eff} is effective anisotropy constant. H_{sat} is saturation field. M_s is saturation magnetization. μ_0 is the permeability of free space. Here, the domain wall energy δ_w is also related to domain width w :^[231]

$$\delta_w = \frac{M_s^2}{\beta 4\pi w} \quad (\text{Equation B8})$$

Here, β is phenomenological fitting parameter determined by the magnet quality factor Q ^[232] and $\beta = 0.31 \pm 0.02$ for $Q \gg 1$. Because Q is about 4 in our system, we fixed $\beta = 0.31$ to calculate the domain width. According to ref.,^[233] the surface magnetic domain width w can be described by arbitrary structure magnetic patterns. And w is defined as,^[231]

$$w = \frac{2 \times \text{total test line length}}{\pi \times \text{number of interaction}} \quad (\text{Equation B9})$$

Then, we can obtain the magnetic domain width w by evaluating the periodicity of the magnetic patterns with the line profile (red line) of a wide range MFM image as shown in Fig. B2. From this method, the estimated domain width of $\text{Fe}_{5-x}\text{GeTe}_2$ is $4/\pi \mu\text{m}$ at 140 K. Finally, the strength D is obtained with parameters $A_{stiff}(140 \text{ K}) = 1.201 \text{ pJ/m}$, $K_{eff} = 7.5 \times 10^{-2} \text{ J/m}^3$, $w = 4/\pi \mu\text{m}$, and $\beta = 0.31$ The estimated D is $3.63 \times 10^{-4} \text{ J/m}^2$ at 140 K.

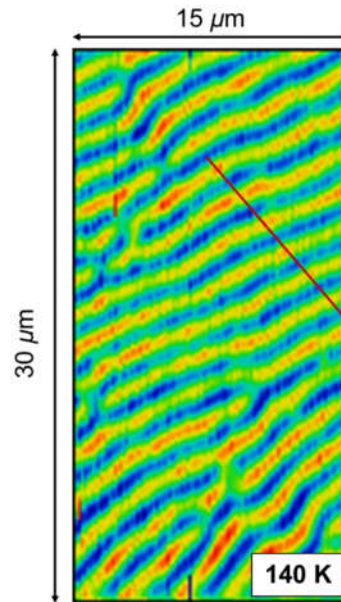


Figure B2. The MFM image used to obtain the domain size.

B4. The ratio of the DMI and exchange energy

As mentioned in previous section, the transition between the uniform state and the chiral soliton lattice state occurs at $\pi\alpha(T) = 4\sqrt{\beta(T)}$. The α means the ratio between the DMI $D(T)$ and exchange coefficient $A(T)$. When $D(T)$ is zero indicating the absence of DMI, the magnetic anomaly is not observed just below T_c .^[227] Therefore, $\alpha = D(T)/A(T)$ is a crucial parameter. With the experimental values, we estimate the ratio $D(T)/A(T)$ by following relation.^[126]

$$\frac{D}{J_{ex}} = \frac{2\sqrt{2}a}{3} \frac{D}{A_{stiff}} \quad (\text{Equation B10})$$

where a is lattice constant. J_{ex} is exchange constant meaning exchange coefficient $A(T)$, and A_{stiff} is exchange stiffness constant. Therefore, the ratio α of our $\text{Fe}_{5-x}\text{GeTe}_2$ can be obtained with $D(140 \text{ K}) = 3.63 \times 10^{-4} \text{ J/m}^2$, $A_{stiff}(140 \text{ K}) = 1.201 \text{ pJ/m}$, and $a = 4 \text{ \AA}$. The estimated

value of the ratio α is approximately 0.1. This value is in the range (0.2 ~ 0.01) generating chiral soliton lattice state. [116,227,234]

Appendix C – Tip and sample preparation

C1. Tip making system

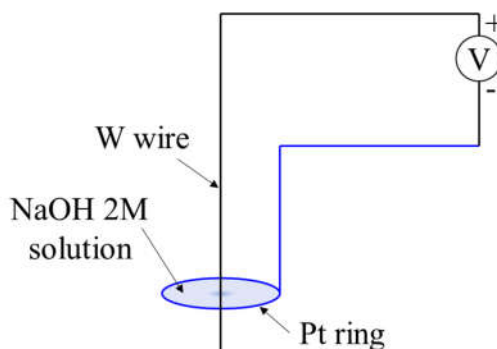


Figure C1: The schematics of tip etching configuration

All tips using for all STM experiments are made of tungsten (W) wires using electrochemical etching. As shown in Fig. C1, the W wire is dipped into a thin layer of NaOH 2M solution hold by platinum (Pt) ring and the voltage bias is applied between Pt ring (anode) and W wire (cathode). There are two processes of tip etching; bias voltage of 20 V is applied in fast etching while 2~5 V is applied in slow etching. After around 30 minutes, the bottom part is dropped and used as a STM tip. In my experience, the thinner NaOH layer results in the shaper STM tip.

C2. Tip and sample annealing stages

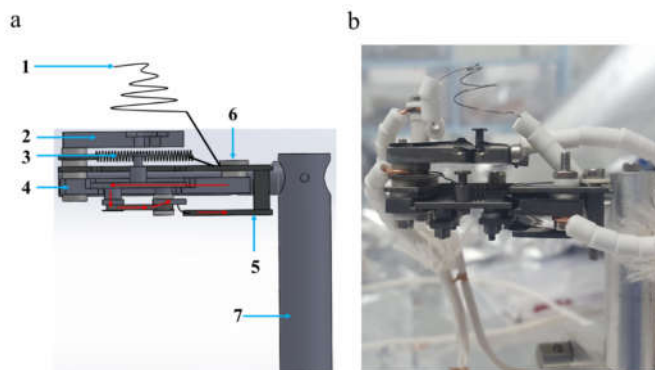


Figure C2: A combination of tip and sample annealing stages. (a) The electronic schematics of annealing stages for tip and sample. (b) A picture of tip and sample annealing stages. (1). Tip filament, (2). Tip stage, (3). Sample filament, (4). Sample stage, (5). Ground stage.

To save space under UHV conditions and lower making cost, a combination of tip and sample annealing stages was designed, as showing in Fig. C2. The tungsten (W) tip is cleaned by electron beam (e-beam) method before using. For this purpose, a current source of 2 A to 5 A is applied to the tip filament (1) while a high bias voltage (0.5 kV to 1 kV) is applied to tip stage (2). For the sample annealing purposes, three modes are available which are using e-beam, radiation, or Joule heating. The sample filament (3) is mounted close to the sample stage (4). In the e-beam mode, the temperature can increase faster than that of radiation mode. In Joule heating mode, the sample is mounted in special way to be grounded (5) and current source is flowing through the sample (red arrows). All electrodes (1), (2), (3), (4), and (5) are isolated by ceramic washers (6). Both tip and sample annealing stages are mounted into the standing aluminum rod (7).

Bibliography

- [1] F. Zhu, W. Chen, Y. Xu, C. Gao, D. Guan, C. Liu, D. Qian, S.-C. Zhang, J. Jia, *Nat. Mater.* **2015**, *14*, 1020.
- [2] S. Raaen, O.-M. Nes, *Solid State Commun.* **1988**, *65*, 1605.
- [3] S. Zhou, R. Wang, J. Han, D. Wang, H. Li, L. Gan, T. Zhai, *Adv. Funct. Mater.* **2019**, *29*, 1805880.
- [4] Y. Du, Z. Yin, J. Zhu, X. Huang, X.-J. Wu, Z. Zeng, Q. Yan, H. Zhang, *Nat. Commun.* **2012**, *3*, 1177.
- [5] C. Schliehe, B. H. Juarez, M. Pelletier, S. Jander, D. Greshnykh, M. Nagel, A. Meyer, S. Foerster, A. Kornowski, C. Klinke, H. Weller, *Science (80-.)*. **2010**, *329*, 550 LP.
- [6] Z. Sun, T. Liao, Y. Dou, S. M. Hwang, M.-S. Park, L. Jiang, J. H. Kim, S. X. Dou, *Nat. Commun.* **2014**, *5*, 3813.
- [7] N. Zhou, R. Yang, T. Zhai, *Mater. Today Nano* **2019**, *8*, 100051.
- [8] H. Liu, A. T. Neal, Z. Zhu, Z. Luo, X. Xu, D. Tománek, P. D. Ye, *ACS Nano* **2014**, *8*, 4033.
- [9] K. S. Novoselov, A. K. Geim, S. V Morozov, D. Jiang, Y. Zhang, S. V Dubonos, I. V Grigorieva, A. A. Firsov, *Science (80-.)*. **2004**, *306*, 666 LP.
- [10] L. Li, Z. Chen, Y. Hu, X. Wang, T. Zhang, W. Chen, Q. Wang, *J. Am. Chem. Soc.* **2013**, *135*, 1213.
- [11] J. D. Dwyer, E. J. Diaz, T. E. Webber, A. Katzenberg, M. A. Modestino, E. S. Aydil, *Nanotechnology* **2019**, *30*, 245705.
- [12] S. Lei, L. Ge, Z. Liu, S. Najmaei, G. Shi, G. You, J. Lou, R. Vajtai, P. M. Ajayan, *Nano Lett.* **2013**, *13*, 2777.
- [13] H. L. Zhuang, R. G. Hennig, *Chem. Mater.* **2013**, *25*, 3232.

- [14] A. V Matetskiy, I. A. Kibirev, A. N. Mihalyuk, S. V Eremeev, A. V Zotov, A. A. Saranin, *Appl. Surf. Sci.* **2021**, 539, 148144.
- [15] K. M. McCreary, A. T. Hanbicki, J. T. Robinson, E. Cobas, J. C. Culbertson, A. L. Friedman, G. G. Jernigan, B. T. Jonker, *Adv. Funct. Mater.* **2014**, 24, 6449.
- [16] S. S. Grønberg, S. Ulstrup, M. Bianchi, M. Dendzik, C. E. Sanders, J. V Lauritsen, P. Hofmann, J. A. Miwa, *Langmuir* **2015**, 31, 9700.
- [17] G. W. Shim, K. Yoo, S.-B. Seo, J. Shin, D. Y. Jung, I.-S. Kang, C. W. Ahn, B. J. Cho, S.-Y. Choi, *ACS Nano* **2014**, 8, 6655.
- [18] X. Lu, M. I. B. Utama, J. Lin, X. Gong, J. Zhang, Y. Zhao, S. T. Pantelides, J. Wang, Z. Dong, Z. Liu, W. Zhou, Q. Xiong, *Nano Lett.* **2014**, 14, 2419.
- [19] Z. Zhang, J. Niu, P. Yang, Y. Gong, Q. Ji, J. Shi, Q. Fang, S. Jiang, H. Li, X. Zhou, L. Gu, X. Wu, Y. Zhang, *Adv. Mater.* **2017**, 29, 1702359.
- [20] L. Xing, X. Yan, J. Zheng, G. Xu, Z. Lu, L. Liu, J. Wang, P. Wang, X. Pan, L. Jiao, *InfoMat* **2019**, 1, 552.
- [21] Y. Guo, L. Kang, P. Song, Q. Zeng, B. Tang, J. Yang, Y. Wu, D. Tian, M. Xu, W. Zhao, X. Qi, Z. Zhang, Z. Liu, *2D Mater.* **2021**, 8, 35036.
- [22] M. Grönke, P. Schmidt, M. Valldor, S. Oswald, D. Wolf, A. Lubk, B. Büchner, S. Hampel, *Nanoscale* **2018**, 10, 19014.
- [23] M. A. McGuire, G. Clark, S. KC, W. M. Chance, G. E. Jellison, V. R. Cooper, X. Xu, B. C. Sales, *Phys. Rev. Mater.* **2017**, 1, 14001.
- [24] X. Cai, T. Song, N. P. Wilson, G. Clark, M. He, X. Zhang, T. Taniguchi, K. Watanabe, W. Yao, D. Xiao, M. A. McGuire, D. H. Cobden, X. Xu, *Nano Lett.* **2019**, 19, 3993.
- [25] D. Ghazaryan, M. T. Greenaway, Z. Wang, V. H. Guarochico-Moreira, I. J. Vera-Marun, J. Yin, Y. Liao, S. V Morozov, O. Kristanovski, A. I. Lichtenstein, M. I. Katsnelson, F. Withers, A. Mishchenko, L. Eaves, A. K. Geim, K. S. Novoselov, A. Misra, *Nat. Electron.* **2018**, 1, 344.

- [26] Z. Zhang, J. Shang, C. Jiang, A. Rasmita, W. Gao, T. Yu, *Nano Lett.* **2019**, *19*, 3138.
- [27] S. Jiang, L. Li, Z. Wang, K. F. Mak, J. Shan, *Nat. Nanotechnol.* **2018**, *13*, 549.
- [28] R. Ai, X. Guan, J. Li, K. Yao, P. Chen, Z. Zhang, X. Duan, X. Duan, *ACS Nano* **2017**, *11*, 3413.
- [29] D. L. Duong, S. J. Yun, Y. H. Lee, *ACS Nano* **2017**, *11*, 11803.
- [30] M.-W. Lin, H. L. Zhuang, J. Yan, T. Z. Ward, A. A. Puretzky, C. M. Rouleau, Z. Gai, L. Liang, V. Meunier, B. G. Sumpter, P. Ganesh, P. R. C. Kent, D. B. Geohegan, D. G. Mandrus, K. Xiao, *J. Mater. Chem. C* **2016**, *4*, 315.
- [31] S. Liu, X. Yuan, Y. Zou, Y. Sheng, C. Huang, E. Zhang, J. Ling, Y. Liu, W. Wang, C. Zhang, J. Zou, K. Wang, F. Xiu, *npj 2D Mater. Appl.* **2017**, *1*, 30.
- [32] P. R. Jothi, J. P. Scheifers, Y. Zhang, M. Alghamdi, D. Stekovic, M. E. Itkis, J. Shi, B. P. T. Fokwa, *Phys. status solidi – Rapid Res. Lett.* **2020**, *14*, 1900666.
- [33] J. Yu, J. Li, W. Zhang, H. Chang, *Chem. Sci.* **2015**, *6*, 6705.
- [34] A. Reina, X. Jia, J. Ho, D. Nezich, H. Son, V. Bulovic, M. S. Dresselhaus, J. Kong, *Nano Lett.* **2009**, *9*, 30.
- [35] X. Li, W. Cai, J. An, S. Kim, J. Nah, D. Yang, R. Piner, A. Velamakanni, I. Jung, E. Tutuc, S. K. Banerjee, L. Colombo, R. S. Ruoff, *Science (80-.)*. **2009**, *324*, 1312 LP.
- [36] Y.-H. Lee, X.-Q. Zhang, W. Zhang, M.-T. Chang, C.-T. Lin, K.-D. Chang, Y.-C. Yu, J. T.-W. Wang, C.-S. Chang, L.-J. Li, T.-W. Lin, *Adv. Mater.* **2012**, *24*, 2320.
- [37] C. Muratore, A. A. Voevodin, N. R. Glavin, *Thin Solid Films* **2019**, *688*, 137500.
- [38] K. S. Novoselov, A. K. Geim, S. V Morozov, D. Jiang, M. I. Katsnelson, I. V Grigorieva, S. V Dubonos, A. A. Firsov, *Nature* **2005**, *438*, 197.
- [39] M. Yi, Z. Shen, *J. Mater. Chem. A* **2015**, *3*, 11700.

- [40] H. Li, J. Wu, Z. Yin, H. Zhang, *Acc. Chem. Res.* **2014**, *47*, 1067.
- [41] V. Nicolosi, M. Chhowalla, M. G. Kanatzidis, M. S. Strano, J. N. Coleman, *Science (80-.)*. **2013**, *340*, 1226419.
- [42] Y. Hernandez, V. Nicolosi, M. Lotya, F. M. Blighe, Z. Sun, S. De, I. T. McGovern, B. Holland, M. Byrne, Y. K. Gun'Ko, J. J. Boland, P. Niraj, G. Duesberg, S. Krishnamurthy, R. Goodhue, J. Hutchison, V. Scardaci, A. C. Ferrari, J. N. Coleman, *Nat. Nanotechnol.* **2008**, *3*, 563.
- [43] J. N. Coleman, M. Lotya, A. O'Neill, S. D. Bergin, P. J. King, U. Khan, K. Young, A. Gaucher, S. De, R. J. Smith, I. V Shvets, S. K. Arora, G. Stanton, H.-Y. Kim, K. Lee, G. T. Kim, G. S. Duesberg, T. Hallam, J. J. Boland, J. J. Wang, J. F. Donegan, J. C. Grunlan, G. Moriarty, A. Shmeliov, R. J. Nicholls, J. M. Perkins, E. M. Grieveson, K. Theuwissen, D. W. McComb, P. D. Nellist, V. Nicolosi, *Science (80-.)*. **2011**, *331*, 568 LP.
- [44] U. Khan, P. May, A. O'Neill, A. P. Bell, E. Boussac, A. Martin, J. Semple, J. N. Coleman, *Nanoscale* **2013**, *5*, 581.
- [45] D. Hanlon, C. Backes, T. M. Higgins, M. Hughes, A. O'Neill, P. King, N. McEvoy, G. S. Duesberg, B. Mendoza Sanchez, H. Pettersson, V. Nicolosi, J. N. Coleman, *Chem. Mater.* **2014**, *26*, 1751.
- [46] J. R. Brent, N. Savjani, E. A. Lewis, S. J. Haigh, D. J. Lewis, P. O'Brien, *Chem. Commun.* **2014**, *50*, 13338.
- [47] L. Niu, J. N. Coleman, H. Zhang, H. Shin, M. Chhowalla, Z. Zheng, *Small* **2016**, *12*, 272.
- [48] M. B. Dines, *Mater. Res. Bull.* **1975**, *10*, 287.
- [49] P. Joensen, R. F. Frindt, S. R. Morrison, *Mater. Res. Bull.* **1986**, *21*, 457.
- [50] L. M. Viculis, J. J. Mack, O. M. Mayer, H. T. Hahn, R. B. Kaner, *J. Mater. Chem.* **2005**, *15*, 974.
- [51] Z. Zeng, T. Sun, J. Zhu, X. Huang, Z. Yin, G. Lu, Z. Fan, Q. Yan, H. H. Hng, H.

- Zhang, *Angew. Chemie Int. Ed.* **2012**, *51*, 9052.
- [52] Z. Zeng, C. Tan, X. Huang, S. Bao, H. Zhang, *Energy Environ. Sci.* **2014**, *7*, 797.
- [53] J. Zheng, H. Zhang, S. Dong, Y. Liu, C. Tai Nai, H. Suk Shin, H. Young Jeong, B. Liu, K. Ping Loh, *Nat. Commun.* **2014**, *5*, 2995.
- [54] K. Parvez, Z.-S. Wu, R. Li, X. Liu, R. Graf, X. Feng, K. Müllen, *J. Am. Chem. Soc.* **2014**, *136*, 6083.
- [55] Z. Liu, R. Ma, M. Osada, N. Iyi, Y. Ebina, K. Takada, T. Sasaki, *J. Am. Chem. Soc.* **2006**, *128*, 4872.
- [56] R. Ma, Z. Liu, K. Takada, N. Iyi, Y. Bando, T. Sasaki, *J. Am. Chem. Soc.* **2007**, *129*, 5257.
- [57] J. Liang, R. Ma, N. Iyi, Y. Ebina, K. Takada, T. Sasaki, *Chem. Mater.* **2010**, *22*, 371.
- [58] R. Ma, K. Takada, K. Fukuda, N. Iyi, Y. Bando, T. Sasaki, *Angew. Chemie Int. Ed.* **2008**, *47*, 86.
- [59] W. S. Hummers Jr, R. E. Offeman, *J. Am. Chem. Soc.* **1958**, *80*, 1339.
- [60] S. Stankovich, D. A. Dikin, R. D. Piner, K. A. Kohlhaas, A. Kleinhammes, Y. Jia, Y. Wu, S. T. Nguyen, R. S. Ruoff, *Carbon N. Y.* **2007**, *45*, 1558.
- [61] Y. Zhu, S. Murali, W. Cai, X. Li, J. W. Suk, J. R. Potts, R. S. Ruoff, *Adv. Mater.* **2010**, *22*, 3906.
- [62] D. Li, M. B. Müller, S. Gilje, R. B. Kaner, G. G. Wallace, *Nat. Nanotechnol.* **2008**, *3*, 101.
- [63] X. Zhou, X. Huang, X. Qi, S. Wu, C. Xue, F. Y. C. Boey, Q. Yan, P. Chen, H. Zhang, *J. Phys. Chem. C* **2009**, *113*, 10842.
- [64] A. K. Geim, K. S. Novoselov, *Nat. Mater.* **2007**, *6*, 183.
- [65] G. Fiori, F. Bonaccorso, G. Iannaccone, T. Palacios, D. Neumaier, A. Seabaugh, S.

- K. Banerjee, L. Colombo, *Nat. Nanotechnol.* **2014**, *9*, 768.
- [66] C. Gong, X. Zhang, Two-dimensional magnetic crystals and emergent heterostructure devices. *Science (80-.)*. **2019**, 363.
- [67] C. J. Chen, *Introduction to scanning tunneling microscopy*; Oxford University Press on Demand, 1993; Vol. 4.
- [68] J. Kim, H. Nam, S. Qin, S. Kim, A. Schroeder, D. Eom, C.-K. Shih, *Rev. Sci. Instrum.* **2015**, *86*, 093707.
- [69] J. Kim, Low temperature scanning tunneling microscope study of low-dimensional superconductivity on metallic nanostructures, 2010.
- [70] M. C. Asensio, M. Batzill, *J. Phys. Condens. Matter* **2016**, *28*, 490301.
- [71] L.-D. Zhao, S.-H. Lo, Y. Zhang, H. Sun, G. Tan, C. Uher, C. Wolverton, V. P. Dravid, M. G. Kanatzidis, *Nature* **2014**, *508*, 373.
- [72] L.-D. Zhao, G. Tan, S. Hao, J. He, Y. Pei, H. Chi, H. Wang, S. Gong, H. Xu, V. P. Dravid, C. Uher, G. J. Snyder, C. Wolverton, M. G. Kanatzidis, *Science (80-.)*. **2015**.
- [73] T.-R. Wei, G. Tan, X. Zhang, C.-F. Wu, J.-F. Li, V. P. Dravid, G. J. Snyder, M. G. Kanatzidis, *J. Am. Chem. Soc.* **2016**, *138*, 8875.
- [74] A. T. Duong, V. Q. Nguyen, G. Duvjir, V. T. Duong, S. Kwon, J. Y. Song, J. K. Lee, J. E. Lee, S. Park, T. Min, J. Lee, J. Kim, S. Cho, *Nat. Commun.* **2016**, *7*, 13713.
- [75] S.-H. Cho, K. Cho, N.-W. Park, S. Park, J.-H. Koh, S.-K. Lee, *Nanoscale Res. Lett.* **2017**, *12*, 373.
- [76] Y.-M. Han, J. Zhao, M. Zhou, X.-X. Jiang, H.-Q. Leng, L.-F. Li, *J. Mater. Chem. A* **2015**, *3*, 4555.
- [77] Asfandiyar, T.-R. Wei, Z. Li, F.-H. Sun, Y. Pan, C.-F. Wu, M. U. Farooq, H. Tang, F. Li, B. Li, J.-F. Li, *Sci. Rep.* **2017**, *7*, 43262.

- [78] E. S. Toberer, A. Zevalkink, G. J. Snyder, *J. Mater. Chem.* **2011**, *21*, 15843.
- [79] H. Geng, H. Zhang, *J. Appl. Phys.* **2014**, *116*, 33708.
- [80] A. Banik, B. Vishal, S. Perumal, R. Datta, K. Biswas, *Energy Environ. Sci.* **2016**, *9*, 2011.
- [81] J. H. Kim, S. Oh, Y. M. Kim, H. S. So, H. Lee, J.-S. Rhyee, S.-D. Park, S.-J. Kim, *J. Alloys Compd.* **2016**, *682*, 785.
- [82] H. Wang, A. D. LaLonde, Y. Pei, G. J. Snyder, *Adv. Funct. Mater.* **2013**, *23*, 1586.
- [83] G. Duvjir, T. Min, T. Thi Ly, T. Kim, A. T. Duong, S. Cho, S. H. Rhim, J. Lee, J. Kim, *Appl. Phys. Lett.* **2017**, *110*, 262106.
- [84] T. T. Ly, G. Duvjir, T. Min, J. Byun, T. Kim, M. M. Saad, N. T. M. Hai, S. Cho, J. Lee, J. Kim, *Phys. Chem. Chem. Phys.* **2017**, *19*, 21648.
- [85] S. Kim, A.-T. Duong, S. Cho, S. H. Rhim, J. Kim, *Surf. Sci.* **2016**, *651*, 5.
- [86] X. He, H. Shen, W. Wang, Z. Wang, B. Zhang, X. Li, *J. Alloys Compd.* **2013**, *556*, 86.
- [87] Z. Gai, W. Lin, J. D. Burton, K. Fuchigami, P. C. Snijders, T. Z. Ward, E. Y. Tsymbal, J. Shen, S. Jesse, S. V Kalinin, A. P. Baddorf, *Nat. Commun.* **2014**, *5*, 4528.
- [88] A. K. Geim, K. S. Novoselov, *J* **2007**, *6*, 183.
- [89] B. Radisavljevic, A. Radenovic, J. Brivio, V. Giacometti, A. Kis, *Nat. Nanotechnol.* **2011**, *6*, 147.
- [90] Y. Liu, N. O. Weiss, X. Duan, H.-C. Cheng, Y. Huang, X. Duan, *Nat. Rev. Mater.* **2016**, *1*, 16042.
- [91] K. S. Novoselov, A. Mishchenko, A. Carvalho, A. H. Castro Neto, *Science (80-.)*. **2016**, *353*, aac9439.
- [92] B. Huang, G. Clark, E. Navarro-Moratalla, D. R. Klein, R. Cheng, K. L. Seyler, D.

- Zhong, E. Schmidgall, M. A. McGuire, D. H. Cobden, W. Yao, D. Xiao, P. Jarillo-Herrero, X. Xu, *Nature* **2017**, *546*, 270.
- [93] C. Gong, L. Li, Z. Li, H. Ji, A. Stern, Y. Xia, T. Cao, W. Bao, C. Wang, Y. Wang, Z. Q. Qiu, R. J. Cava, S. G. Louie, J. Xia, X. Zhang, *Nature* **2017**, *546*, 265.
- [94] C. Gong, X. Zhang, *Science (80-.)*. **2019**, *363*, eaav4450.
- [95] M. Gibertini, M. Koperski, A. F. Morpurgo, K. S. Novoselov, *Nat. Nanotechnol.* **2019**, *14*, 408.
- [96] B. Huang, M. A. McGuire, A. F. May, D. Xiao, P. Jarillo-Herrero, X. Xu, *Nat. Mater.* **2020**, *19*, 1276.
- [97] Y. Deng, Y. Yu, Y. Song, J. Zhang, N. Z. Wang, Z. Sun, Y. Yi, Y. Z. Wu, S. Wu, J. Zhu, J. Wang, X. H. Chen, Y. Zhang, *Nature* **2018**, *563*, 94.
- [98] B. Chen, J. Yang, H. Wang, M. Imai, H. Ohta, C. Michioka, K. Yoshimura, M. Fang, *J. Phys. Soc. Japan* **2013**, *82*, 124711.
- [99] A. F. May, S. Calder, C. Cantoni, H. Cao, M. A. McGuire, *Phys. Rev. B* **2016**, *93*, 14411.
- [100] A. F. May, D. Ovchinnikov, Q. Zheng, R. Hermann, S. Calder, B. Huang, Z. Fei, Y. Liu, X. Xu, M. A. McGuire, *ACS Nano* **2019**, *13*, 4436.
- [101] A. F. May, C. A. Bridges, M. A. McGuire, *Phys. Rev. Mater.* **2019**, *3*, 104401.
- [102] J. Seo, D. Y. Kim, E. S. An, K. Kim, G.-Y. Kim, S.-Y. Hwang, D. W. Kim, B. G. Jang, H. Kim, G. Eom, S. Y. Seo, R. Stania, M. Muntwiler, J. Lee, K. Watanabe, T. Taniguchi, Y. J. Jo, J. Lee, B. Il Min, M. H. Jo, H. W. Yeom, S.-Y. Choi, J. H. Shim, J. S. Kim, *Sci. Adv.* **2020**, *6*, eaay8912.
- [103] H. Zhang, R. Chen, K. Zhai, X. Chen, L. Caretta, X. Huang, R. V Chopdekar, J. Cao, J. Sun, J. Yao, R. Birgeneau, R. Ramesh, *Phys. Rev. B* **2020**, *102*, 64417.
- [104] Q. Li, M. Yang, C. Gong, R. V Chopdekar, A. T. N'Diaye, J. Turner, G. Chen, A. Scholl, P. Shafer, E. Arenholz, A. K. Schmid, S. Wang, K. Liu, N. Gao, A. S.

- Admasu, S.-W. Cheong, C. Hwang, J. Li, F. Wang, X. Zhang, Z. Qiu, *Nano Lett.* **2018**, *18*, 5974.
- [105] J. Stahl, E. Shlaen, D. Johrendt, *Zeitschrift für Anorg. und Allg. Chemie* **2018**, *644*, 1923.
- [106] M. Joe, U. Yang, C. Lee, *Nano Mater. Sci.* **2019**, *1*, 299.
- [107] A. Fert, N. Reyren, V. Cros, *Nat. Rev. Mater.* **2017**, *2*, 1.
- [108] K. M. Song, J.-S. Jeong, B. Pan, X. Zhang, J. Xia, S. Cha, T.-E. Park, K. Kim, S. Finizio, J. Raabe, J. Chang, Y. Zhou, W. Zhao, W. Kang, H. Ju, S. Woo, *Nat. Electron.* **2020**, *3*, 148.
- [109] S. Woo, K. Litzius, B. Krüger, M.-Y. Im, L. Caretta, K. Richter, M. Mann, A. Krone, R. M. Reeve, M. Weigand, others, *Nat. Mater.* **2016**, *15*, 501.
- [110] T. Yokouchi, F. Kagawa, M. Hirschberger, Y. Otani, N. Nagaosa, Y. Tokura, *Nature* **2020**, *586*, 232.
- [111] G. D. Nguyen, J. Lee, T. Berlijn, Q. Zou, S. M. Hus, J. Park, Z. Gai, C. Lee, A.-P. Li, *Phys. Rev. B* **2018**, *97*, 14425.
- [112] H.-J. Deiseroth, K. Aleksandrov, C. Reiner, L. Kienle, R. K. Kremer, *Eur. J. Inorg. Chem.* **2006**, *2006*, 1561.
- [113] K.-W. Kim, H.-W. Lee, K.-J. Lee, M. D. Stiles, *Phys. Rev. Lett.* **2013**, *111*, 216601.
- [114] V. Kashid, T. Schena, B. Zimmermann, Y. Mokrousov, S. Blügel, V. Shah, H. G. Salunke, *Phys. Rev. B* **2014**, *90*, 54412.
- [115] S. Kim, K. Ueda, G. Go, P.-H. Jang, K.-J. Lee, A. Belabbes, A. Manchon, M. Suzuki, Y. Kotani, T. Nakamura, K. Nakamura, T. Koyama, D. Chiba, K. T. Yamada, D.-H. Kim, T. Moriyama, K.-J. Kim, T. Ono, *Nat. Commun.* **2018**, *9*, 1648.
- [116] J. Kishine, K. Inoue, Y. Yoshida, *Prog. Theor. Phys. Suppl.* **2005**, *159*, 82.
- [117] Y. Cao, Z. Huang, Y. Yin, H. Xie, B. Liu, W. Wang, C. Zhu, D. Mandrus, L. Wang,

- W. Huang, *Mater. Today Adv.* **2020**, 7, 100080.
- [118] Y. Togawa, T. Koyama, K. Takayanagi, S. Mori, Y. Kousaka, J. Akimitsu, S. Nishihara, K. Inoue, A. S. Ovchinnikov, J. Kishine, *Phys. Rev. Lett.* **2012**, 108, 107202.
- [119] Y. Kousaka, S. Yano, J. Kishine, Y. Yoshida, K. Inoue, K. Kikuchi, J. Akimitsu, *J. Phys. Soc. Japan* **2007**, 76, 123709.
- [120] U. Güngördü, R. Nepal, O. A. Tretiakov, K. Belashchenko, A. A. Kovalev, *Phys. Rev. B* **2016**, 93, 64428.
- [121] M. Haze, Y. Yoshida, Y. Hasegawa, *Sci. Rep.* **2017**, 7, 1.
- [122] J. Müller, *Magnetic Skyrmions and Topological Domain Walls*, Universität zu Köln, 2018.
- [123] Y. Kousaka, Y. Nakao, J. Kishine, M. Akita, K. Inoue, J. Akimitsu, *Nucl. Instruments Methods Phys. Res. Sect. A Accel. Spectrometers, Detect. Assoc. Equip.* **2009**, 600, 250.
- [124] N. J. Ghimire, M. A. McGuire, D. S. Parker, B. Sipos, S. Tang, J.-Q. Yan, B. C. Sales, D. Mandrus, *Phys. Rev. B* **2013**, 87, 104403.
- [125] A. Fernández-Pacheco, E. Vedmedenko, F. Ummelen, R. Mansell, D. Petit, R. P. Cowburn, *Nat. Mater.* **2019**, 18, 679.
- [126] H. T. Nembach, J. M. Shaw, M. Weiler, E. Jué, T. J. Silva, *Nat. Phys.* **2015**, 11, 825.
- [127] A. M. Vibhakar, D. D. Khalyavin, P. Manuel, J. Liu, A. A. Belik, R. D. Johnson, *Phys. Rev. Lett.* **2020**, 124, 127201.
- [128] S. Emori, E. Martinez, K.-J. Lee, H.-W. Lee, U. Bauer, S.-M. Ahn, P. Agrawal, D. C. Bono, G. S. D. Beach, *Phys. Rev. B* **2014**, 90, 184427.
- [129] S. Husain, N. Sisodia, A. K. Chaurasiya, A. Kumar, J. P. Singh, B. S. Yadav, S. Akansel, K. H. Chae, A. Barman, P. K. Muduli, P. Svedlindh, S. Chaudhary, *Sci. Rep.* **2019**, 9, 1085.

- [130] A. Soumyanarayanan, M. Raju, A. L. Gonzalez Oyarce, A. K. C. Tan, M.-Y. Im, A. P. Petrović, P. Ho, K. H. Khoo, M. Tran, C. K. Gan, F. Ernult, C. Panagopoulos, *Nat. Mater.* **2017**, *16*, 898.
- [131] A. Hrabec, N. A. Porter, A. Wells, M. J. Benitez, G. Burnell, S. McVitie, D. McGrouther, T. A. Moore, C. H. Marrows, *Phys. Rev. B* **2014**, *90*, 20402.
- [132] M. Belmeguenai, J.-P. Adam, Y. Roussigné, S. Eimer, T. Devolder, J.-V. Kim, S. M. Cherif, A. Stashkevich, A. Thiaville, *Phys. Rev. B* **2015**, *91*, 180405.
- [133] J. A. Wilson, A. D. Yoffe, *Adv. Phys.* **1969**, *18*, 193.
- [134] D. Zhang, J. Ha, H. Baek, Y.-H. Chan, F. D. Natterer, A. F. Myers, J. D. Schumacher, W. G. Cullen, A. V Davydov, Y. Kuk, M. Y. Chou, N. B. Zhitenev, J. A. Stroscio, *Phys. Rev. Mater.* **2017**, *1*, 24005.
- [135] M. M. Ugeda, A. J. Bradley, S.-F. Shi, F. H. da Jornada, Y. Zhang, D. Y. Qiu, W. Ruan, S.-K. Mo, Z. Hussain, Z.-X. Shen, F. Wang, S. G. Louie, M. F. Crommie, *Nat. Mater.* **2014**, *13*, 1091.
- [136] C.-S. Lian, C. Si, W. Duan, *Nano Lett.* **2018**, *18*, 2924.
- [137] K. Takita, K. Masuda, *J. Low Temp. Phys.* **1985**, *58*, 127.
- [138] Y. Liu, D. F. Shao, L. J. Li, W. J. Lu, X. D. Zhu, P. Tong, R. C. Xiao, L. S. Ling, C. Y. Xi, L. Pi, H. F. Tian, H. X. Yang, J. Q. Li, W. H. Song, X. B. Zhu, Y. P. Sun, *Phys. Rev. B* **2016**, *94*, 45131.
- [139] C.-S. Lian, C. Heil, X. Liu, C. Si, F. Giustino, W. Duan, *J. Phys. Chem. Lett.* **2019**, *10*, 4076.
- [140] X. Xi, L. Zhao, Z. Wang, H. Berger, L. Forró, J. Shan, K. F. Mak, *Nat. Nanotechnol.* **2015**, *10*, 765.
- [141] P. Chen, W. W. Pai, Y.-H. Chan, V. Madhavan, M. Y. Chou, S.-K. Mo, A.-V. Fedorov, T.-C. Chiang, *Phys. Rev. Lett.* **2018**, *121*, 196402.
- [142] M. D. Johannes, I. I. Mazin, *Phys. Rev. B* **2008**, *77*, 165135.

- [143] K. Rossnagel, *J. Phys. Condens. Matter* **2011**, *23*, 213001.
- [144] X. Zhu, Y. Cao, J. Zhang, E. W. Plummer, J. Guo, *Proc. Natl. Acad. Sci.* **2015**, *112*, 2367.
- [145] D. W. Shen, B. P. Xie, J. F. Zhao, L. X. Yang, L. Fang, J. Shi, R. H. He, D. H. Lu, H. H. Wen, D. L. Feng, *Phys. Rev. Lett.* **2007**, *99*, 216404.
- [146] G. Li, A. Luican, J. M. B. Lopes dos Santos, A. H. Castro Neto, A. Reina, J. Kong, E. Y. Andrei, *Nat. Phys.* **2010**, *6*, 109.
- [147] J. Dai, E. Calleja, J. Alldredge, X. Zhu, L. Li, W. Lu, Y. Sun, T. Wolf, H. Berger, K. McElroy, *Phys. Rev. B* **2014**, *89*, 165140.
- [148] M. Calandra, I. I. Mazin, F. Mauri, *Phys. Rev. B* **2009**, *80*, 241108.
- [149] S. Lebègue, O. Eriksson, *Phys. Rev. B* **2009**, *79*, 115409.
- [150] P. Darancet, A. J. Millis, C. A. Marianetti, *Phys. Rev. B* **2014**, *90*, 45134.
- [151] J.-P. Peng, J.-Q. Guan, H.-M. Zhang, C.-L. Song, L. Wang, K. He, Q.-K. Xue, X.-C. Ma, *Phys. Rev. B* **2015**, *91*, 121113.
- [152] M. M. Ugeda, A. J. Bradley, Y. Zhang, S. Onishi, Y. Chen, W. Ruan, C. Ojeda-Aristizabal, H. Ryu, M. T. Edmonds, H.-Z. Tsai, A. Riss, S.-K. Mo, D. Lee, A. Zettl, Z. Hussain, Z.-X. Shen, M. F. Crommie, *Nat. Phys.* **2016**, *12*, 92.
- [153] J. Yang, W. Wang, Y. Liu, H. Du, W. Ning, G. Zheng, C. Jin, Y. Han, N. Wang, Z. Yang, M. Tian, Y. Zhang, *Appl. Phys. Lett.* **2014**, *105*, 63109.
- [154] G. Duvjir, B. K. Choi, T. T. Ly, N. H. Lam, S.-H. Chun, K. Jang, A. Soon, Y. J. Chang, J. Kim, *Nanoscale* **2019**, *11*, 20096.
- [155] W. Yu, J. Li, T. S. Heng, Z. Wang, X. Zhao, X. Chi, W. Fu, I. Abdelwahab, J. Zhou, J. Dan, Z. Chen, Z. Li, J. Lu, S. J. Pennycook, Y. P. Feng, J. Ding, K. P. Loh, *Adv. Mater.* **2019**, *31*, 1903779.
- [156] Y. Ma, Y. Dai, M. Guo, C. Niu, Y. Zhu, B. Huang, *ACS Nano* **2012**, *6*, 1695.

- [157] H.-R. Fuh, C.-R. Chang, Y.-K. Wang, R. F. L. Evans, R. W. Chantrell, H.-T. Jeng, *Sci. Rep.* **2016**, *6*, 32625.
- [158] H.-R. Fuh, B. Yan, S.-C. Wu, C. Felser, C.-R. Chang, *New J. Phys.* **2016**, *18*, 113038.
- [159] M. Bonilla, S. Kolekar, Y. Ma, H. C. Diaz, V. Kalappattil, R. Das, T. Eggers, H. R. Gutierrez, M.-H. Phan, M. Batzill, *Nat. Nanotechnol.* **2018**, *13*, 289.
- [160] T. J. Kim, S. Ryee, M. J. Han, S. Choi, Sub-room temperature ferromagnetism and its nature in VSe₂ monolayer **2019**, <https://arxiv.org/abs/1907.04790>.
- [161] G. Duvjir, B. K. Choi, I. Jang, S. Ulstrup, S. Kang, T. Thi Ly, S. Kim, Y. H. Choi, C. Jozwiak, A. Bostwick, E. Rotenberg, J.-G. Park, R. Sankar, K.-S. Kim, J. Kim, Y. J. Chang, *Nano Lett.* **2018**, *18*, 5432.
- [162] P. M. Coelho, K. Nguyen Cong, M. Bonilla, S. Kolekar, M.-H. Phan, J. Avila, M. C. Asensio, I. I. Oleynik, M. Batzill, *J. Phys. Chem. C* **2019**, *123*, 14089.
- [163] M. Bayard, M. J. Sienko, *J. Solid State Chem.* **1976**, *19*, 325.
- [164] V. N. Strocov, M. Shi, M. Kobayashi, C. Monney, X. Wang, J. Krempasky, T. Schmitt, L. Patthey, H. Berger, P. Blaha, *Phys. Rev. Lett.* **2012**, *109*, 86401.
- [165] D. J. Eaglesham, R. L. Withers, D. M. Bird, *J. Phys. C Solid State Phys.* **1986**, *19*, 359.
- [166] B. Giambattista, C. G. Slough, W. W. McNairy, R. V Coleman, *Phys. Rev. B* **1990**, *41*, 10082.
- [167] P. K. J. Wong, W. Zhang, F. Bussolotti, X. Yin, T. S. Heng, L. Zhang, Y. L. Huang, G. Vinai, S. Krishnamurthi, D. W. Bukhvalov, Y. J. Zheng, R. Chua, A. T. N'Diaye, S. A. Morton, C.-Y. Yang, K.-H. Ou Yang, P. Torelli, W. Chen, K. E. J. Goh, J. Ding, M.-T. Lin, G. Brocks, M. P. de Jong, A. H. Castro Neto, A. T. S. Wee, *Adv. Mater.* **2019**, *31*, 1901185.
- [168] W. Zhang, C.-P. Chuu, J.-K. Huang, C.-H. Chen, M.-L. Tsai, Y.-H. Chang, C.-T. Liang, Y.-Z. Chen, Y.-L. Chueh, J.-H. He, M.-Y. Chou, L.-J. Li, *Sci. Rep.* **2014**, *4*,

3826.

- [169] T. Georgiou, R. Jalil, B. D. Belle, L. Britnell, R. V Gorbachev, S. V Morozov, Y.-J. Kim, A. Gholinia, S. J. Haigh, O. Makarovsky, L. Eaves, L. A. Ponomarenko, A. K. Geim, K. S. Novoselov, A. Mishchenko, *Nat. Nanotechnol.* **2013**, *8*, 100.
- [170] H.-L. Tang, M.-H. Chiu, C.-C. Tseng, S.-H. Yang, K.-J. Hou, S.-Y. Wei, J.-K. Huang, Y.-F. Lin, C.-H. Lien, L.-J. Li, *ACS Nano* **2017**, *11*, 12817.
- [171] S. Rehman, H. Kim, M. F. Khan, J.-H. Hur, J. Eom, D. Kim, *J. Alloys Compd.* **2021**, *855*, 157310.
- [172] D. J. Groenendijk, M. Buscema, G. A. Steele, S. Michaelis de Vasconcellos, R. Bratschitsch, H. S. J. van der Zant, A. Castellanos-Gomez, *Nano Lett.* **2014**, *14*, 5846.
- [173] D.-S. Tsai, K.-K. Liu, D.-H. Lien, M.-L. Tsai, C.-F. Kang, C.-A. Lin, L.-J. Li, J.-H. He, *ACS Nano* **2013**, *7*, 3905.
- [174] Y.-C. Lin, H.-P. Komsa, C.-H. Yeh, T. Björkman, Z.-Y. Liang, C.-H. Ho, Y.-S. Huang, P.-W. Chiu, A. V Krasheninnikov, K. Suenaga, *ACS Nano* **2015**, *9*, 11249.
- [175] A.-J. Cho, S. D. Namgung, H. Kim, J.-Y. Kwon, *APL Mater.* **2017**, *5*, 76101.
- [176] E. Zhang, Y. Jin, X. Yuan, W. Wang, C. Zhang, L. Tang, S. Liu, P. Zhou, W. Hu, F. Xiu, *Adv. Funct. Mater.* **2015**, *25*, 4076.
- [177] E. Elahi, M. F. Khan, S. Rehman, H. M. W. Khalil, M. A. Rehman, D. Kim, H. Kim, K. Khan, M. Shahzad, M. W. Iqbal, M. A. Basit, F. Khan, *Dalt. Trans.* **2020**, *49*, 10017.
- [178] M. F. Khan, S. Rehman, I. Akhtar, S. Aftab, H. M. S. Ajmal, W. Khan, D. Kim, J. Eom, *2D Mater.* **2019**, *7*, 15010.
- [179] S.-H. Jo, H.-Y. Park, D.-H. Kang, J. Shim, J. Jeon, S. Choi, M. Kim, Y. Park, J. Lee, Y. J. Song, S. Lee, J.-H. Park, *Adv. Mater.* **2016**, *28*, 6518.
- [180] M. H. Ali, D.-H. Kang, J.-H. Park, *Org. Electron.* **2018**, *53*, 14.

- [181] Z. Qiu, M. Trushin, H. Fang, I. Verzhbitskiy, S. Gao, E. Laksono, M. Yang, P. Lyu, J. Li, J. Su, M. Telychko, K. Watanabe, T. Taniguchi, J. Wu, A. H. C. Neto, L. Yang, G. Eda, S. Adam, J. Lu, *Sci. Adv.* **2019**, *5*, eaaw2347.
- [182] C. Xie, S. Jiang, X. Zou, Y. Sun, L. Zhao, M. Hong, S. Chen, Y. Huan, J. Shi, X. Zhou, others, *Nano Res.* **2019**, *12*, 149.
- [183] B. K. Choi, S. Ulstrup, S. M. Gunasekera, J. Kim, S. Y. Lim, L. Moreschini, J. S. Oh, S.-H. Chun, C. Jozwiak, A. Bostwick, E. Rotenberg, H. Cheong, I.-W. Lyo, M. Mucha-Kruczynski, Y. J. Chang, *ACS Nano* **2020**, *14*, 7880.
- [184] Q. Wang, Y. Shao, X. Shi, *J. Chem. Phys.* **2020**, *152*, 244701.
- [185] C. Gong, L. Colombo, R. M. Wallace, K. Cho, *Nano Lett.* **2014**, *14*, 1714.
- [186] H. Wang, C. Si, J. Zhou, Z. Sun, *J. Phys. Chem. C* **2017**, *121*, 25164.
- [187] Y. Liu, P. Stradins, S.-H. Wei, *Sci. Adv.* **2016**, *2*, e1600069.
- [188] H. V Phuc, N. N. Hieu, B. D. Hoi, C. V Nguyen, *Phys. Chem. Chem. Phys.* **2018**, *20*, 17899.
- [189] M. Hong, X. Zhou, N. Gao, S. Jiang, C. Xie, L. Zhao, Y. Gao, Z. Zhang, P. Yang, Y. Shi, Q. Zhang, Z. Liu, J. Zhao, Y. Zhang, *ACS Nano* **2018**, *12*, 10095.
- [190] T. T. Ly, T. Lee, S. Kim, Y.-J. Lee, G. Duvjir, K. Jang, K. Palotás, S.-Y. Jeong, A. Soon, J. Kim, *J. Phys. Chem. C* **2019**, *123*, 12716.
- [191] R. Plumadore, M. M. Al Ezzi, S. Adam, A. Luican-Mayer, *J. Appl. Phys.* **2020**, *128*, 44303.
- [192] T. Le Quang, K. Nogajewski, M. Potemski, M. T. Dau, M. Jamet, P. Mallet, J.-Y. Veullen, *2D Mater.* **2018**, *5*, 35034.
- [193] T. Le Quang, V. Cherkez, K. Nogajewski, M. Potemski, M. T. Dau, M. Jamet, P. Mallet, J.-Y. Veullen, *2D Mater.* **2017**, *4*, 35019.
- [194] X. Liu, I. Balla, H. Bergeron, G. P. Campbell, M. J. Bedzyk, M. C. Hersam, *ACS Nano* **2016**, *10*, 1067.

- [195] A. Kerelsky, A. Nipane, D. Edelberg, D. Wang, X. Zhou, A. Motmaendadgar, H. Gao, S. Xie, K. Kang, J. Park, J. Teherani, A. Pasupathy, *Nano Lett.* **2017**, *17*, 5962.
- [196] B. K. Meyer, A. Polity, D. Reppin, M. Becker, P. Hering, P. J. Klar, T. Sander, C. Reindl, J. Benz, M. Eickhoff, C. Heiliger, M. Heinemann, J. Bläsing, A. Krost, S. Shokovets, C. Müller, C. Ronning, *Phys. Status Solidi Basic Res.* **2012**, *249*, 1487.
- [197] A. O. Musa, T. Akomolafe, M. J. Carter, *Sol. Energy Mater. Sol. Cells* **1998**, *51*, 305.
- [198] M. Tadatsugu, N. Yuki, M. Toshihiro, *Appl. Phys. Express* **2013**, *6*, 44101.
- [199] M. Hara, *Chem. Commun.* **1998**, 357.
- [200] J. N. Nian, C. C. Hu, H. Teng, *Int. J. Hydrogen Energy* **2008**, *33*, 2897.
- [201] A. Paracchino, V. Laporte, K. Sivula, M. Grätzel, E. Thimsen, *Nat. Mater.* **2011**, *10*, 456.
- [202] S. Sun, X. Song, Y. Sun, D. Deng, Z. Yang, *Catal. Sci. Technol.* **2012**, *2*, 925.
- [203] Y. Kwon, A. Soon, H. Han, H. Lee, *J. Mater. Chem. A* **2015**, *3*, 156.
- [204] F. Yang, Y. Choi, P. Liu, J. Hrbek, J. A. Rodriguez, *J. Phys. Chem. C* **2010**, *114*, 17042.
- [205] E. Fortunato, V. Figueiredo, P. Barquinha, E. Elamurugu, R. Barros, G. Gonçalves, S. H. K. Park, C. S. Hwang, R. Martins, *Appl. Phys. Lett.* **2010**, *96*, 192102.
- [206] P. Biswas, S. D. Baek, S. H. Lee, J. W. Kim, J. H. Park, S. J. Lee, T. Il Lee, J. M. Myoung, *Appl. Phys. Lett.* **2016**, *109*, 171102.
- [207] S. Han, A. J. Flewitt, *Sci. Rep.* **2017**, *7*, 5766.
- [208] H. Raebiger, S. Lany, A. Zunger, *Phys. Rev. B - Condens. Matter Mater. Phys.* **2007**, *76*, 45209.
- [209] A. Soon, X. Y. Cui, B. Delley, S. H. Wei, C. Stampfl, *Phys. Rev. B - Condens. Matter Mater. Phys.* **2009**, *79*, 035205.

- [210] F. Jensen, F. Besenbacher, I. Stensgaard, *Surf. Sci.* **1992**, 269–270, 400.
- [211] T. Matsumoto, R. A. Bennett, P. Stone, T. Yamada, K. Domen, M. Bowker, *Surf. Sci.* **2001**, 471, 225.
- [212] F. Wiame, V. Maurice, P. Marcus, *Surf. Sci.* **2007**, 601, 1193.
- [213] A. J. Therrien, R. Zhang, F. R. Lucci, M. D. Marcinkowski, A. Hensley, J. S. McEwen, E. C. H. Sykes, *J. Phys. Chem. C* **2016**, 120, 10879.
- [214] F. Yang, Y. Choi, P. Liu, D. Stacchiola, J. Hrbek, J. A. Rodriguez, *J. Am. Chem. Soc.* **2011**, 133, 11474.
- [215] A. Önsten, M. Göthelid, U. O. Karlsson, *Surf. Sci.* **2009**, 603, 257.
- [216] A. Soon, M. Todorova, B. Delley, C. Stampfl, *Phys. Rev. B - Condens. Matter Mater. Phys.* **2006**, 73, 165424.
- [217] N. Nilius, H. Fedderwitz, B. Groß, C. Noguera, J. Goniakowski, *Phys. Chem. Chem. Phys.* **2016**, 18, 6729.
- [218] A. Soon, M. Todorova, B. Delley, C. Stampfl, *Phys. Rev. B - Condens. Matter Mater. Phys.* **2007**, 75, 125420.
- [219] L. Martin, H. Martinez, D. Poinot, B. Pecquenard, F. Le Cras, *J. Phys. Chem. C* **2013**, 117, 4421.
- [220] H. Sträter, H. Fedderwitz, B. Groß, N. Nilius, *J. Phys. Chem. C* **2015**, 119, 5975.
- [221] C. Möller, H. Fedderwitz, C. Noguera, J. Goniakowski, N. Nilius, *Phys. Chem. Chem. Phys.* **2018**, 20, 5636.
- [222] A. Önsten, J. Weissenrieder, D. Stoltz, S. Yu, M. Göthelid, U. O. Karlsson, *J. Phys. Chem. C* **2013**, 117, 19357.
- [223] C. Möller, N. Nilius, *J. Phys. Chem. C* **2017**, 121, 20877.
- [224] C. Möller, J. Barreto, F. Stavale, H. Tissot, S. Shaikhutdinov, H. J. Freund, N. Nilius, *J. Phys. Chem. C* **2018**, 122, 2195.

- [225] R. Zhang, L. Li, L. Frazer, K. B. Chang, K. R. Poeppelmeier, M. K. Y. Chan, J. R. Guest, *Phys. Chem. Chem. Phys.* **2018**, *20*, 27456.
- [226] H. Fedderwitz, *Preparation and Characterization of Cuprous Oxide Thin Films using Low-Temperature Scanning Tunneling Microscopy*.
- [227] J. Kishine, K. Inoue, K. Kikuchi, *J. Magn. Magn. Mater.* **2007**, *310*, 1386.
- [228] O. Petrova, O. Tchernyshyov, *Phys. Rev. B* **2011**, *84*, 214433.
- [229] R. Y. Umetsu, A. Okubo, A. Fujita, T. Kanomata, K. Ishida, R. Kainuma, *IEEE Trans. Magn.* **2011**, *47*, 2451.
- [230] M. Heide, G. Bihlmayer, S. Blügel, *Phys. Rev. B* **2008**, *78*, 140403.
- [231] Y. Wu, S. Zhang, J. Zhang, W. Wang, Y. L. Zhu, J. Hu, G. Yin, K. Wong, C. Fang, C. Wan, X. Han, Q. Shao, T. Taniguchi, K. Watanabe, J. Zang, Z. Mao, X. Zhang, K. L. Wang, *Nat. Commun.* **2020**, *11*, 3860.
- [232] N. León-Brito, E. D. Bauer, F. Ronning, J. D. Thompson, R. Movshovich, *J. Appl. Phys.* **2016**, *120*, 83903.
- [233] R. Bodenberger, A. Hubert, *Phys. status solidi* **1977**, *44*, K7.
- [234] M. Shinozaki, S. Hoshino, Y. Masaki, J. Kishine, Y. Kato, *J. Phys. Soc. Japan* **2016**, *85*, 74710.

Publications

[J1] Ganbat Duvjir, Taewon Min, **Trinh Thi Ly**, Taehoon Kim, Anh-Tuan Duong, Sunglae Cho, SH Rhim, Jaekwang Lee, Jungdae Kim, “Origin of p-type characteristics in a SnSe single crystal”, Applied Physics Letters, vol. 110, no. 26, pp. 262106, 30th June 2017.

[J2] **Trinh Thi Ly**, Ganbat Duvjir, Taewon Min, Jinho Byun, Taehoon Kim, Mahmoud M. Saad, Nguyen Thi Minh Hai, Sunglae Cho, Jaekwang Lee, Jungdae Kim, “Atomistic study of the alloying behavior of crystalline SnSe_{1-x}S_x”, Physical Chemistry Chemical Physics, vol.19, no.32, pp.21648, 26th July 2017.

[J3] **Trinh Thi Ly**, Jungdae Kim, “Influence of the State of the Tungsten Tip on STM Topographic Images of SnSe Surfaces”, Journal of the Korean Physical Society, vol.72, no.6, pp.658-661, 22nd Mar 2018.

[J4] Ganbat Duvjir, Byoung Ki Choi, Iksu Jang, Søren Ulstrup, Soonmin Kang, **Trinh Thi Ly**, Sanghwa Kim, YoungHwan Choi, Chris Jozwiak, Aaron Bostwick, Eli Rotenberg, Je-Geun Park, Raman Sankar, Ki-Seok Kim*, Jungdae Kim*, Young Jun Chang*, “Emergence of a metal-insulator transition and high temperature charge density waves in VSe₂ at the monolayer limit”, Nano letters, vol.18, no.9, pp.5432-5438, 31st July 2018.

[J5] Ganbat Duvjir, Byoung Ki Choi, **Trinh Thi Ly**, Nguyen Huu Lam, Seung-Hyun Chun, Kyuha Jang, Aloysius Soon, Young Jun Chang, Jungdae Kim, “Novel polymorphic phase of two-dimensional VSe₂: The 1T' structure and its lattice dynamics”, Nanoscale, vol.11, no.42, pp.20096, 7th Oct 2019.

[J6] **Trinh Thi Ly**, Taehun Lee, Sanghwa Kim, Yun-Jae Lee, Ganbat Duvjir, Kyuha Jang, Krisztian Palotas, Se-Young Jeong, Aloysius Soon, Jungdae Kim, “Growing Ultrathin Cu₂O Films on Highly Crystalline Cu(111): A Closer Inspection from Microscopy and Theory”, The Journal of Physical Chemistry C, vol.123, no.20, pp.12716-12721, 2nd May 2019.

[J7] **Trinh Thi Ly**, Ganbat Duvjir, Nguyen Huu Lam, Byoung Ki Choi, Young Jun Chang, Jungdae Kim, “ $\sqrt{3}\times 2$ and $\sqrt{3}\times\sqrt{7}$ Charge Density Wave Driven by Lattice Distortion in Monolayer VSe₂”, Journal of the Korean Physical Society, vol.76, no.5, pp.412-415, 13th Mar 2020.

[J8] Anh-Tuan Pham, Thi Hoa Vu, Chang Cheng, **Trinh Thi Ly**, Ji-Eun Lee, Hyejin Ryu, Choongyu Hwang, Sung-Kwan Mo, Jungdae Kim, Li-dong Zhao, Anh-Tuan Duong, Sunghae Cho, “High-Quality SnSe₂ Single Crystals: Electronic and Thermoelectric Properties”, ACS Applied Energy Materials, vol.3, no.11, pp.10787-10792, 25th Sept 2020.

[J9] **Trinh Thi Ly**, Jungmin Park, Kyoo Kim, Hyo-Bin Ahn, Nyun Jong Lee, Kwangsu Kim, Tae-Eon Park, Ganbat Duvjir, Nguyen Huu Lam, Kyuha Jang, Chun-Yeol You, Younghun Jo, Se Kwon Kim, Changgu Lee, Sanghoon Kim, Jungdae Kim, “Direct Observation of Fe-Ge Ordering in Fe_{5-x}GeTe₂ Crystals and Resultant Helimagnetism”, Advanced Functional Materials, vol. 31, no. 17, pp.2009758, 22nd April 2021.

[J10] Yun-Jae Lee, **Trinh Thi Ly**, Taehun Lee, Krisztián Palotás, Se Young Jeong, Jungdae Kim, Aloysius Soon, “Completing the picture of initial oxidation on copper”, Applied Surface Science, vol. 562, pp.150148, 24th May 2021.

[J11] Ganbat Duvjir, Byoung Ki Choi, **Trinh Thi Ly**, Nguyen Huu Lam, Kyuha Jang, Dang Duc Dung, Young Jun Chang, Jungdae Kim, “Multiple charge density wave phases of monolayer VSe₂ manifested by graphene substrates”, Nanotechnology, vol. 32, No. 36, pp.364002, 18th June 2021.